This is to certify that the

dissertation entitled

NATURAL RESONANCE REPRESENTATION OF THE TRANSIENT FIELD REFLECTED BY A PLANAR LAYERED LOSSY DIELECTRIC

presented by

JONG CHAN OH

has been accepted towards fulfillment
of the requirements for

Ph.D degree in Electrical Engineering

Edward J Rothwell
Major professor

Date 12/4/02

NATURAL RESONANCE REPRESENTATION OF THE TRANSIENT FIELD REFLECTED BY A PLANAR LAYERED LOSSY DIELECTRIC

By

JONG CHAN OH

A DISSERTATION

Submitted to
Michigan State University
in partial fulfillment of the requirements
for the degree of

DOCTOR OF PHILOSOPHY

Department of Electrical and Computer Engineering

2002

ABSTRACT

NATURAL RESONANCE REPRESENTATION OF THE TRANSIENT FIELD REFLECTED BY A PLANAR LAYERED LOSSY DIELECTRIC

By

JONG CHAN OH

The impulse response of a conductor-backed or air-backed lossy dielectric slab with frequency independent or dependent (Debye type) material parameters is evaluated analytically. It is shown that the impulse response consists of a specular reflection from the interface between free-space and the dielectric slab during the early-time period, and a natural mode series, which is a pure sum of damped sinusoids whose frequencies are determined by the poles of the complex s-plane reflection coefficient, during the late-time period. Time-domain responses using a truncated Gaussian pulse as an input with an arbitrary incident angle and with parallel or perpendicular polarization are compared to responses found by the inverse fast Fourier transform. The results may be applied to material characterization using the E-pulse method, and also give physical insight into the nature of transient scattering by a layered medium.

For my wife Sun-Kyung and our children Sang-Jun and Sang-Gun

Acknowledgements

I would like to express my sincere gratitude to the Republic of Korea Air Force for providing me the opportunity to study abroad. I would also like to thank those who taught, guided, and encouraged me throughout my academic pursuit. Foremost, I am deeply indebted to my academic advisor Professor Edward Rothwell for his invaluable guidance and encouragement. I would like to thank him for enabling me to successfully complete my research endeavors. I am very grateful to Professor Dennis Nyquist for his generosity, and in providing motivation through his inspirational lectures. Special thanks must be given to Professor Leo Kempel and Mrs. Kempel for their kindness and encouragement in helping me to overcome difficulties in times of need. I would like to express my thanks to Professor Byron Drachman for his guidance and generosity. I also would like to extend my thanks to Professor Shanker Balasubramaniam who joined my guidance committee in place of Professor Nyquist. I am very much thankful to Hyun Park and the colleagues in EM group, especially Christopher Coleman, Jeffery Meese, and Brad Perry for their help and invaluable discussions.

Finally, I would like to reserve my deepest gratitude to my wife, my best friend Sun-Kyung, and my sons Sang-Jun and Sang-Gun for their encouragement and patience. Without their support, this research would not have been possible.

Table of Contents

List of Tables

List of Figures

Chapter 1: Introduction

Time domain electromagnetics has been utilized for various applications such as target-signature analysis and the determination of the intrinsic properties of materials [1], mainly due to its adaptability to the broadband signals. The singularity expansion method (SEM) [2] which views the late-time period transient response of a scatterer as a series of the residues at the poles of the Green function [3], has been studied by many researchers for the target-signature analysis purpose. Here, the late-time period refers to the time period after the forcing function completely excites the entire body of a scatterer, whereas the early-time period refers to the time period before the late-time begins. The applications of the singularity expansion method and its limitations are found in [4]-[6].

On the other hand, the E-pulse method [7]-[9] which is one of the most successful target identification schemes using the singularity expansion method, can be used for non-destructive material testing [10], [11]. Here, the E-pulse refers to the signal that is synthesized to annihilate the output response when it is convolved with the late-time period target response, such that it can provide a measure to determine the closeness of the unknown target signature to the library of the known target signatures.

Layered materials are often applied to conducting surfaces for the purpose of reducing the scattered field strength within specific frequency bands. Because of the band-limited nature of the reflected field, a wideband pulse can be used to interrogate the layered structure so as to characterize the materials or determine whether the materials have degraded. The E-pulse method can be used to determine whether the material properties have changed compared to baseline values determined by previous measurements or constructed by analytically obtained natural resonance series, provided that the late-time response can be

expressed as a natural resonance series. Therefore, it is important to identify the natural frequencies, i.e., the poles of the reflection coefficient in the complex s-plane, and to show that the late-time response is indeed a sum of damped sinusoids.

So far, there has been no detailed analysis of the transient response of a layered medium as a resonance series, except the work done by Tihuis and Block in 1984 [12], [13]. They calculated the transient scattering of a normally incident plane wave by an air-backed lossy dielectric slab using the singularity expansion method. However, their approach was semi-analytic and did not clearly show that the late-time response can be expressed as a pure natural resonance series, due to the difficulty in evaluating the contributions from the branch cut and the closing contours at infinity when evaluating the Laplace inversion integrals.

In this thesis, we will consider a conductor-backed or air-backed lossy dielectric slab with frequency independent or dependent (Debye type) material parameters, and a plane wave excitation of both TE and TM polarization at arbitrary incidence angle. It will be shown that the integral contribution from the closing contours at infinity vanishes as long as the input waveform is at least APC (almost piecewise continuous) and time limited [14]. When viewed as a functional, the delta function can be considered APC, and thus the impulse response can be computed directly. Also, it will be shown analytically that the branch-cut contribution for the current problem vanishes.

By evaluating the impulse response, it will be shown that the transient field reflected by a conductor-backed or air-backed lossy dielectric slab can be represented as the sum of early-time and late-time components. The early-time component consists of the specular reflection from the air-slab interface, which persists until the arrival of the field reflected by the backing material. The ensuing multiple reflections can be viewed as the late-time component, which is written as a pure sum of natural resonance modes. The scattered field impulse response will be

determined as an inverse Laplace transform of the frequency-domain reflection coefficient, and will be shown that the branch-cut contribution vanishes during the late-time period, except for the residual contributions at the poles on the branch-cut, allowing a pure natural resonance representation.

Results computed using the resonance formulation are verified by comparing to the direct inverse fast Fourier transform (IFFT). The distribution of resonance frequencies in the complex plane, and their dependence on conductivity and incidence angle is examined.

This thesis is organized in 6 chapters. In Chapter 2, the frequency domain formulation of plane-wave propagation in a general planar layered medium is presented. In particular, the interfacial reflection coefficient $\Gamma(\omega)$ and the reflection coefficient $R(\omega)$ are distinctively defined, and the definitions are applied throughout the thesis.

In Chapters 3 and 4, the transient responses from the conductor-backed and the air-backed cases with frequency independent material parameters are examined. The complex s-plane poles of the reflection coefficient are found numerically and the residues at the poles are calculated. The transient responses are constructed from the residue series and they are compared to the responses obtained by the IFFT.

In Chapter 5, the formulation of the frequency domain reflection with a frequency dependent Debye type permittivity [28]-[32] for both conductor-backed and air-backed cases is presented. The transient responses from water with varying conductivity are constructed and compared to the responses from the IFFT.

Finally, the conclusions and the proposed future research areas are presented in Chapter 6.

Chapter 2: Frequency Domain Analysis of Plane-Wave Propagation in a General Planar Layered Medium

The frequency domain representation of plane waves in a planar layered medium can be found in [15]. In this chapter, these representations will be reviewed and specialized for the current problem. For the subsequent discussion, only source-free, linear, isotropic, homogeneous materials are considered.

2.1 The frequency domain wave equation

In a source-free and simple material, Maxwell's equations in terms of $\mathbf{E}$ and $\mathbf{H}$ are

$$\nabla \times \mathbf{E} = -j\omega\mu\mathbf{H}, \tag{2.1}$$

$$\nabla \times \mathbf{H} = j\omega\epsilon^c\mathbf{E}, \tag{2.2}$$

$$\nabla \cdot \mathbf{E} = 0, \tag{2.3}$$

$$\nabla \cdot \mathbf{H} = 0, \tag{2.4}$$

where ϵ^c is the frequency-dependent complex permittivity which is a combination of the conductivity $\sigma(\omega)$ and the permittivity $\epsilon(\omega)$. The curl of (2.1) is then,

$$\nabla \times (\nabla \times \mathbf{E}) = -j\omega\mu(\nabla \times \mathbf{H}) = -j\omega\mu(j\omega\epsilon^c\mathbf{E}).$$

Since, $\nabla \times (\nabla \times \mathbf{E}) = \nabla(\nabla \cdot \mathbf{E}) - \nabla^2\mathbf{E}$, using (2.3) gives

$$\nabla^2\mathbf{E} + k^2\mathbf{E} = 0 \tag{2.5}$$

Here, $k = \omega\sqrt{\mu\epsilon^c}$ is the wave number of the medium. Similarly, taking the curl of (2.2),

$$\nabla \times (\nabla \times \mathbf{H}) = j\omega\epsilon^c(\nabla \times \mathbf{E}) = j\omega\epsilon^c(-j\omega\mu\mathbf{H}),$$

and thus

$$\nabla^2\mathbf{H} + k^2\mathbf{H} = 0. \tag{2.6}$$

Equations (2.5) and (2.6) are the *homogeneous vector Helmholtz equations.* Thus, the rectangular components of $\mathbf{E}$ and $\mathbf{H}$ satisfy the scalar wave equation

$$\nabla^2\psi + k^2\psi = 0,$$

whose solution is a linear combination of the harmonic functions,

$$\sin kx, \quad \cos kx, \quad e^{jkx}, \quad e^{-jkx}.$$

Consider a propagating-wave solution to the homogeneous vector Helmholtz equation,

$$\mathbf{E} = \mathbf{E}_0 e^{-jk_x x} e^{-jk_y y} e^{-jk_z z}$$

where $\mathbf{E}_0$ is the vector amplitude spectrum. If we define the wave vector

$$\mathbf{k} = \hat{\mathbf{x}}k_x + \hat{\mathbf{y}}k_y + \hat{\mathbf{z}}k_z,$$

then,

$$\mathbf{E} = \mathbf{E}_0 e^{-j\mathbf{k}\cdot\mathbf{r}} \tag{2.7}$$

where

$$\mathbf{r} = \hat{\mathbf{x}}x + \hat{\mathbf{y}}y + \hat{\mathbf{z}}z$$

If $\mathbf{k}$ is real, the vector phase constant $\vec{\beta}$, which is defined by $\vec{\beta} = -\nabla\Phi$ [16], where Φ represents the phase of (2.7), becomes

$$\vec{\beta} = -\nabla(-\mathbf{k} \cdot \mathbf{r}) = \mathbf{k}.$$

Hence, the equiphase surfaces are planes perpendicular to $\mathbf{k}$, and (2.7) represents a uniform plane wave. If $\mathbf{k}$ is complex, it can be represented as

$$\mathbf{k} = \vec{\beta} - j\vec{\alpha},$$

where both $\vec{\beta}$ and $\vec{\alpha}$ are real vectors. Then, the wave propagation constant $\vec{\gamma}$ is [16]

$$\vec{\gamma} = -\nabla\theta = -\nabla(-j\mathbf{k} \cdot \mathbf{r}) = j\mathbf{k} = \vec{\alpha} + j\vec{\beta}.$$

Therefore, the equiphase surface is perpendicular to $\vec{\beta}$ and the eqiamplitude surface is perpendicular to $\vec{\alpha}$. In general, it is not a uniform plane wave unless $\vec{\alpha}$ and $\vec{\beta}$ are in the same direction.

Now, from (2.1) and (2.7),

$$\begin{aligned}
\nabla \times \mathbf{E} &= \nabla \times \left(\mathbf{E}_0 e^{-j\mathbf{k}\cdot\mathbf{r}}\right) \\
&= e^{-j\mathbf{k}\cdot\mathbf{r}} \left(\nabla \times \mathbf{E}_0\right) - \mathbf{E}_0 \times \left(\nabla e^{-j\mathbf{k}\cdot\mathbf{r}}\right) \\
&= -\mathbf{E}_0 \times \left(-j\mathbf{k} e^{-j\mathbf{k}\cdot\mathbf{r}}\right) \\
&= -j\mathbf{k} \times \mathbf{E} = -j\omega\mu\mathbf{H}.
\end{aligned}$$

Therefore,

$$\mathbf{H} = \frac{\mathbf{k} \times \mathbf{E}}{\omega\mu}. \tag{2.8}$$

Taking the cross product to (2.8) with $\mathbf{k}$,

$$\mathbf{k} \times \mathbf{H} = \frac{\mathbf{k} \times (\mathbf{k} \times \mathbf{E})}{\omega\mu} = \frac{\mathbf{k}(\mathbf{k} \cdot \mathbf{E}) - \mathbf{E}(\mathbf{k} \cdot \mathbf{k})}{\omega\mu}.$$

Here, $\mathbf{k} \cdot \mathbf{E} = 0$, since

$$\begin{aligned} \nabla \cdot \mathbf{E} &= \nabla \cdot (\mathbf{E}_0 e^{-j\mathbf{k}\cdot\mathbf{r}}) \\ &= e^{-j\mathbf{k}\cdot\mathbf{r}} \nabla \cdot \mathbf{E}_0 - j\mathbf{k} \cdot \mathbf{E}_0 e^{-j\mathbf{k}\cdot\mathbf{r}} = 0 \end{aligned}$$

As a result,

$$\mathbf{E} = -\frac{\mathbf{k} \times \mathbf{H}}{\omega\epsilon^c}. \tag{2.9}$$

If we assume a uniform plane wave, i.e., $\mathbf{k} = \hat{\mathbf{k}}k$, from (2.8) and (2.9)

$$\mathbf{H} = \frac{\mathbf{k} \times \mathbf{E}}{\eta} = \frac{\mathbf{k} \times \mathbf{E}_0}{\eta} e^{-j\mathbf{k}\cdot\mathbf{r}}, \tag{2.10}$$

$$\mathbf{E} = -\eta\hat{\mathbf{k}} \times \mathbf{H}, \tag{2.11}$$

where $\eta = \omega\mu/k = \sqrt{\mu/\epsilon^c}$. Clearly, these equations represent a TEM wave.

2.2 Reflection from a single interface

2.2.1 Perpendicular polarization

Consider a uniform plane wave incident on a planar interface between two lossy regions of space as shown in Figure 2.1. Here, the incident wave is perpendicularly polarized to the plane of incidence, which is defined as the plane containing the wave propagation vector $\mathbf{k}$ and normal to the interface. At this point it should be

noted that, for a uniform plane wave, the field can be decomposed into two orthogonal components, one parallel and the other perpendicular to the plane of incidence. Therefore, the solutions from each case are sufficient to characterize any arbitrary incident uniform plane wave. For the perpendicularly incident uniform plane wave, the incident fields are

$$\begin{aligned}\mathbf{E^i} &= \hat{\mathbf{y}} E_0^i e^{-jk_1(x\sin\theta_i + z\cos\theta_i)}, \\ \mathbf{H^i} &= \frac{E_0^i}{\eta_1}\left(-\hat{\mathbf{x}}\cos\theta_i + \hat{\mathbf{z}}\sin\theta_i\right) e^{-jk_1(x\sin\theta_i + z\cos\theta_i)}.\end{aligned}$$

Although the reflected field and the transmitted field are not known at this point, they cannot have vector components not present in the incident field, in order to satisfy the boundary conditions at the planar surface. Therefore, the reflected and transmitted fields are

$$\begin{aligned}\mathbf{E^r} &= \hat{\mathbf{y}} E_0^r e^{-jk_1(x\sin\theta_r - z\cos\theta_r)}, \\ \mathbf{H^r} &= \frac{E_0^r}{\eta_1}\left(\hat{\mathbf{x}}\cos\theta_r + \hat{\mathbf{z}}\sin\theta_r\right) e^{-jk_1(x\sin\theta_r - z\cos\theta_r)},\end{aligned}$$

and

$$\begin{aligned}\mathbf{E^t} &= \hat{\mathbf{y}} E_0^t e^{-jk_2(x\sin\theta_t + z\cos\theta_t)}, \\ \mathbf{H^t} &= \frac{E_0^t}{\eta_2}\left(-\hat{\mathbf{x}}\cos\theta_t + \hat{\mathbf{z}}\sin\theta_t\right) e^{-jk_2(x\sin\theta_t + z\cos\theta_t)},\end{aligned}$$

respectively. In order to satisfy the continuity of *tangential* $\mathbf{E}$ and $\mathbf{H}$ over the entire interface, the x-variation of all three partial fields must be the same, i.e.,

$$k_1\sin\theta_i = k_1\sin\theta_r = k_2\sin\theta_t.$$

As a result,

$$\theta_r = \theta_i, \tag{2.12}$$

$$\frac{\sin\theta_t}{\sin\theta_i} = \frac{k_1}{k_2} = \sqrt{\frac{\epsilon_1^c \mu_1}{\epsilon_2^c \mu_2}}. \tag{2.13}$$

Also, z-directed wave impedance $Z = -\dfrac{E_y}{H_x}$ should be continuous at the interface, that is

$$Z_1|_{z=0} = Z_2|_{z=0}. \tag{2.14}$$

Here,

$$\begin{aligned} Z_1|_{z=0} &= -\left.\frac{E_y^{(1)}}{H_x^{(1)}}\right|_{z=0} = -\frac{E_0^i + E_0^r}{(E_0^r - E_0^i)\cos\theta_i/\eta_1} \\ &= \frac{\eta_1(E_0^i + E_0^r)}{\cos\theta_i(E_0^i - E_0^r)}, \end{aligned} \tag{2.15}$$

$$Z_2|_{z=0} = -\left.\frac{E_y^{(2)}}{H_x^{(2)}}\right|_{z=0} = -\frac{1}{-\cos\theta_t/\eta_2} = \frac{\eta_2}{\cos\theta_t}. \tag{2.16}$$

From (2.14) - (2.16),

$$\frac{\eta_1(E_0^i + E_0^r)}{\cos\theta_i(E_0^i - E_0^r)} = \frac{\eta_2}{\cos\theta_t},$$

or

$$E_0^i(\eta_2\cos\theta_i - \eta_1\cos\theta_t) = E_0^r(\eta_2\cos\theta_i + \eta_1\cos\theta_t).$$

Therefore,

$$\begin{aligned} \Gamma &= \frac{E_0^r}{E_0^i} = \frac{\eta_2\cos\theta_i - \eta_1\cos\theta_t}{\eta_2\cos\theta_i + \eta_1\cos\theta_t} \\ &= \frac{\dfrac{\eta_2}{\cos\theta_t} - \dfrac{\eta_1}{\cos\theta_i}}{\dfrac{\eta_2}{\cos\theta_t} + \dfrac{\eta_1}{\cos\theta_i}} = \frac{Z_\perp^{(2)} - Z_\perp^{(1)}}{Z_\perp^{(2)} + Z_\perp^{(1)}}. \end{aligned} \tag{2.17}$$

Here, Γ is the interfacial reflection coefficient, and $\frac{\eta_1}{\cos\theta_i}$ and $\frac{\eta_2}{\cos\theta_t}$ are the z-directed wave impedances in region 1 and region 2 respectively. In order to find the transmission coefficient T, use

$$\hat{\mathbf{z}} \times (\mathbf{E}^i + \mathbf{E}^r)|_{z=0} = \hat{\mathbf{z}} \times \mathbf{E}^t|_{z=0},$$

and thus

$$E_0^i(1+\Gamma) = E_0^t.$$

Therefore,

$$T = \frac{E_0^t}{E_0^i} = 1 + \Gamma. \tag{2.18}$$

Finally, collecting the results from (2.17) and (2.18),

$$\begin{aligned} \Gamma_\perp &= \frac{Z_\perp^{(2)} - Z_\perp^{(1)}}{Z_\perp^{(2)} + Z_\perp^{(1)}}, \quad T_\perp = 1 + \Gamma \\ Z_\perp^{(1)} &= \frac{\eta_1}{\cos\theta_i}, \quad Z_\perp^{(2)} = \frac{\eta_2}{\cos\theta_t} = \frac{\eta_2 k_2}{k_{2,z}}, \end{aligned} \tag{2.19}$$

where $k_{2,z} = k_2 \cos\theta_t$ is the z-component of k_2.

2.2.2 Parallel polarization

Analogous to the perpendicular incidence case, Figure 2.2 shows a uniform plane wave incident on a planar interface between two lossy regions of space with

parallel polarization. In this case the fields are

$$\begin{aligned}
\mathbf{E^i} &= E_0^i\,(\hat{\mathbf{x}}\cos\theta_i - \hat{\mathbf{z}}\sin\theta_i)\,e^{-jk_1(x\sin\theta_i + z\cos\theta_i)},\\
\mathbf{H^i} &= \hat{\mathbf{y}}\frac{E_0^i}{\eta_1}e^{-jk_1(x\sin\theta_i + z\cos\theta_i)},\\
\\
\mathbf{E^r} &= E_0^r\,(\hat{\mathbf{x}}\cos\theta_r - \hat{\mathbf{z}}\sin\theta_r)\,e^{-jk_1(x\sin\theta_r - z\cos\theta_r)},\\
\mathbf{H^r} &= -\hat{\mathbf{y}}\frac{E_0^r}{\eta_1}e^{-jk_1(x\sin\theta_r - z\cos\theta_r)},\\
\\
\mathbf{E^t} &= E_0^t\,(\hat{\mathbf{x}}\cos\theta_t - \hat{\mathbf{z}}\sin\theta_t)\,e^{-jk_2(x\sin\theta_t + z\cos\theta_t)},\\
\mathbf{H^t} &= \hat{\mathbf{y}}\frac{E_0^t}{\eta_2}e^{-jk_2(x\sin\theta_t + z\cos\theta_t)}.
\end{aligned}$$

As with the perpendicular polarization case, $\theta_r = \theta_i$, and the z-directed wave impedance $Z = \dfrac{E_x}{H_y}$ should be continuous at the interface. In parallel polarization,

$$\begin{aligned}
Z_1|_{z=0} &= \left.\frac{E_x^{(1)}}{H_y^{(1)}}\right|_{z=0} = \frac{\cos\theta_i(E_0^i + E_0^r)}{(E_0^i - E_0^r)\eta_1},\\
&= \eta_1\cos\theta_i\frac{E_0^i + E_0^r}{E_0^i - E_0^r} \qquad (2.20)\\
Z_2|_{z=0} &= \left.\frac{E_x^{(2)}}{H_y^{(2)}}\right|_{z=0} = \eta_2\cos\theta_t. \qquad (2.21)
\end{aligned}$$

Then, in order to satisfy the continuity of the tangential wave impedance at the interface,

$$\eta_1\cos\theta_i\frac{E_0^i + E_0^r}{E_0^i - E_0^r} = \eta_2\cos\theta_t,$$

or

$$\eta_1\cos\theta_i(E_0^i + E_0^r) = \eta_2\cos\theta_t(E_0^i - E_0^r).$$

Hence,

$$\Gamma = \frac{E_0^r}{E_0^i} = \frac{\eta_2\cos\theta_t - \eta_1\cos\theta_i}{\eta_2\cos\theta_t + \eta_1\cos\theta_i} = \frac{Z_\parallel^{(2)} - Z_\parallel^{(1)}}{Z_\parallel^{(2)} + Z_\parallel^{(1)}}. \qquad (2.22)$$

In (2.22), $\eta_1 \cos\theta_i$ and $\eta_2 \cos\theta_t$ are the z-directed wave impedances in region 1 and region 2 respectively. In order to find the transmission coefficient T, use

$$\hat{\mathbf{z}} \times (\mathbf{E}^i + \mathbf{E}^r)|_{z=0} = \hat{\mathbf{z}} \times \mathbf{E}^t|_{z=0},$$

and thus

$$(1+\Gamma)\cos\theta_i E_0^i = \cos\theta_t E_0^t.$$

Therefore,

$$T = \frac{E_0^t}{E_0^i} = (1+\Gamma)\frac{\cos\theta_i}{\cos\theta_t} = \frac{2\eta_2 \cos\theta_i}{\eta_2 \cos\theta_t + \eta_1 \cos\theta_i} \tag{2.23}$$

Note that (2.23) is the ratio of the total electric fields at the interface. Hence, later when we apply the tangential boundary conditions at the interfaces in order to obtain the global reflection coefficients of the layered medium, we use

$$T_{\parallel} = \frac{E_{0,x}^t}{E_{0,x}^i} = 1 + \Gamma. \tag{2.24}$$

This is the tangential ratio of the transmitted to incident electrical field.

Finally, collecting the results from (2.22) and (2.24),

$$\begin{aligned} &\Gamma_{\parallel} = \frac{Z_{\parallel}^{(2)} - Z_{\parallel}^{(1)}}{Z_{\parallel}^{(2)} + Z_{\parallel}^{(1)}}, \quad T_{\parallel} = 1 + \Gamma, \\ &Z_{\parallel}^{(1)} = \eta_1 \cos\theta_i, \quad Z_{\parallel}^{(2)} = \eta_2 \cos\theta_t = \frac{\eta_2 k_{2,z}}{k_2}. \end{aligned} \tag{2.25}$$

2.3 Reflection from multiple layers

In this section, the approach used in [15] will be reviewed, and the results will be specialized for the current problem.

Consider $N+1$ regions of space separated by N plannar interfaces as shown in Figure 2.3, and assume that a uniform plane wave is incident on the first interface

at angle θ_i. Each region is assumed isotropic and homogeneous with a frequency-dependent complex permittivity and permeability. As shown in the single interface case, in order to satisfy the boundary conditions, each region, except region N, contains an incident-type wave of the form

$$\mathbf{E}^i = \mathbf{E}_0^i e^{-j\mathbf{k}^i \cdot \mathbf{r}}$$

and a reflected-type wave of the form

$$\mathbf{E}^r = \mathbf{E}_0^r e^{-j\mathbf{k}^r \cdot \mathbf{r}}.$$

In region n, the wave vectors are described as

$$\mathbf{k}_n^i = \hat{\mathbf{x}} k_{x,n} + \hat{\mathbf{z}} k_{z,n}\,, \quad \mathbf{k}_n^r = \hat{\mathbf{x}} k_{x,n} - \hat{\mathbf{z}} k_{z,n}\,.$$

Here, in order to satisfy the boundary conditions, Snell's law of reflection should hold. Therefore,

$$k_{x,n} = k_{x,0} = k_0 \sin\theta_i. \tag{2.26}$$

For the case of perpendicular polarization, the electrical field in region n, $0 \le n \le N-1$, is $\mathbf{E} = \mathbf{E}_n^i + \mathbf{E}_n^r$ where

$$\begin{aligned} \mathbf{E}_n^i &= \hat{\mathbf{y}} a_{n+1} e^{-jk_{x,n}x} e^{-jk_{z,n}(z - z_{n+1})}, \\ \mathbf{E}_n^r &= \hat{\mathbf{y}} b_{n+1} e^{-jk_{x,n}x} e^{+jk_{z,n}(z - z_{n+1})}, \end{aligned}$$

and the magnetic field is $\mathbf{H} = \mathbf{H}_n^i + \mathbf{H}_n^r$ where

$$\begin{aligned} \mathbf{H}_n^i &= \frac{-\hat{\mathbf{x}} k_{z,n} + \hat{\mathbf{z}} k_{x,n}}{k_n \eta_n} a_{n+1} e^{-jk_{x,n}x} e^{-jk_{z,n}(z - z_{n+1})}, \\ \mathbf{H}_n^r &= \frac{+\hat{\mathbf{x}} k_{z,n} + \hat{\mathbf{z}} k_{x,n}}{k_n \eta_n} b_{n+1} e^{-jk_{x,n}x} e^{+jk_{z,n}(z - z_{n+1})}. \end{aligned}$$

When $n = N$ there is no reflected wave, therefore

$$\begin{aligned}\mathbf{E}_N &= \hat{\mathbf{y}} a_{N+1} e^{-jk_{x,N}x} e^{-jk_{z,N}(z - z_N)}, \\ \mathbf{H}_N &= \frac{-\hat{\mathbf{x}}k_{z,N} + \hat{\mathbf{z}}k_{x,N}}{k_n \eta_n} a_{N+1} e^{-jk_{x,N}x} e^{-jk_{z,N}(z - z_N)}.\end{aligned}$$

Since a_1 is the known amplitude of the incident wave, there are $2N$ unknown wave amplitudes, and $2N$ simultaneous equations by applying the boundary conditions at each of the interfaces. At interface n located at $z = z_n$, $1 \leq n \leq N - 1$, from the continuity of tangential electric field

$$a_n + b_n = a_{n+1} e^{-jk_{z,n}(z_n - z_{n+1})} + b_{n+1} e^{+jk_{z,n}(z_n - z_{n+1})} \tag{2.27}$$

while from the continuity of magnetic field

$$\begin{aligned}-a_n \frac{k_{z,n-1}}{k_{n-1}\eta_{n-1}} + b_n \frac{k_{z,n-1}}{k_{n-1}\eta_{n-1}} &= -a_{n+1} \frac{k_{z,n}}{k_n \eta_n} e^{-jk_{z,n}(z_n - z_{n+1})} + \\ &\quad b_{n+1} \frac{k_{z,n}}{k_n \eta_n} e^{+jk_{z,n}(z_n - z_{n+1})}.\end{aligned} \tag{2.28}$$

Noting that the wave impedance of region n for the perpendicular polarization is

$$Z_{\perp n} = \frac{k_n \eta_n}{k_{z,n}}$$

and defining the region n propagation factor as

$$P_n = e^{-jk_{z,n}\Delta_n} \tag{2.29}$$

where $\Delta_n = z_{n+1} - z_n$, (2.27) and (2.28) become

$$a_n P_n + b_n P_n = a_{n+1} + b_{n+1} P_n^2, \tag{2.30}$$

$$-a_n P_n + b_n P_n = -a_{n+1} \frac{Z_{\perp n-1}}{Z_{\perp n}} + b_{n+1} \frac{Z_{\perp n-1}}{Z_{\perp n}} P_n^2. \tag{2.31}$$

When $z = z_N$, (2.30) and (2.31) hold if we set $b_{N+1} = 0$ and $P_N = 1$. The $2N$ simultaneous equations (2.30) and (2.31) may be solved using standard matrix methods. However, through a little manipulation, these equations can be solved by recursion. By subtracting (2.31) from (2.30),

$$2a_n P_n = a_{n+1} \left[1 + \frac{Z_{\perp n-1}}{Z_{\perp n}} \right] + b_{n+1} P_n^2 \left[1 - \frac{Z_{\perp n-1}}{Z_{\perp n}} \right]. \tag{2.32}$$

Defining

$$\Gamma_n = \frac{Z_{\perp n} - Z_{\perp n-1}}{Z_{\perp n} + Z_{\perp n-1}} \tag{2.33}$$

as the *interfacial reflection coefficient* for interface n, and

$$T_n = \frac{2Z_{\perp n}}{Z_{\perp n} + Z_{\perp n-1}} = 1 + \Gamma_n \tag{2.34}$$

as the *interfacial transmission coefficient* for interface n, (2.32) can be written as

$$a_{n+1} = a_n T_n P_n + b_{n+1} P_n (-\Gamma_n) P_n. \tag{2.35}$$

Finally, if we define the *global* reflection coefficient R_n for region n as the ratio of the amplitudes of the reflected and incident waves,

$$R_n = \frac{b_n}{a_n},$$

(2.35) can be written as

$$a_{n+1} = a_n T_n P_n + a_{n+1} R_{n+1} P_n(-\Gamma_n) P_n. \tag{2.36}$$

If we choose to eliminate a_{n+1} from (2.30) and (2.31) we find that

$$b_n = a_n \Gamma_n + R_{n+1} P_n (1 - \Gamma_n) a_{n+1}. \tag{2.37}$$

Equations (2.36) and (2.37) have nice physical interpretations. Consider Figure 2.4, which shows the wave amplitudes for region n. We may think of the wave incident on interface $n+1$ with amplitude a_{n+1} as consisting of two terms. The first term is the wave transmitted through interface n. This wave must propagate through a distance Δ_n to reach interface $n+1$ and thus has an amplitude $a_n T_n P_n$. The second term is the reflection at interface n of the wave traveling in the $-z$ direction within region n. The amplitude of the wave before reflection is merely $b_{n+1} P_n$, where the term P_n results from the propagation of the negatively-traveling wave from interface $n+1$ to interface n. Now, since the interfacial reflection coefficient at interface n for a wave incident from region n is the negative of that for a wave incident from region $n-1$, and since the reflected wave must travel through a distance Δ_n from interface n back to interface $n+1$, the amplitude of the second term is $b_{n+1} P_n(-\Gamma_n) P_n$. Finally, remembering that $b_{n+1} = R_{n+1} a_{n+1}$, we can write

$$a_{n+1} = a_n T_n P_n + a_{n+1} R_{n+1} P_n(-\Gamma_n) P_n.$$

This equation is exactly the same as (2.36) which was found using the boundary conditions. By similar reasoning, we may say that the wave traveling in the $-z$ direction in region $n-1$ consists of a term reflected from the interface and a term transmitted through the interface. The amplitude of the reflected term is merely

$a_n\Gamma_n$. The amplitude of the transmitted term is found by considering $b_{n+1} = R_{n+1}a_{n+1}$ propagated through a distance Δ_n and then transmitted backwards through interface n. Since the transmission coefficient for a wave going region n to region $n-1$ is $1+(-\Gamma_n)$, the amplitude of the transmitted term is $R_{n+1}P_n(1-\Gamma_n)a_{n+1}$. Thus

$$b_n = \Gamma_n a_n + R_{n+1}P_n(1-\Gamma_n)a_{n+1},$$

which is identical to (2.37).

Now, from (2.34) and (2.36)

$$a_{n+1} = \frac{(1+\Gamma_n)P_n}{1+\Gamma_n R_{n+1}P_n^2}a_n. \tag{2.38}$$

Substituting this into (2.37)

$$b_n = \frac{\Gamma_n + R_{n+1}P_n^2}{1+\Gamma_n R_{n+1}P_n^2}a_n. \tag{2.39}$$

Using this expression we find a recursive relationship for the gloval reflection coefficient:

$$R_n = \frac{b_n}{a_n} = \frac{\Gamma_n + R_{n+1}P_n^2}{1+\Gamma_n R_{n+1}P_n^2}. \tag{2.40}$$

The procedure is now as follows. The global reflection coefficient for interface N is obtained from (2.40) with $R_{N+1} = 0$. We next find R_{N-1}:

$$R_{N-1} = \frac{\Gamma_{N-1} + R_N P_{N-1}^2}{1+\Gamma_{N-1}R_N P_{N-1}^2}.$$

This process is repeated until reaching R_1, whereupon all of the global reflection coefficients are known. We then find the amplitudes beginning with a_1, which is the known incident field amplitude. From (2.40) we find $b_1 = a_1R_1$, and from (2.38) we

find

$$a_2 = \frac{(1+\Gamma_1)P_1}{1+\Gamma_1 R_2 P_1^2} a_1.$$

This process is repeated until all field amplitudes are known.

Note that the process outlined above holds equally well for parallel polarization as long as we use the parallel wave impedances

$$Z_{\parallel n} = \frac{k_{x,n}\eta_n}{k_n}$$

when computing the interfacial reflection coefficients.

Now, specializing (2.40) for the problems of interest, first consider a PEC-backed lossy slab. In this case $N = 2$ and $R_2 = -1$, thus from (2.40) the global reflection coefficient in region 0, which is free-space, becomes

$$R_1 = \frac{\Gamma_1 - P_1^2}{1 - \Gamma_1 P_1^2}. \tag{2.41}$$

Next, for an air-backed lossy slab where $R_2 = -\Gamma_1$, the global reflection coefficient in region 0 becomes

$$R_1 = \frac{\Gamma_1(1 - P_1^2)}{1 - \Gamma_1^2 P_1^2}. \tag{2.42}$$

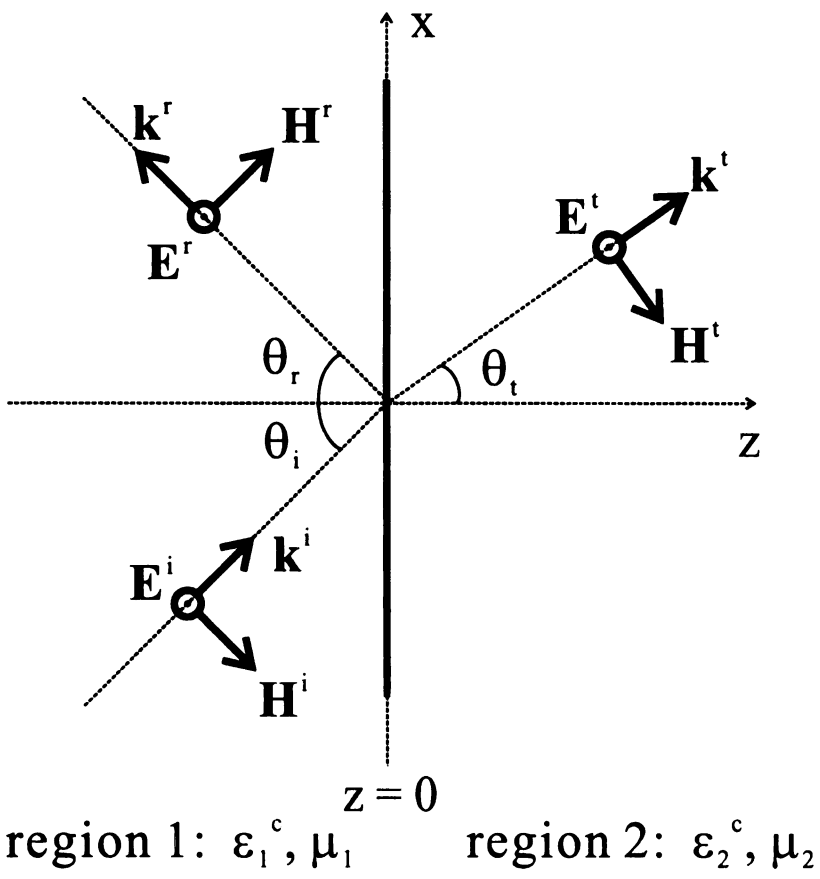

Figure 2.1: Uniform plane wave incident on a planar interface between two lossy regions of space. Perpendicular polarization.

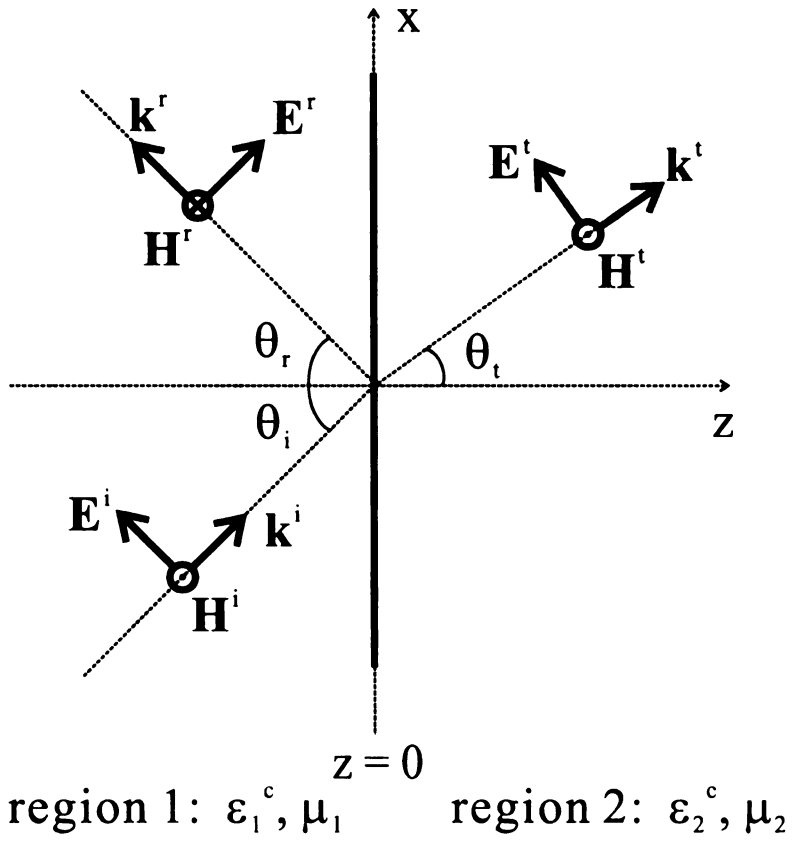

Figure 2.2: Uniform plane wave incident on a planar interface between two lossy regions of space. Parallel polarization.

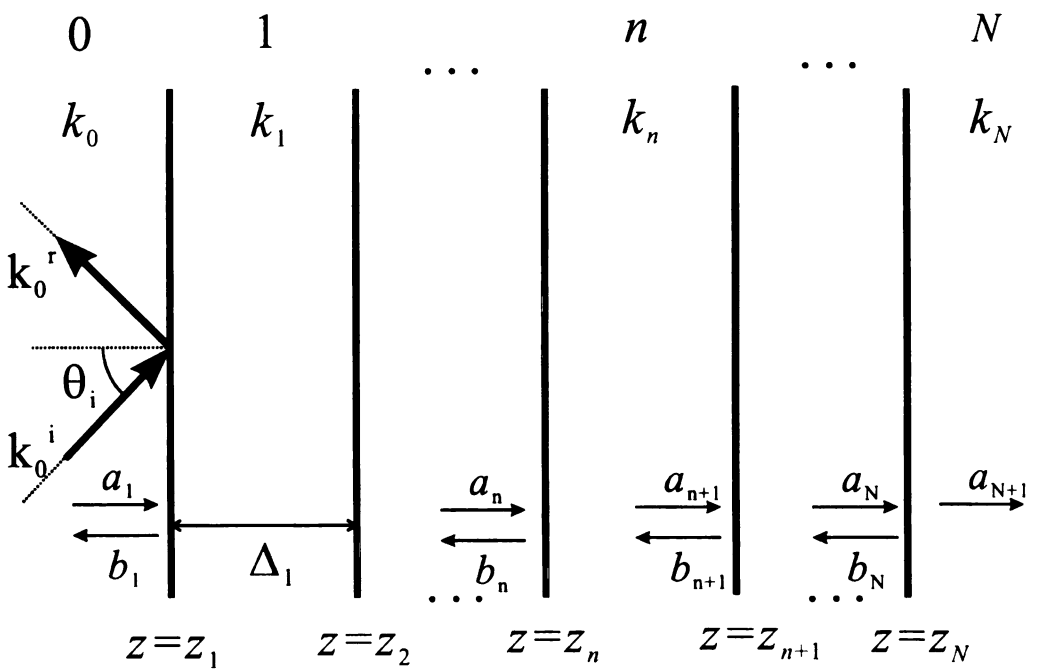

Figure 2.3: Interaction of a uniform plane wave with a multi-layered material.

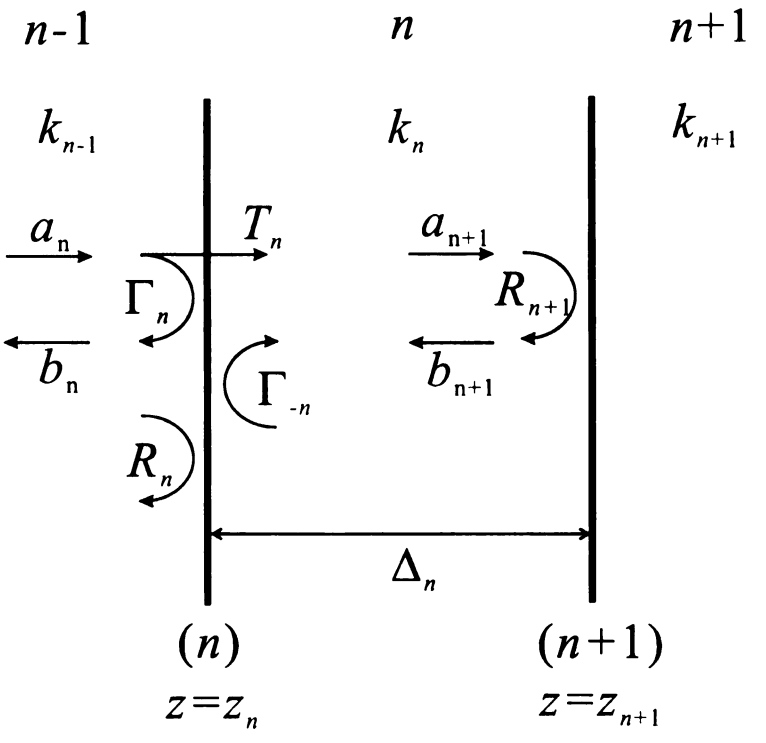

Figure 2.4: Wave flow diagram showing interaction of incident and reflected waves for region n.

Chapter 3: Natural Mode Analysis of a Conductor-Backed Slab

3.1 Formulation of the frequency-domain reflection

3.1.1 The frequency-domain reflection coefficient

Consider a plane wave of frequency ω incident from free space onto an interface between free space and a conductor backed slab of material with frequency independent material parameters $\epsilon = \epsilon_r\epsilon_0$, μ_0, and σ, and with thickness Δ, as shown in Figure 3.1. In the figure, region 0 and region 1 correspond to free space and the dielectric slab respectively. Likewise, for the subsequent discussion, the subscripts 0 and 1 correspond to free space and dielectric, respectively. As seen in (2.29), (2.33) and (2.41), the reflection coefficients have the general form

$$R(\omega) = \frac{\Gamma(\omega) - P^2(\omega)}{1 - \Gamma(\omega)P^2(\omega)} \tag{3.1}$$

where $\Gamma(\omega)$ is the interfacial reflection coefficient, given in general form by

$$\Gamma(\omega) = \frac{Z_1(\omega) - Z_0}{Z_1(\omega) + Z_0},$$

and $P(\omega)$ is the propagation factor, defined by

$$P(\omega) = e^{-jk_{z,1}\Delta}.$$

Since

$$k_1^2 = k_{x,1}^2 + k_{z,1}^2$$

where

$$\begin{aligned} k_1^2 &= \omega^2 \mu_0 \epsilon^c, \quad \epsilon^c = \epsilon + \frac{\sigma}{j\omega}, \\ k_{x,1} &= k_0 \sin\theta_i = \omega\sqrt{\mu_0\epsilon_0}\sin\theta_i, \end{aligned}$$

the z-component of the wave number k_1 becomes

$$\begin{aligned} k_{z,1} &= \sqrt{k_1^2 - k_{x,1}^2} = \sqrt{\omega^2\mu_0\epsilon^c - \omega^2\mu_0\epsilon_0\sin^2\theta_i} \\ &= \sqrt{\omega^2\mu_0(\epsilon + \frac{\sigma}{j\omega}) - \omega^2\mu_0\epsilon_0\sin^2\theta_i} \\ &= \sqrt{\omega^2\mu_0\epsilon_0(\epsilon_r + \frac{\sigma}{j\omega\epsilon_0} - \sin^2\theta_i)} \\ &= k_0\sqrt{\epsilon_r + \frac{\sigma}{j\omega\epsilon_0} - \sin^2\theta_i} = \frac{\omega}{c}\sqrt{\epsilon_r + \frac{\sigma}{j\omega\epsilon_0} - \sin^2\theta_i}. \end{aligned} \tag{3.2}$$

Defining $\bar{\epsilon} = \epsilon_r - \sin^2\theta_i$, (3.2) can be written as

$$k_{z,1} = \frac{\omega}{c}F(\omega), \quad F(\omega) = \sqrt{\bar{\epsilon} + \frac{\sigma}{j\omega\epsilon_0}}.$$

Hence, for perpendicular polarization

$$Z_1(\omega) \equiv Z_\perp(\omega) = \frac{k_1\eta_1}{k_{z,1}} = \frac{\eta_0}{F(\omega)}, \quad Z_0 \equiv Z_{0\perp} = \frac{\eta_0}{cos\theta_i}, \tag{3.3}$$

and for parallel polarization

$$Z_1(\omega) \equiv Z_\parallel(\omega) = \frac{k_{z,1}\eta_1}{k_1} = \frac{\eta_0 F(\omega)}{\epsilon_r + \frac{\sigma}{j\omega\epsilon_0}}, \quad Z_0 \equiv Z_{0\parallel} = \eta_0 cos\theta_i. \tag{3.4}$$

As a result, (3.1) is written as

$$R(\omega) = \frac{\Gamma(\omega) - e^{-j\omega\tau(\omega)}}{1 - \Gamma(\omega)e^{-j\omega\tau(\omega)}}, \tag{3.5}$$

where

$$\tau(\omega) = \frac{2\Delta}{c}F(\omega).$$

3.1.2 The impulse response

Since $R(\omega)$ exists, its Laplace domain representation also exists [21]-[23] and is given by

$$R(s) = R(\omega)|_{\omega=s/j} = \frac{\Gamma(s) - e^{-s\tau(s)}}{1 - \Gamma(s)e^{-s\tau(s)}}, \tag{3.6}$$

where

$$\begin{aligned} s\tau(s) &= j\omega\tau(\omega)|_{\omega=s/j} \\ &= j\omega\frac{2\Delta}{c}F(\omega)|_{\omega=s/j} = s\frac{2\Delta}{c}\sqrt{\bar{\epsilon} + \frac{\sigma}{s\epsilon_0}} \\ &= \frac{2\Delta}{c}\sqrt{\bar{\epsilon}}\sqrt{s}\sqrt{s + \frac{\sigma}{\epsilon_0\bar{\epsilon}}} \\ &= \frac{2\Delta}{\nu}\sqrt{s}\sqrt{s - s_0}, \qquad (3.7) \\ \Gamma(s) &= \frac{Z_1(s) - Z_0}{Z_1(s) + Z_0}. \qquad (3.8) \end{aligned}$$

Here $\nu = c/\sqrt{\bar{\epsilon}}$ and $s_0 = -\sigma/(\epsilon_0\bar{\epsilon})$. For perpendicular polarization the z-directed impedance $Z_1(s)$ is

$$\begin{aligned} Z_\perp(s) &= \left.\frac{\eta_0}{F(\omega)}\right|_{\omega=s/j} = \frac{\eta_0}{\sqrt{\bar{\epsilon} + \frac{\sigma}{s\epsilon_0}}} \\ &= \frac{\eta_0 s}{\sqrt{\bar{\epsilon}}\sqrt{s}\sqrt{s - s_0}}, \end{aligned} \tag{3.9}$$

and for parallel polarization

$$Z_{\parallel}(s) = \left.\frac{\eta_0 F(\omega)}{\epsilon_r + \frac{\sigma}{j\omega\epsilon_0}}\right|_{\omega=s/j} = \frac{\eta_0\sqrt{\bar{\epsilon} + \frac{\sigma}{s\epsilon_0}}}{\epsilon_r + \frac{\sigma}{s\epsilon_0}} = \frac{\eta_0\sqrt{\bar{\epsilon}}\sqrt{s}\sqrt{s - s_0}}{s\epsilon_r + \frac{\sigma}{\epsilon_0}}. \tag{3.10}$$

Therefore, the interfacial reflection coefficient $\Gamma(s)$ in (3.8) can be written as

$$\Gamma(s) = \begin{cases} \dfrac{s\cos\theta_i - \sqrt{\bar{\epsilon}}\sqrt{s}\sqrt{s - s_0}}{s\cos\theta_i + \sqrt{\bar{\epsilon}}\sqrt{s}\sqrt{s - s_0}}. & (\perp \text{ pol.}) \\ \dfrac{\sqrt{\bar{\epsilon}}\sqrt{s}\sqrt{s - s_0} - \cos\theta_i(s\epsilon_r + \frac{\sigma}{\epsilon_0})}{\sqrt{\bar{\epsilon}}\sqrt{s}\sqrt{s - s_0} + \cos\theta_i(s\epsilon_r + \frac{\sigma}{\epsilon_0})}. & (\parallel \text{ pol.}) \end{cases} \tag{3.11}$$

The reflection coefficient $R(s)$ is the transfer function of the system. Thus, the impulse response $r(t)$ is obtained by

$$r(t) = \mathcal{L}^{-1}\{R(s)\} = \frac{1}{j2\pi}\int_{Br} R(s)e^{st}ds \tag{3.12}$$

where Br indicates the Bromwich path. This integral can be evaluated by contour integration. We must thus examine the singularities and define an appropriate branch for the integrand.

3.2 Singularities and the branch cut

From the complex square roots in $s\tau(s)$ and $Z_1(s)$, the branch points are located at $s = 0$ and $s = s_0$. In order to ensure the continuity of $R(s)$, the branch cut is taken along the negative real axis between the two branch points.

From (3.6), the poles are the roots of

$$1 - \Gamma(s)e^{-s\tau(s)} = 0. \tag{3.13}$$

Taking the logarithm of this equation and rearranging gives

$$\ln\left[\Gamma(s)e^{-s\tau(s)}\right] = \ln\left|\Gamma(s)e^{-s\tau(s)}\right| + j\arg\left[\Gamma(s)e^{-s\tau(s)}\right] \pm j2n\pi = 0, \quad (n = 0, 1, 2, \cdots).$$

Since $-\pi < \arg\left[\Gamma(s)e^{-s\tau(s)}\right] < \pi$ and the goal is to find roots, n can be set to 0. Therefore, the poles should satisfy

$$\ln\left|\Gamma(s)e^{-s\tau(s)}\right| + j\arg\left[\Gamma(s)e^{-s\tau(s)}\right] = 0. \tag{3.14}$$

Except for the lossless case ($\sigma = 0$), wherein the poles can be calculated analytically, the above equation needs to be solved numerically. For the lossless case, both $\Gamma(s)$ and $\tau(s)$ are independent of s, and $-1 < \Gamma < 0$, i.e. $\arg(\Gamma) = \pi$. As a result, from (3.14), the lossless case poles are

$$s = \frac{1}{\tau}\left[\ln|\Gamma| \pm j(2n-1)\pi\right], \quad n = 1, 2, 3, \cdots \tag{3.15}$$

From (3.14) and (3.15), it is clear that the poles occur in complex conjugate pairs as expected for real signals. Table 3.1 shows the lossless case poles, where $\theta_i = 0°$, $\epsilon_r = 9$ and $\Delta = 2$ cm. In the table, only poles in the upper-half complex plane are shown.

When the conductivity is nonzero, equation (3.14) can be solved by 2-D root search algorithms such as the Newton-Rahpson method [17], which was used in this work using the lossless case poles as the initial guesses. At this point, it should be emphasized that the real part of a pole should be less than or equal to zero for a passive system. This can be shown to be true by noting that the magnitude of $\Gamma(s)e^{-s\tau(s)}$ in (3.14) is always less than 1 if $\mathrm{Re}\{s\}$ is greater than zero, since both the magnitudes of $\Gamma(s)$ and $e^{-s\tau(s)}$ are less than 1 as can be shown using (3.7) and (3.11). Here, it should be remembered that $s_0 = -\sigma/(\epsilon_0\bar{\epsilon})$ is a non-positive

constant. As a result, no solution of (3.14) can exist if $\mathrm{Re}\{s\}$ is positive.

Figure 3.2 and Figure 3.3 show several pole trajectories obtained by the Newton-Rahpson method when the conductivity σ varies from 0 to 10 S/m for perpendicular and parallel polarization respectively. When the conductivity reaches a certain value, each pole becomes purely real. In the figures, the conductivity values at which the poles become real are shown, and the corresponding pole locations in the complex s plane are shown as the cross-marks. As shown in the figures, when the conductivity increases, the magnitudes of the imaginary parts of the poles decrease whereas those of the real parts increase until the poles approach the real axis and become purely real. This phenomenon is clearly seen in Figure 3.4 and Figure 3.5. Note the difference between the mode 0 pole trajectories of the perpendicular and parallel polarization cases.

These pole trajectories of both polarizations suggest that when the conductivity becomes higher, the amplitude decay factors become larger, resulting in a smaller contribution to the late-time response.

In Figure 3.6 and Figure 3.7, the pole trajectories for varying angle of incidence are shown, where $\epsilon_r = 9$ and $\sigma = 0.1$ S/m. As seen in Figure 3.6, which depicts the pole amplitudes of the perpendicular polarization case, as the angle of incidence increases, the magnitudes of the real parts of the poles monotonically decrease whereas those of the imaginary parts are relatively unchanged. At this point, it should be emphasized that the pole locations do not solely determine the late-time transient responses. In order to obtain the correct transient responses, the residues corresponding to the poles should be considered. For the parallel polarization case, as the angle of incidence increases, the magnitudes of the real parts of the poles show a dip around 70° of incidence angle which approximately corresponds to the

Brewster angle calculated as [15]

$$\theta_{B\|} = \sin^{-1}\sqrt{\frac{\epsilon_2}{\epsilon_1+\epsilon_2}} = \sin^{-1}\sqrt{\frac{9}{1+9}} = 71.6°,$$

where we assume the dielectric material is lossless and $\epsilon_r = 9$. Also, it should be noticed that the mode 0 pole becomes real approximately at this angle. This behavior evidently suggests that the late-time response may be affected by the Brewster angle. Further discussions on this behavior will be made in the result section of this chapter. The existence condition for the real poles and the algorithm for finding such poles are examined next.

Let us assume a complex frequency s to be negative real and denote its magnitude as x, where $x > 0$. Then, if $s > s_0$, i.e., $\sigma > -s\epsilon_0\bar{\epsilon}$, from (3.7) and (3.11)

$$s\tau(s) = j\frac{2\Delta}{\nu}\sqrt{x}\sqrt{-(x+s_0)}, \tag{3.16}$$

and the reflection coefficient becomes

$$\Gamma(s) = \begin{cases} \dfrac{-x\cos\theta_i - j\sqrt{\bar{\epsilon}}\sqrt{x}\sqrt{-(x+s_0)}}{-x\cos\theta_i + j\sqrt{\bar{\epsilon}}\sqrt{x}\sqrt{-(x+s_0)}}. & (\perp \text{ pol.}) \\ \dfrac{j\sqrt{\bar{\epsilon}}\sqrt{x}\sqrt{-(x+s_0)} - \cos\theta_i(-x\epsilon_r + \frac{\sigma}{\epsilon_0})}{j\sqrt{\bar{\epsilon}}\sqrt{x}\sqrt{-(x+s_0)} + \cos\theta_i(-x\epsilon_r + \frac{\sigma}{\epsilon_0})}. & (\| \text{ pol.}) \end{cases} \tag{3.17}$$

It is now clear that the magnitudes of both $e^{-s\tau(s)}$ and $\Gamma(s)$ are 1. As a result, $\ln\left|\Gamma(s)e^{-s\tau(s)}\right| = 0$, and the poles need to satisfy only the imaginary part of (3.14), i.e., $\arg\left[\Gamma(s)e^{-s\tau(s)}\right] = 0$. Therefore, if we denote $-(2\Delta/\nu)\sqrt{x}\sqrt{-(x+s_0)}$, which is $-s\tau(s)$, as ϕ_1 and $\arg\left[\Gamma(s)\right]$ as ϕ_2, the poles need to satisfy

$$\phi_1 + \phi_2 + 2n\pi = 0. \quad n = 0, 1, 2, \cdots \tag{3.18}$$

Here, only the positive sign in front of n is necessary, since ϕ_1 is always negative,

when $s > s_0$ and $-\pi < \phi_2 < \pi$. The above equation, which we call the *characteristic function*, can be solved by any 1-D root search algorithm, such as the secant method, which was used in this work. Here, it is very important to note that (3.18) does not always have solutions, and that the number of solutions is dependent upon the conductivity, permittivity and incident angle. In addition, great care should be taken when finding the real roots, especially for the $n = 0$ case where the characteristic function can have more than one root, which may cause the usual secant method to fail. Figure 3.8 and Figure 3.9 show the amplitude of the characteristic function versus the amplitude of s, which is purely real. In Figure 3.8, the 0 amplitude line was crossed 3 times by the characteristic function, and the corresponding values of s are the poles. Here, the left end point of the amplitude curve of the $n = 0$ case corresponds to the removable pole located at $s = s_0$ as shown in the following discussion. On the other hand, there is no such crossing in Figure 3.9 implying no pole exists for that case.

If $s < s_0$, $s\tau(s)$ becomes negative real causing $e^{-s\tau(s)}$ to be greater than 1, and $\Gamma(s)$ becomes real. Therefore, in (3.14), $\arg\left[\Gamma(s)e^{-s\tau(s)}\right] = 0$ can only be satisfied when $\Gamma(s) > 0$. If $s < s_0$ and $\Gamma(s) > 0$, the poles only need to satisfy $\ln\left|\Gamma(s)e^{-s\tau(s)}\right| = 0$. Figure 3.10 shows the amplitudes of the reflection coefficients for both polarizations, where $s < s_0$. As shown in the figure, for perpendicular polarization, the reflection coefficient $\Gamma(s) = 1$ when $s = s_0$ and monotonically decreases as s decreases. In particular, it becomes negative when $s < \frac{\sigma}{\epsilon_0(1-\epsilon_r)}$, since the reflection coefficient has roots

$$s = 0, \quad \frac{\sigma}{\epsilon_0(1-\epsilon_r)}.$$

As a result, one additional real pole can exist when $\frac{\sigma}{\epsilon_0(1-\epsilon_r)} < s < s_0$ for perpendicular polarization. Figure 3.11 shows the amplitudes of $-s\tau(s)$, $\ln|\Gamma(s)|$

and their sum for perpendicular polarization. In the figure, the point where $\ln|\Gamma(s)| - s\tau(s)$ crosses the 0 amplitude line represents the pole location. It should be noted that the apparent pole $s = s_0$ where both $e^{-s\tau(s)}$ and $\Gamma(s)$ are 1 is a removable pole, since the numerator of the reflection coefficient becomes identical to the denominator.

For parallel polarization, $\Gamma(s) = -1$ when $s = s_0$, and it has two real roots at

$$s = \frac{\sigma}{\epsilon_0(1-\epsilon_r)}, \quad \frac{\sigma}{\epsilon_0(\tan^2\theta_i - \epsilon_r)}.$$

Therefore, depending on ϵ_r and θ_i, the amplitude of the reflection coefficient increases initially, then stays positive or monotonically decreases as s decreases. As a result, at most 2 real poles can exist when $s < s_0$ for parallel polarization. Figure 3.12 shows the case where 2 real poles exist. However, it should be noted that the contribution to the late time response from the real poles located where $s < s_0$ are dominated by the contributions from the other poles, since their real parts are much smaller than those of the dominant poles.

A complete sketch of the poles is shown in Figure 3.13 and Figure 3.14. In the figures, the solid lines represent the trajectories of the complex poles, and the cross-marks represent the real poles. The real poles consist of the poles with magnitudes less than s_0 and those with magnitudes greater than s_0. Since the complex pole trajectories from different modes follow approximately the same curve in the complex s plane (before each mode becomes real and diverges), it is difficult to resolve each complex pole trajectory from the figures. As previously discussed, the complex poles gradually become real poles as the conductivity increases. Note that, except for mode 0, each single complex pole splits into a pair of real poles.

3.3 Evaluation of $r(t)$

Since all poles and branch points lie in the left half plane including the imaginary axis, the region of convergence is the right half plane. Therefore, the Bromwich path is put in the right half plane and the Laplace inversion integral is evaluated by contour integration. The evaluation is accomplished in two different time intervals, corresponding to the early-time period and the late-time period. The beginning of the late-time period is $\tau_0 = \frac{2\Delta}{\nu}$, which represents the two-way transit time of the wave inside the dielectric slab.

3.3.1 Case I: $t > \tau_0$

When $t > \tau_0$, the integration contour is closed in the left half plane as shown in Figure 3.15. Inside the contour, the branch cut lies from 0 to s_0 and there is a closed path enclosing the branch cut and several possible real poles on the branch cut (two of which are shown). We denote the outer integration contour which includes the Bromwich path as C_0 and the closed path which encloses the branch cut as C_1, such that

$$\begin{aligned} C_0 &= B_r + \Gamma_\infty + L_1 + L_2, \\ C_1 &= \gamma_1 + \gamma_2 + \cdots + \gamma_6 + l_1 + l_2 + \cdots + l_6. \end{aligned}$$

Then, by Cauchy's residue theorem,

$$\int_{C_0+C_1} R(s)e^{st}\,\mathrm{d}s = j2\pi \sum Res[R(s)e^{st}, poles] \tag{3.19}$$

Therefore, if the integral contribution from each path is known, the impulse response $r(t)$ can be determined.

The contribution from Γ_∞

On Γ_∞, from (3.7),

$$\begin{aligned} \mathrm{Re}\{\tau(s)\} &= \mathrm{Re}\left\{\lim_{\mathrm{Re}\{s\}\to-\infty} \frac{2\Delta}{\nu}\sqrt{1+\frac{\sigma}{s\epsilon_0\bar{\epsilon}}}\right\} \\ &\simeq \frac{2\Delta}{\nu} = \tau_0 \end{aligned}$$

If we let $t_1 = t - \tau_0$, which is positive since we are evaluating the integral when $t > \tau_0$, then

$$\int_{\Gamma_\infty} R(s)e^{st}\,\mathrm{d}s = \int_{\Gamma_\infty} \frac{\Gamma(s)e^{s\tau_0} - e^{-s\tau(s)}e^{s\tau_0}}{1-\Gamma(s)e^{-s\tau(s)}}e^{st_1}\,\mathrm{d}s = \int_{\Gamma_\infty} f(s)e^{st_1}\,\mathrm{d}s$$

Since $f(s) \to 0$ on Γ_∞, by *Jordan's Lemma* [20], [21],

$$\int_{\Gamma_\infty} R(s)e^{st}\,\mathrm{d}s = 0 \tag{3.20}$$

The contribution from L_1 and L_2

On L_1 and L_2, it is not possible to apply *Jordan's Lemma* without imposing some restrictions that will be introduced in subsequent discussion, since $R(s)$ does not approach zero over these paths. Furthermore, it would be very difficult to evaluate the inversion integral directly. However, it is possible to apply *Jordan's Lemma* if we use the following theorem [14]:

Theorem *Let $f(t)$ be a function which is APC (almost piecewise continuous) and which is identically zero for t greater than some number T. Then the Laplace transform of $f(t)$ approaches zero uniformly as s becomes infinite in a right half plane,*

$$|\arg(s - c_0)| \leq \frac{\pi}{2},$$

where $c_0 = \sigma_0 + j\omega_0$ is any complex constant in the s plane.

In this theorem, the APC function is piecewise continuous except at a finite number of isolated points. Let the time response of the incident wave be given by $g(t)$, and let this function be APC. Then the response of the system is given by $G(s)R(s)$, where $G(s) = \mathcal{L}\{g(t)\}$. Since $G(s)$ approaches zero on L_1 and L_2, we can use *Jordan's Lemma* to show that the contribution from L_1 and L_2 is zero for an APC input waveform. When considering the impulse response, we view the delta function as a functional that is APC [21], [24], and thus

$$\int_{L_1,L_2} R(s)e^{st}\,\mathrm{d}s = 0 \tag{3.21}$$

The contribution from C_1

The segments of the contour C_1 enclosing the branch cut can be divided into three groups. The first group consists of γ_1 and γ_4 that enclose the branch points s_0 and 0 respectively. The second group consists of the straight lines immediately below and above the branch cut, and those are designated l_1, l_2, $\cdots$, l_6. The last group consists of γ_2, γ_3, γ_5 and γ_6 that enclose the real poles on the branch cut. These groups will be examined separately.

Denote the radius of γ_1 as r, and let θ to be the angle measured counterclockwise from the real axis to the point on γ_1. Then, any point on γ_1 can be represented as

$$s = s_0 + re^{j\theta}.$$

The reflection coefficient on γ_1 with $r \to 0$, i.e. $s \to s_0$, becomes

$$\Gamma(s) = \begin{cases} \dfrac{s\eta_0 - Z_{0\perp}\sqrt{\bar{\epsilon}}\sqrt{s}\sqrt{s-s_0}}{s\eta_0 + Z_{0\perp}\sqrt{\bar{\epsilon}}\sqrt{s}\sqrt{s-s_0}} & \longrightarrow \quad 1, \quad \perp \text{ - pol} \\ \dfrac{\eta_0\sqrt{\bar{\epsilon}}\sqrt{s}\sqrt{s-s_0} - Z_{0\parallel}(s\epsilon_r + \frac{\sigma}{\epsilon_0})}{\eta_0\sqrt{\bar{\epsilon}}\sqrt{s}\sqrt{s-s_0} + Z_{0\parallel}(s\epsilon_r + \frac{\sigma}{\epsilon_0})} & \longrightarrow -1, \quad \parallel \text{ - pol} \end{cases} \tag{3.22}$$

Then,

$$R(s)e^{st} = \frac{\Gamma(s) - e^{-s\tau(s)}}{1 - \Gamma(s)e^{-s\tau(s)}}e^{st} = \begin{cases} e^{st} & , \quad \perp \text{ - pol} \\ -e^{st} & , \quad \| \text{ - pol} \end{cases}$$

and

$$\left|R(s)e^{st}\right| \leq e^{(s_0+r)t}.$$

Therefore,

$$\left|\int_{\gamma_1} R(s)e^{st}\,\mathrm{d}s\right| \leq 2\pi\, r\, e^{(s_0+r)t} \rightarrow 0, \quad (r \rightarrow 0).$$

As a result,

$$\int_{\gamma_1} R(s)e^{st}\,\mathrm{d}s = 0. \tag{3.23}$$

Similarly, it can be shown

$$\int_{\gamma_4} R(s)e^{st}\,\mathrm{d}s = 0. \tag{3.24}$$

For the second group, it is necessary to determine $\Gamma(s)$ and $s\tau(s)$ along a path immediately above the branch cut, which we denote as B^+, and immediately below the branch cut, which we denote as B^-. If we denote the magnitude of s as x $(s_0 + r < -x < -r < 0)$, then on B^+,

$$\sqrt{s}\sqrt{s - s_0} = j\sqrt{x}\sqrt{-x - s_0}\,,$$

and on B^-,

$$\sqrt{s}\sqrt{s - s_0} = -j\sqrt{x}\sqrt{-x - s_0}\,.$$

Now, let $Z(s)$ on B^+ be denoted as Z^+, and Z(s) on B^- as Z^-. Then, using (3.11), it can be shown that

$$Z^+ = -Z^-. \tag{3.25}$$

Since,

$$\begin{aligned} R(s) &= \frac{\Gamma(s) - e^{-s\tau(s)}}{1 - \Gamma(s)e^{-s\tau(s)}} \\ &= \frac{[Z(s) - Z_0]e^{\frac{1}{2}s\tau(s)} - [Z(s) + Z_0]e^{-\frac{1}{2}s\tau(s)}}{[Z(s) + Z_0]e^{\frac{1}{2}s\tau(s)} - [Z(s) - Z_0]e^{-\frac{1}{2}s\tau(s)}}, \end{aligned}$$

we have,

$$\begin{aligned} R(s)|_{B^+} &= \frac{[Z^+ - Z_0]e^{j\phi} - [Z^+ + Z_0]e^{-j\phi}}{[Z^+ + Z_0]e^{j\phi} - [Z^+ - Z_0]e^{-j\phi}} \\ &= \frac{jZ^+ \sin\phi - Z_0 \cos\phi}{jZ^+ \sin\phi + Z_0 \cos\phi} \end{aligned}$$

where $j\phi = \frac{1}{2}s\tau(s)$, and

$$\begin{aligned} R(s)|_{B^-} &= \frac{[Z^- - Z_0]e^{-j\phi} - [Z^- + Z_0]e^{j\phi}}{[Z^- + Z_0]e^{-j\phi} - [Z^- - Z_0]e^{j\phi}} \\ &= \frac{-jZ^- \sin\phi - Z_0 \cos\phi}{-jZ^- \sin\phi + Z_0 \cos\phi} \end{aligned}$$

Therefore, by (3.25)

$$R(s)|_{B^+} = R(s)|_{B^-}.$$

As a result,

$$\int_{l_1+l_2+l_3} R(s)|_{B^+} e^{st}\, ds + \int_{l_4+l_5+l_6} R(s)|_{B^-} e^{st}\, ds = 0 \tag{3.26}$$

The integral contributions from the third group and the other complex poles can be determined by calculating the residues of $R(s)e^{st}$ at the poles. It is found that all of the poles of $R(s)$ are of first order and thus

$$Res\left[R(s)e^{st},\ poles\right]|_{s=s_k} = \lim_{s\to s_k}(s - s_k)\left[\frac{\Gamma(s) - e^{-s\tau(s)}}{1 - \Gamma(s)e^{-s\tau(s)}}e^{st}\right] = A_k e^{s_k t}, \tag{3.27}$$

where

$$A_k = -\frac{\Gamma(s_k) - e^{-s_k\tau(s_k)}}{\frac{d}{ds}\left[\Gamma(s)e^{-s\tau(s)}\right]|_{s=s_k}} \tag{3.28}$$

is the complex natural mode amplitude. Carrying out the details gives

$$A_k = e^{-\frac{2\Delta}{\nu}\sqrt{s}\sqrt{s-s_0}}\left[G(s) - \frac{\Delta}{\nu}\Gamma(s)\frac{2s-s_0}{\sqrt{s}\sqrt{s-s_0}}\right], \tag{3.29}$$

where

$$G(s) = \frac{2\cos\theta_i\sqrt{\bar{\epsilon}}\sqrt{s}\sqrt{s-s_0} - \cos\theta_i\sqrt{\bar{\epsilon}}\frac{2s^2-ss_0}{\sqrt{s}\sqrt{s-s_0}}}{s^2\cos^2\theta_i + 2s\sqrt{\bar{\epsilon}}\sqrt{s}\sqrt{s-s_0} + \bar{\epsilon}s(s-s_0)},$$

for perpendicular polarization and

$$G(s) = \frac{\cos\theta_i(s\epsilon_r + \frac{\sigma}{\epsilon_0})\sqrt{\bar{\epsilon}}\frac{2s-s_0}{\sqrt{s}\sqrt{s-s_0}} - 2\epsilon_r\cos\theta_i\sqrt{\bar{\epsilon}}\sqrt{s}\sqrt{s-s_0}}{\bar{\epsilon}s(s-s_0) + 2\cos\theta_i(s\epsilon_r + \frac{\sigma}{\epsilon_0})\sqrt{\bar{\epsilon}}\sqrt{s}\sqrt{s-s_0} + \cos^2\theta_i(s\epsilon_r + \frac{\sigma}{\epsilon_0})^2}$$

for parallel polarization.

Collecting the results from (3.20)-(3.29), the impulse response $r(t)$ becomes

$$r(t) = \frac{1}{j2\pi}\int_{B_r} R(s)e^{st}\,ds = \sum A_k e^{s_k t}, \quad t > \tau_0\,, \tag{3.30}$$

and thus the late-time period is a pure natural resonance series, and contains no branch-cut contribution.

3.3.2 Case II: $t < \tau_0$

For $t < \tau_0$, $r(t)$ is found by computing the inverse Laplace transform of $R(s) = \Gamma(s) + \overline{R}(s)$, where

$$\overline{R}(s) = R(s) - \Gamma(s) = \left[\Gamma^2(s) - 1\right]\frac{e^{-s\tau(s)}}{1 - \Gamma(s)e^{-s\tau(s)}}.$$

Then

$$\overline{R}(t) = \mathcal{L}^{-1}\left\{\overline{R}(s)\right\} = \frac{1}{j2\pi}\int_{Br}\left[\Gamma^2(s)-1\right]\frac{e^{-s\tau(s)}}{1-\Gamma(s)e^{-s\tau(s)}}e^{st}ds.$$

To compute this integral, the integration contour is closed in the right half plane, as shown in Figure 3.16. On Γ_∞, from (3.7),

$$\begin{aligned}\mathrm{Re}\left\{\tau(s)\right\} &= \mathrm{Re}\left\{\lim_{\mathrm{Re}\{s\}\to\infty}\frac{2\Delta}{\nu}\sqrt{1+\frac{\sigma}{s\epsilon_0\bar{\epsilon}}}\right\}\\ &\simeq \frac{2\Delta}{\nu} = \tau_0\end{aligned}$$

If we let $t_1 = t - \tau_0$, which is negative since we are evaluating the integral when $t < \tau_0$, then

$$\int_{\Gamma_\infty}\overline{R}(s)e^{st}\,\mathrm{d}s = \int_{\Gamma_\infty}\left[\Gamma^2(s)-1\right]\frac{e^{-s\tau(s)}e^{s\tau_0}}{1-\Gamma(s)e^{-s\tau(s)}}e^{st_1}\,\mathrm{d}s = \int_{\Gamma_\infty}f(s)e^{st_1}\,\mathrm{d}s$$

Here, it is not possible to apply *Jordan's Lemma* directly, since $f(s)$ does not approach zero over the entire contour Γ_∞. However, if we use the theorem introduced earlier, it can be argued that

$$\int_{\Gamma_\infty}\overline{R}(s)e^{st}\,\mathrm{d}s = 0$$

The inverse transform of $\Gamma(s)$, denoted as $\Gamma(t)$, can be found in [26] and [27]. As a result, when $t < \tau_0$, $r(t)$ becomes

$$r(t) = \Gamma(t), \quad t < \tau_0. \tag{3.31}$$

Combining the results (3.30) and (3.31), the impulse response $r(t)$ is

$$r(t) = \begin{cases}\sum A_k e^{s_k t}, & t > \tau_0\\ \Gamma(t), & t < \tau_0.\end{cases} \tag{3.32}$$

3.4 Results

It has been shown analytically that the early-time response is a specular reflection from the interface between free-space and the dielectric slab, and the late-time response is a pure sum of damped sinusoids. In order to verify these results, the natural mode series is compared to the direct IFFT using a truncated Gaussian pulse as the input waveform. This waveform is given by $f(t) = e^{-\pi(t-\mu)^2/\tau^2}$, where τ and μ are 0.1 and 0.15 ns respectively, and is shown in the inset of Figure 3.17. Figures 3.17-3.25 show the transient responses calculated by the natural mode series and the IFFT. In addition, the IFFT of the interfacial reflection coefficients $\Gamma(s)$ are also shown in order to explain the early-time behavior. The natural resonant frequencies of the corresponding cases are shown in Table 3.1-3.9.

As an example of the results, in Figure 3.19 the incident wave is in perpendicular polarization with an incidence angle of 20°, and the material parameters are $\Delta = 2$ cm, $\epsilon_r = 9$ and $\sigma = 0.1$ S/m. Therefore, the beginning of the impulse response late-time, i.e., the two-way transit time of the wave inside the slab, is $\tau_0 = 0.397$ ns. As shown in Figure 3.19, during the early-time period, before τ_0, the IFFT of $R(\omega)F(\omega)$ (where $F(\omega)$ is the spectrum of the input waveform) matches well with the IFFT of $\Gamma(\omega)F(\omega)$, which is the specular reflection from the interface. During the late-time, the IFFT of $R(\omega)F(\omega)$ matches well with the natural mode series. It should be noted that when $t < \tau_0$ the response from the natural mode series does not have any meaning; i.e., the natural mode series is valid only when $t > \tau_0$, the late-time period. Since the frequency band of the input waveform is roughly $0 - 20$ GHz, it was found that the first 7 natural modes, which are shown in Table 3.3, are sufficient to represent the late-time reflected field.

Figure 3.17 shows the response from the lossless, normal incidence case. As seen in the figure, there are equally spaced replicas of the input waveform with gradually diminishing amplitudes during the late-time period. Note that the

amplitude of the first peak is greater than that of the specular reflection in this case.

Comparing Figures 3.20 and 3.21 to Figures 3.18 and 3.19, due to the relatively higher conductivity in the Figure 3.20 and 3.21 cases, relatively smaller late-time responses are observed. The corresponding natural resonance frequencies for these cases are shown in Tables 3.4 and 3.5, and it is seen that the first mode poles of these cases are purely real.

The responses from both polarizations with the incidence angle $\theta_i = 70°$, which is close to the lossless case Brewster angle, are shown in Figures 3.22 and 3.23. As seen in Figure 3.22, the interfacial reflection is very small compared to the first peak of the late-time response for the parallel polarization case. Also, note that no subsequent late-time response is observed for this case. This property is not observed for perpendicular polarization case, as shown in Figure 3.23.

Figures 3.24 and 3.25 show the responses when the incidence angle is large (85°) for parallel and perpendicular polarization respectively. As seen in Table 3.8, the parallel polarization case has a real pole with a relatively smaller amplitude. As a result, the late-time response from the parallel case shows a slower decay rate than the perpendicular case. On the other hand, it is observed that the late-time response from the perpendicular case is smaller than the parallel case due to its high interfacial reflection.

Table 3.1: Poles and corresponding complex natural mode amplitudes (A_k), loseless case ($\epsilon_r = 9$, $\Delta = 2$ cm, $\theta_i = 0°$)

	Pole Amplitude		Natural Mode Amplitude	
	Real Part	Imaginary Part	Real Part	Imaginary Part
mode 0	$-.17329 \times 10^{10}$	$.78540 \times 10^{10}$	$.37500 \times 10^{10}$	$.70819 \times 10^{-6}$
mode 1	$-.17329 \times 10^{10}$	$.23562 \times 10^{11}$	$.37500 \times 10^{10}$	$.26797 \times 10^{-5}$
mode 2	$-.17329 \times 10^{10}$	$.39270 \times 10^{11}$	$.37500 \times 10^{10}$	$.29858 \times 10^{-5}$
mode 3	$-.17329 \times 10^{10}$	$.54978 \times 10^{11}$	$.37500 \times 10^{10}$	$.10715 \times 10^{-5}$
mode 4	$-.17329 \times 10^{10}$	$.70686 \times 10^{11}$	$.37500 \times 10^{10}$	$.58186 \times 10^{-5}$
mode 5	$-.17329 \times 10^{10}$	$.86394 \times 10^{11}$	$.37500 \times 10^{10}$	$.15007 \times 10^{-4}$
mode 6	$-.17329 \times 10^{10}$	$.10210 \times 10^{12}$	$.37500 \times 10^{10}$	$.64309 \times 10^{-5}$

Table 3.2: Poles and corresponding complex natural mode amplitudes (A_k), $\|$ polarization ($\epsilon_r = 9$, $\Delta = 2$ cm, $\theta_i = 20°$, $\sigma = 0.5$ S/m)

	Pole Amplitude		Natural Mode Amplitude	
	Real Part	Imaginary Part	Real Part	Imaginary Part
mode 0	$-.52539 \times 10^{10}$	$.62604 \times 10^{10}$	$.50445 \times 10^{10}$	$.26990 \times 10^{10}$
mode 1	$-.50527 \times 10^{10}$	$.23232 \times 10^{11}$	$.41113 \times 10^{10}$	$.69726 \times 10^{9}$
mode 2	$-.50419 \times 10^{10}$	$.39239 \times 10^{11}$	$.40715 \times 10^{10}$	$.41149 \times 10^{9}$
mode 3	$-.50390 \times 10^{10}$	$.55133 \times 10^{11}$	$.40610 \times 10^{10}$	$.29261 \times 10^{9}$
mode 4	$-.50378 \times 10^{10}$	$.70990 \times 10^{11}$	$.40567 \times 10^{10}$	$.22717 \times 10^{9}$
mode 5	$-.50372 \times 10^{10}$	$.86830 \times 10^{11}$	$.40546 \times 10^{10}$	$.18569 \times 10^{9}$
mode 6	$-.50369 \times 10^{10}$	$.10266 \times 10^{12}$	$.40534 \times 10^{10}$	$.15704 \times 10^{9}$

Table 3.3: Poles and corresponding complex natural mode amplitudes (A_k), $\perp$ polarization ($\epsilon_r = 9$, $\Delta = 2$ cm, $\theta_i = 20°$, $\sigma = 0.1$ S/m)

	Pole Amplitude		Natural Mode Amplitude	
	Real Part	Imaginary Part	Real Part	Imaginary Part
mode 0	$-.23079 \times 10^{10}$	$.77397 \times 10^{10}$	$.36509 \times 10^{10}$	$.32595 \times 10^{9}$
mode 1	$-.22824 \times 10^{10}$	$.23661 \times 10^{11}$	$.35377 \times 10^{10}$	$.11479 \times 10^{9}$
mode 2	$-.22804 \times 10^{10}$	$.39494 \times 10^{11}$	$.35288 \times 10^{10}$	$.69136 \times 10^{8}$
mode 3	$-.22799 \times 10^{10}$	$.55315 \times 10^{11}$	$.35264 \times 10^{10}$	$.49433 \times 10^{8}$
mode 4	$-.22797 \times 10^{10}$	$.71131 \times 10^{11}$	$.35254 \times 10^{10}$	$.38464 \times 10^{8}$
mode 5	$-.22796 \times 10^{10}$	$.86946 \times 10^{11}$	$.35249 \times 10^{10}$	$.31477 \times 10^{8}$
mode 6	$-.22795 \times 10^{10}$	$.10276 \times 10^{12}$	$.35246 \times 10^{10}$	$.26638 \times 10^{8}$

Table 3.4: Poles and corresponding complex natural mode amplitudes (A_k), $\|$ polarization ($\epsilon_r = 9$, $\Delta = 2$ cm, $\theta_i = 30°$, $\sigma = 1.0$ S/m)

	Pole Amplitude		Natural Mode Amplitude	
	Real Part	Imaginary Part	Real Part	Imaginary Part
mode 0	$-.52600 \times 10^{10}$	0.0	$-.68433 \times 10^{10}$	$-.51876 \times 10^{3}$
	$-.12581 \times 10^{11}$	$.19393 \times 10^{10}$	$.10205 \times 10^{11}$	$-.16967 \times 10^{10}$
mode 1	$-.85250 \times 10^{10}$	$.22393 \times 10^{11}$	$.45539 \times 10^{10}$	$.16527 \times 10^{10}$
mode 2	$-.85010 \times 10^{10}$	$.38947 \times 10^{11}$	$.45153 \times 10^{10}$	$.94467 \times 10^{9}$
mode 3	$-.84948 \times 10^{10}$	$.55133 \times 10^{11}$	$.45059 \times 10^{10}$	$.66634 \times 10^{9}$
mode 4	$-.84923 \times 10^{10}$	$.71204 \times 10^{11}$	$.45022 \times 10^{10}$	$.51564 \times 10^{9}$
mode 5	$-.84910 \times 10^{10}$	$.87223 \times 10^{11}$	$.45004 \times 10^{10}$	$.42081 \times 10^{9}$
mode 6	$-.84903 \times 10^{10}$	$.10322 \times 10^{12}$	$.44993 \times 10^{10}$	$.35555 \times 10^{9}$

Table 3.5: Poles and corresponding complex natural mode amplitudes (A_k), $\perp$ polarization ($\epsilon_r = 9$, $\Delta = 2$ cm, $\theta_i = 30°$, $\sigma = 1.5$ S/m).

	Pole Amplitude		Natural Mode Amplitude	
	Real Part	Imaginary Part	Real Part	Imaginary Part
mode 0	$-.33106 \times 10^{10}$	0.0	$-.13299 \times 10^{10}$	$.20254 \times 10^{2}$
mode 1	$-.11233 \times 10^{11}$	$.21104 \times 10^{11}$	$.32151 \times 10^{10}$	$.17600 \times 10^{10}$
mode 2	$-.11227 \times 10^{11}$	$.38219 \times 10^{11}$	$.32366 \times 10^{10}$	$.97606 \times 10^{9}$
mode 3	$-.11225 \times 10^{11}$	$.54621 \times 10^{11}$	$.32421 \times 10^{10}$	$.68370 \times 10^{9}$
mode 4	$-.11224 \times 10^{11}$	$.70808 \times 10^{11}$	$.32443 \times 10^{10}$	$.52763 \times 10^{9}$
mode 5	$-.11224 \times 10^{11}$	$.86900 \times 10^{11}$	$.32454 \times 10^{10}$	$.43002 \times 10^{9}$
mode 6	$-.11224 \times 10^{11}$	$.10294 \times 10^{12}$	$.32460 \times 10^{10}$	$.36305 \times 10^{9}$

Table 3.6: Poles and corresponding complex natural mode amplitudes (A_k), $\|$ polarization ($\epsilon_r = 9$, $\Delta = 2$ cm, $\theta_i = 70°$, $\sigma = 0.5$ S/m)

	Pole Amplitude		Natural Mode Amplitude	
	Real Part	Imaginary Part	Real Part	Imaginary Part
mode 0	$-.37966 \times 10^{10}$	0.0	$-.58702 \times 10^{10}$	$-.55113 \times 10^{3}$
mode 1	$-.10993 \times 10^{11}$	$.21160 \times 10^{11}$	$.10655 \times 10^{11}$	$.48499 \times 10^{11}$
mode 2	$-.11619 \times 10^{11}$	$.39009 \times 10^{11}$	$.39566 \times 10^{11}$	$.45363 \times 10^{11}$
mode 3	$-.11821 \times 10^{11}$	$.56182 \times 10^{11}$	$.52026 \times 10^{11}$	$.36984 \times 10^{11}$
mode 4	$-.11908 \times 10^{11}$	$.73090 \times 10^{11}$	$.57936 \times 10^{11}$	$.30405 \times 10^{11}$
mode 5	$-.11953 \times 10^{11}$	$.89869 \times 10^{11}$	$.61121 \times 10^{11}$	$.25589 \times 10^{11}$
mode 6	$-.11979 \times 10^{11}$	$.10658 \times 10^{12}$	$.63104 \times 10^{11}$	$.22008 \times 10^{11}$

Table 3.7: Poles and corresponding complex natural mode amplitudes (A_k), $\perp$ polarization ($\epsilon_r = 9$, $\Delta = 2$ cm, $\theta_i = 70°$, $\sigma = 0.5$ S/m)

	Pole Amplitude		Natural Mode Amplitude	
	Real Part	Imaginary Part	Real Part	Imaginary Part
mode 0	$-.41396 \times 10^{10}$	$.71833 \times 10^{10}$	$.13691 \times 10^{10}$	$.67111 \times 10^{9}$
mode 1	$-.41206 \times 10^{10}$	$.24473 \times 10^{11}$	$.12906 \times 10^{10}$	$.18876 \times 10^{9}$
mode 2	$-.41192 \times 10^{10}$	$.41150 \times 10^{11}$	$.12854 \times 10^{10}$	$.11193 \times 10^{9}$
mode 3	$-.41188 \times 10^{10}$	$.57748 \times 10^{11}$	$.12840 \times 10^{10}$	$.79695 \times 10^{8}$
mode 4	$-.41187 \times 10^{10}$	$.74320 \times 10^{11}$	$.12835 \times 10^{10}$	$.61904 \times 10^{8}$
mode 5	$-.41186 \times 10^{10}$	$.90880 \times 10^{11}$	$.12832 \times 10^{10}$	$.50615 \times 10^{8}$
mode 6	$-.41186 \times 10^{10}$	$.10743 \times 10^{12}$	$.12830 \times 10^{10}$	$.42811 \times 10^{8}$

Table 3.8: Poles and corresponding complex natural mode amplitudes (A_k), $\|$ polarization ($\epsilon_r = 9$, $\Delta = 2$ cm, $\theta_i = 85°$, $\sigma = 0.5$ S/m)

	Pole Amplitude		Natural Mode Amplitude	
	Real Part	Imaginary Part	Real Part	Imaginary Part
mode 0	$-.11692 \times 10^{10}$	0.0	$-.21180 \times 10^{10}$	$.20153 \times 10^{3}$
mode 1	$-.50128 \times 10^{10}$	$.16532 \times 10^{11}$	$-.30588 \times 10^{10}$	$.57062 \times 10^{9}$
mode 2	$-.50326 \times 10^{10}$	$.33249 \times 10^{11}$	$-.31490 \times 10^{10}$	$.30084 \times 10^{9}$
mode 3	$-.50365 \times 10^{10}$	$.49921 \times 10^{11}$	$-.31678 \times 10^{10}$	$.20275 \times 10^{9}$
mode 4	$-.50379 \times 10^{10}$	$.66584 \times 10^{11}$	$-.31745 \times 10^{10}$	$.15265 \times 10^{9}$
mode 5	$-.50386 \times 10^{10}$	$.83242 \times 10^{11}$	$-.31777 \times 10^{10}$	$.12234 \times 10^{9}$
mode 6	$-.50390 \times 10^{10}$	$.99899 \times 10^{11}$	$-.31794 \times 10^{10}$	$.10205 \times 10^{9}$

Table 3.9: Poles and corresponding complex natural mode amplitudes (A_k), $\perp$ polarization ($\epsilon_r = 9$, $\Delta = 2$ cm, $\theta_i = 85°$, $\sigma = 0.5$ S/m)

	Pole Amplitude		Natural Mode Amplitude	
	Real Part	Imaginary Part	Real Part	Imaginary Part
mode 0	$-.36956 \times 10^{10}$	$.74632 \times 10^{10}$	$.33232 \times 10^{9}$	$.15734 \times 10^{9}$
mode 1	$-.36944 \times 10^{10}$	$.24705 \times 10^{11}$	$.32742 \times 10^{9}$	$.46879 \times 10^{8}$
mode 2	$-.36943 \times 10^{10}$	$.41468 \times 10^{11}$	$.32704 \times 10^{9}$	$.27899 \times 10^{8}$
mode 3	$-.36943 \times 10^{10}$	$.58168 \times 10^{11}$	$.32694 \times 10^{9}$	$.19883 \times 10^{8}$
mode 4	$-.36943 \times 10^{10}$	$.74847 \times 10^{11}$	$.32690 \times 10^{9}$	$.15451 \times 10^{8}$
mode 5	$-.36943 \times 10^{10}$	$.91517 \times 10^{11}$	$.32688 \times 10^{9}$	$.12636 \times 10^{8}$
mode 6	$-.36943 \times 10^{10}$	$.10818 \times 10^{12}$	$.32686 \times 10^{9}$	$.10689 \times 10^{8}$

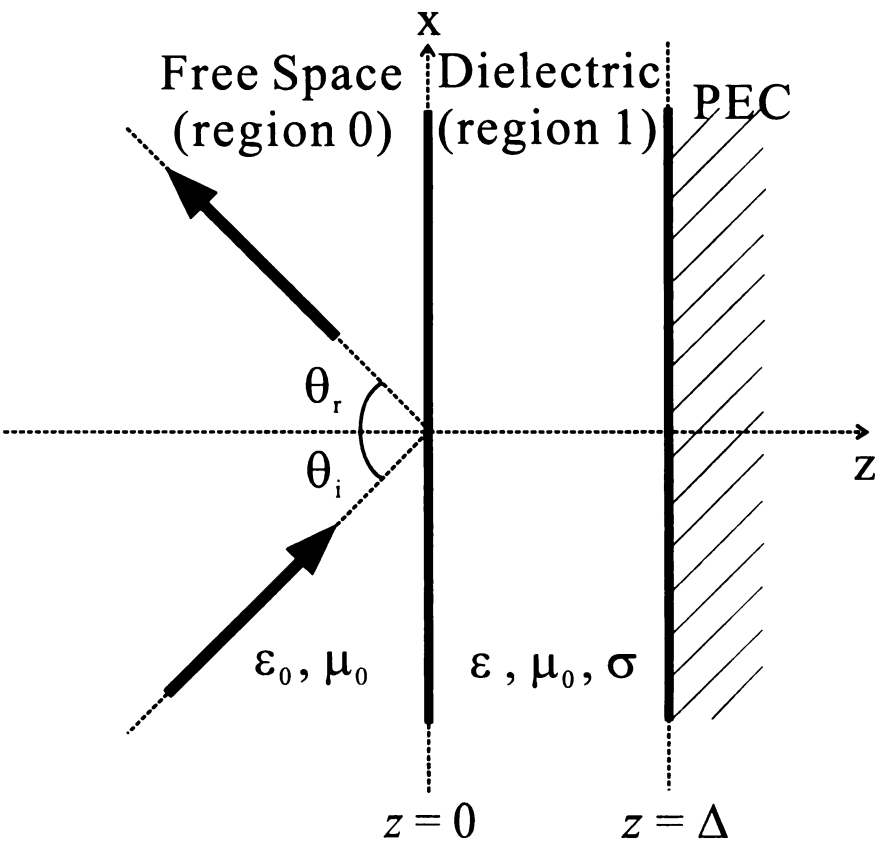

Figure 3.1: A uniform plane wave incident from free space upon a conductor-backed lossy slab.

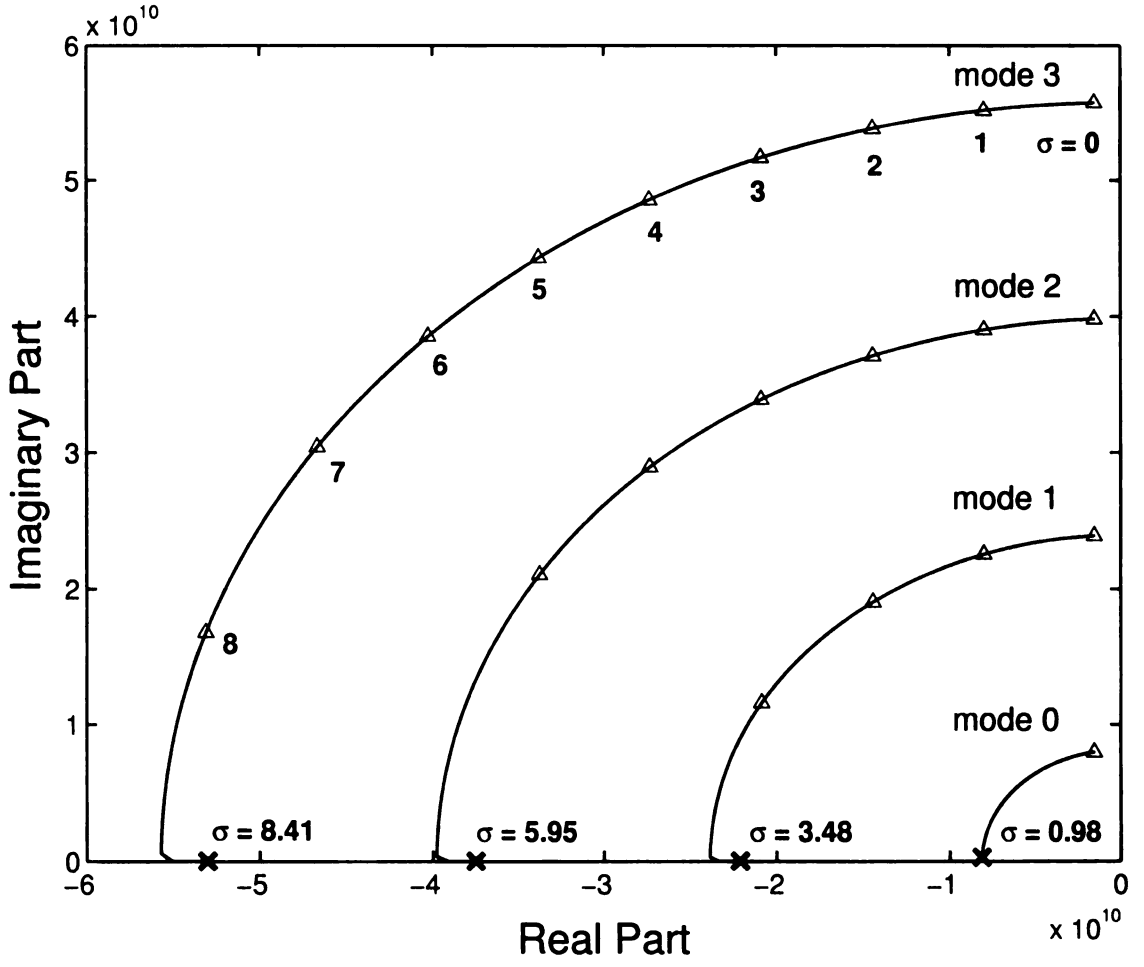

Figure 3.2: Pole trajectories of the reflection coefficient, $\perp$ polarization ($\epsilon_r = 9$, $\Delta = 2$ cm, $\theta_i = 30°$).

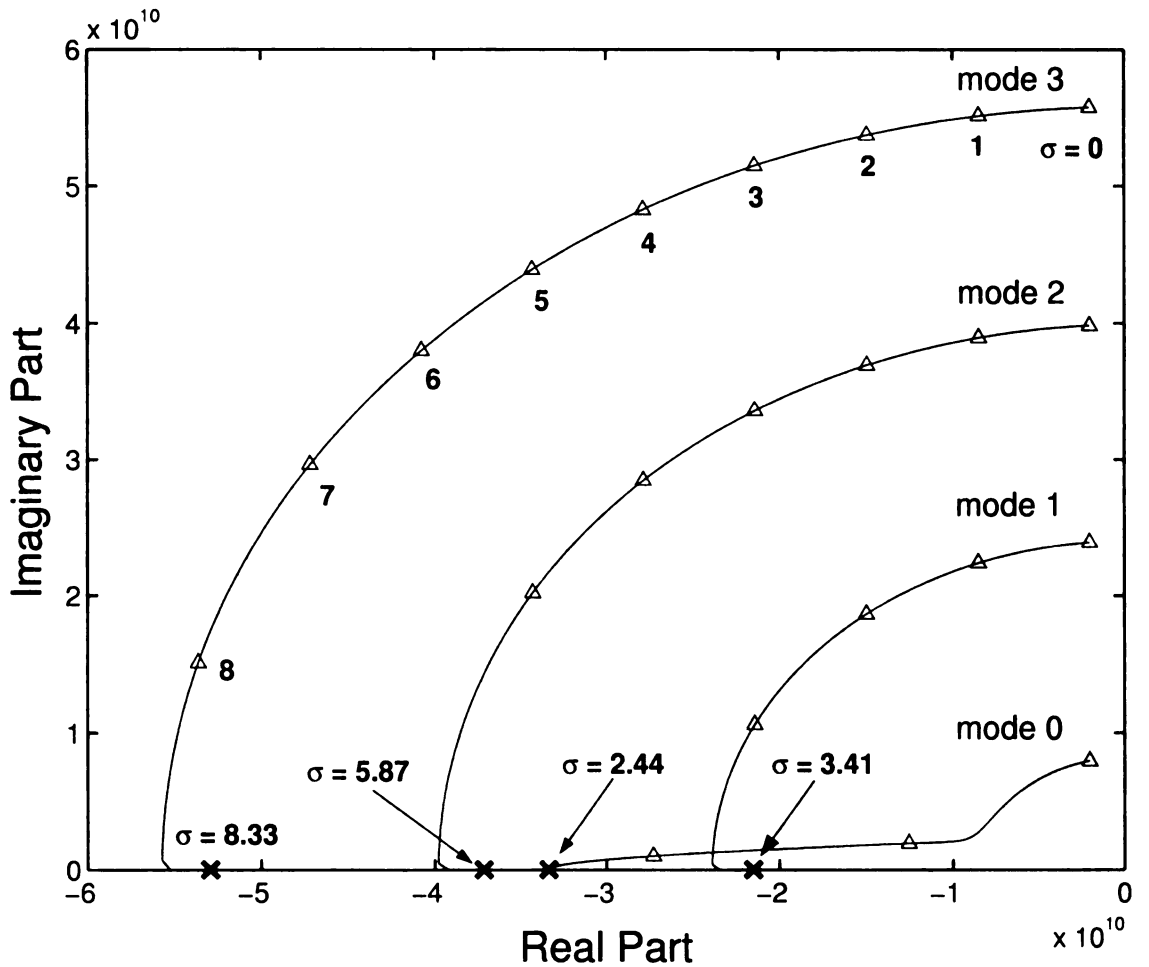

Figure 3.3: Pole trajectories of the reflection coefficient, $\|$ polarization ($\epsilon_r = 9$, $\Delta = 2$ cm, $\theta_i = 30°$).

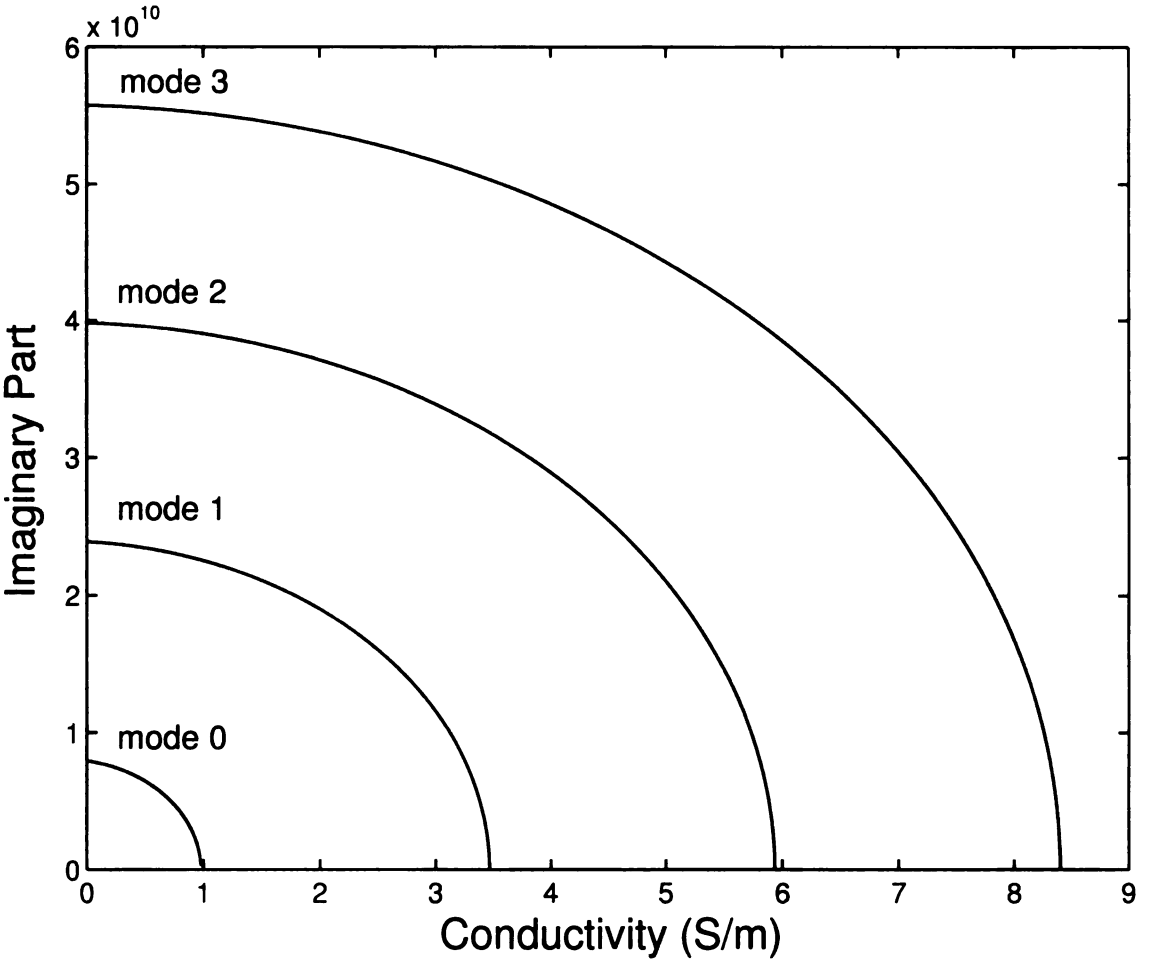

Figure 3.4: The amplitude of the imaginary parts of poles vs. conductivity, $\perp$ polarization ($\epsilon_r = 9$, $\Delta = 2$ cm, $\theta_i = 30°$, $\sigma = 0 \rightarrow 10.0$ S/m).

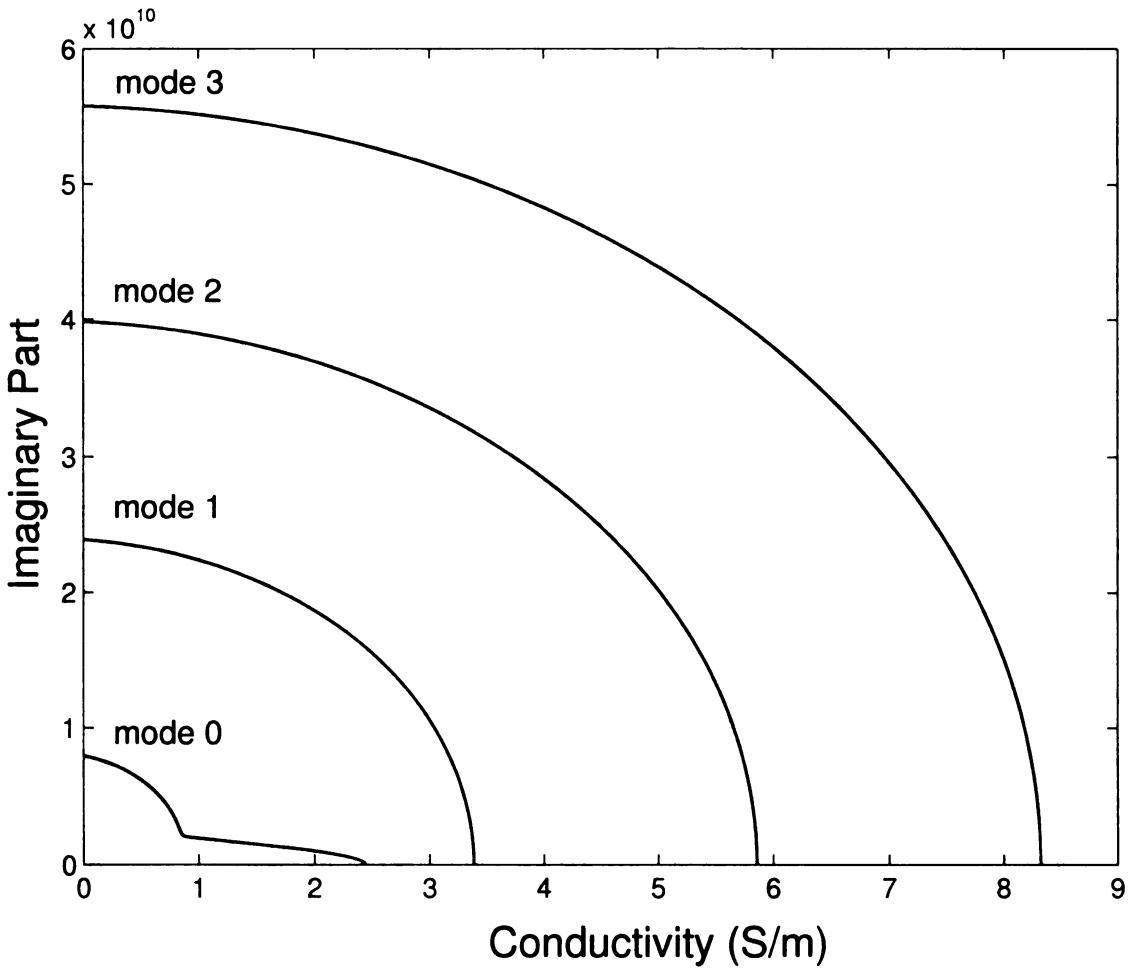

Figure 3.5: The amplitude of the imaginary parts of poles vs. conductivity, $\|$ polarization ($\epsilon_r = 9$, $\Delta = 2$ cm, $\theta_i = 30°$, $\sigma = 0 \rightarrow 10.0$ S/m).

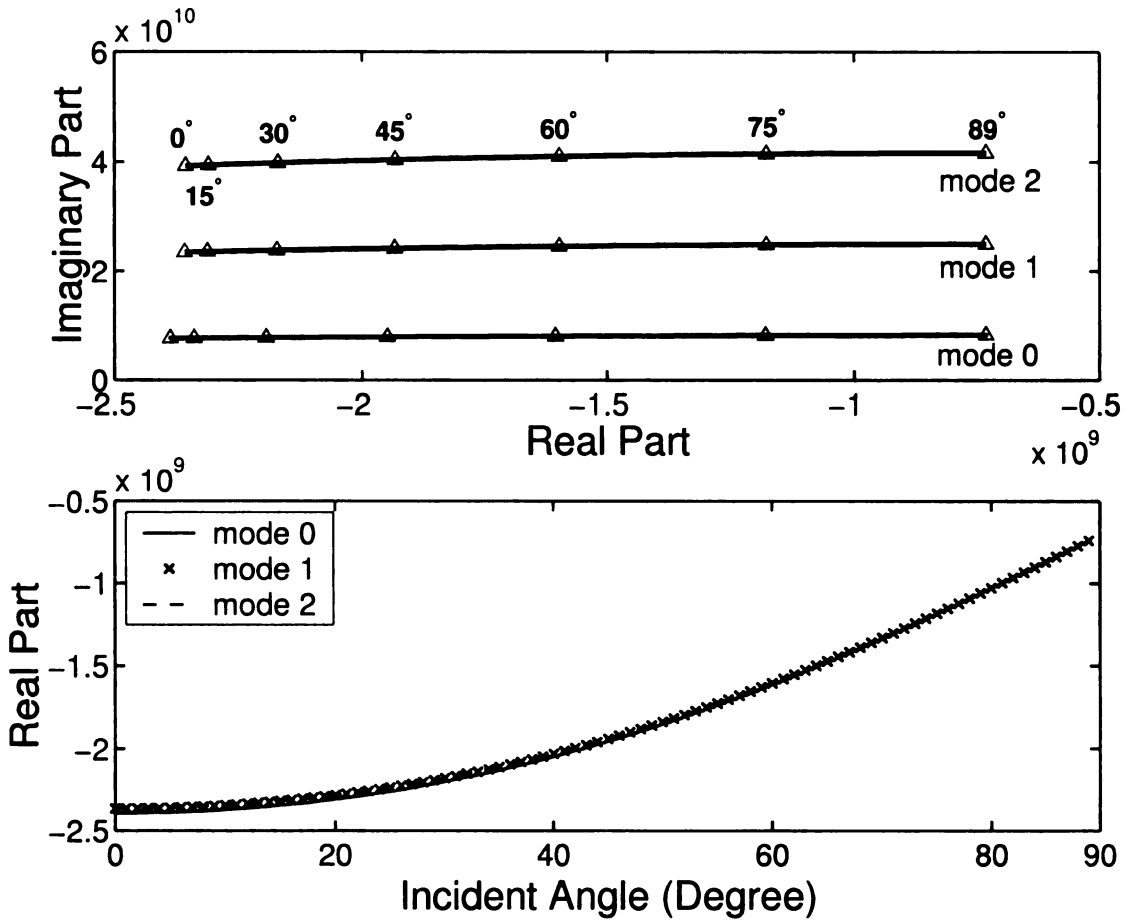

Figure 3.6: Pole trajectories of the reflection coefficient vs. angle of incidence, $\perp$ polarization ($\epsilon_r = 9$, $\Delta = 2$ cm, $\sigma = 0.1$ S/m).

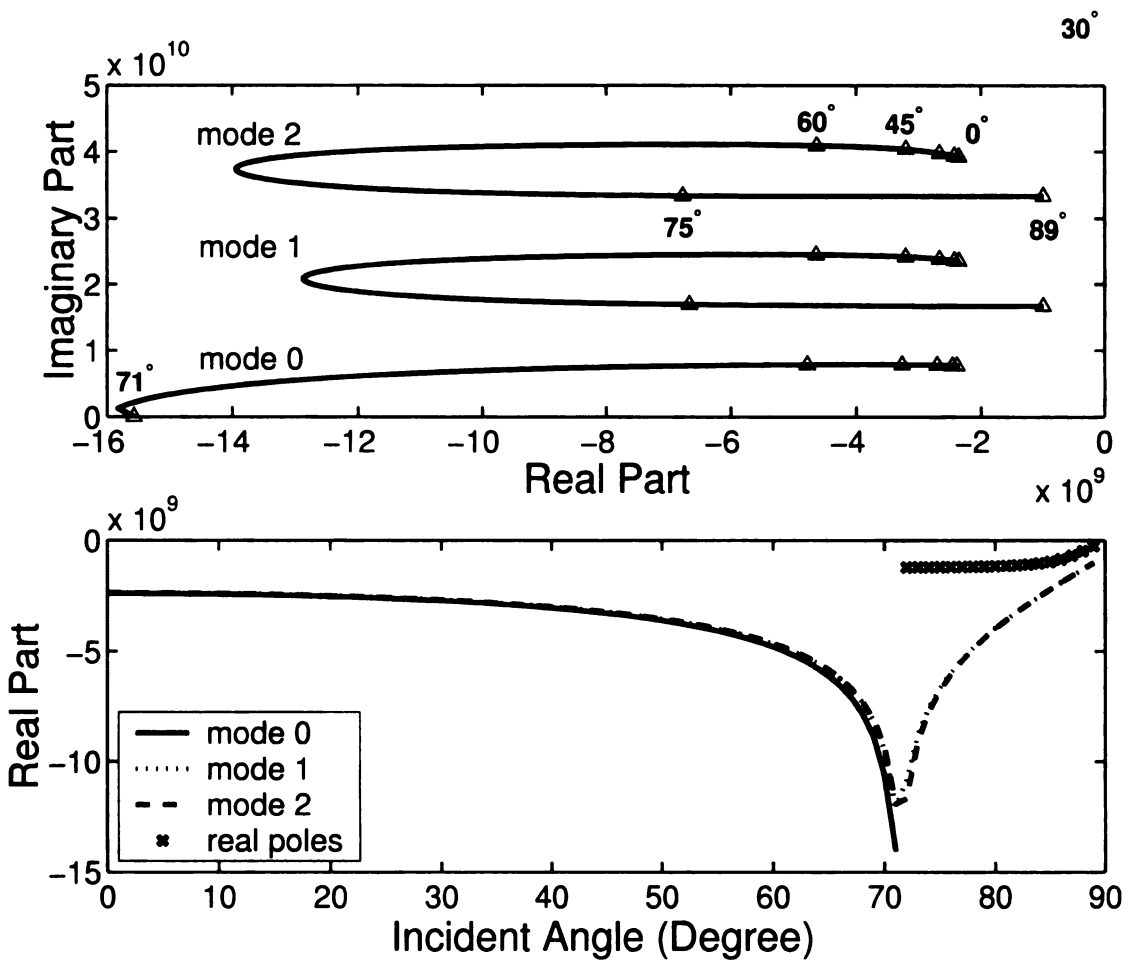

Figure 3.7: Pole trajectories of the reflection coefficient vs. angle of incidence, $\|$ polarization ($\epsilon_r = 9$, $\Delta = 2$ cm, $\sigma = 0.1$ S/m).

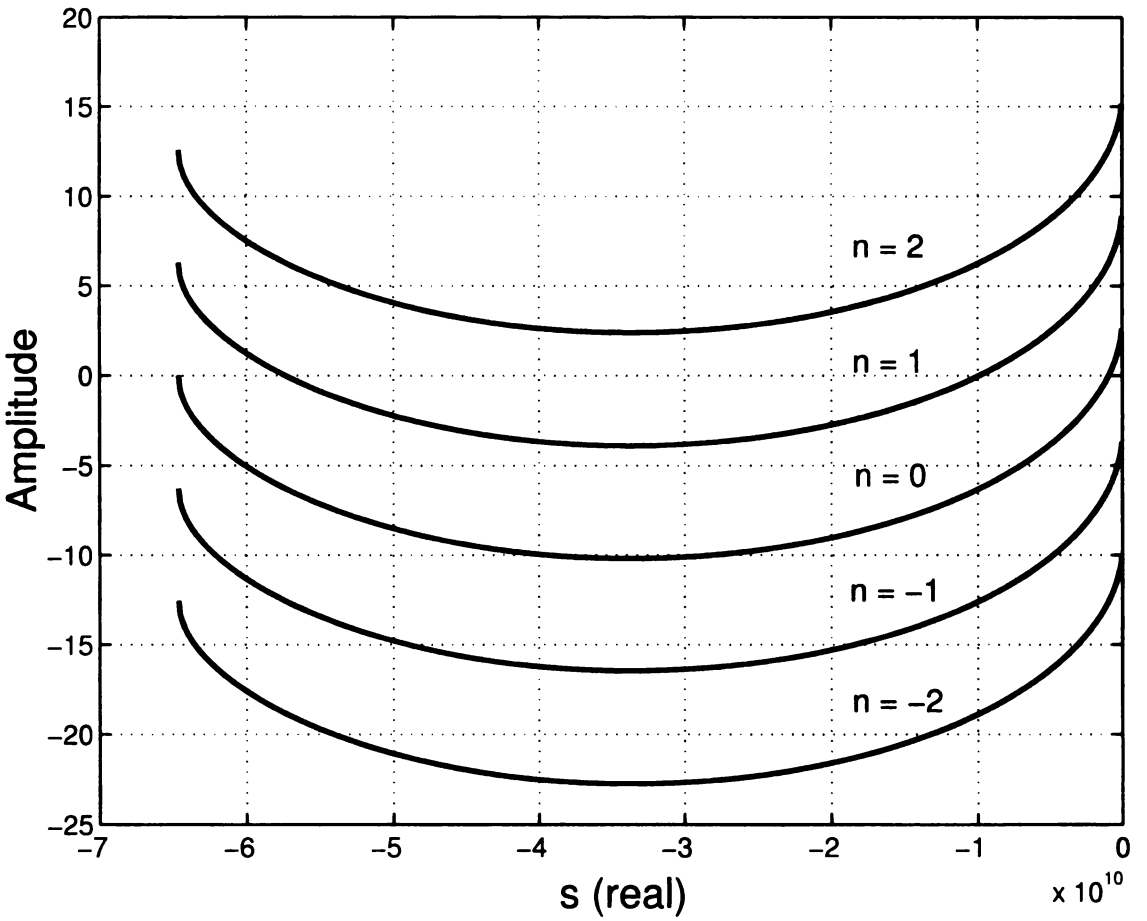

Figure 3.8: Characteristic function vs. real s, $\perp$ polarization ($\epsilon_r = 9$, $\Delta = 2$ cm, $\sigma = 5.0$ S/m, $\theta_i = 30°$).

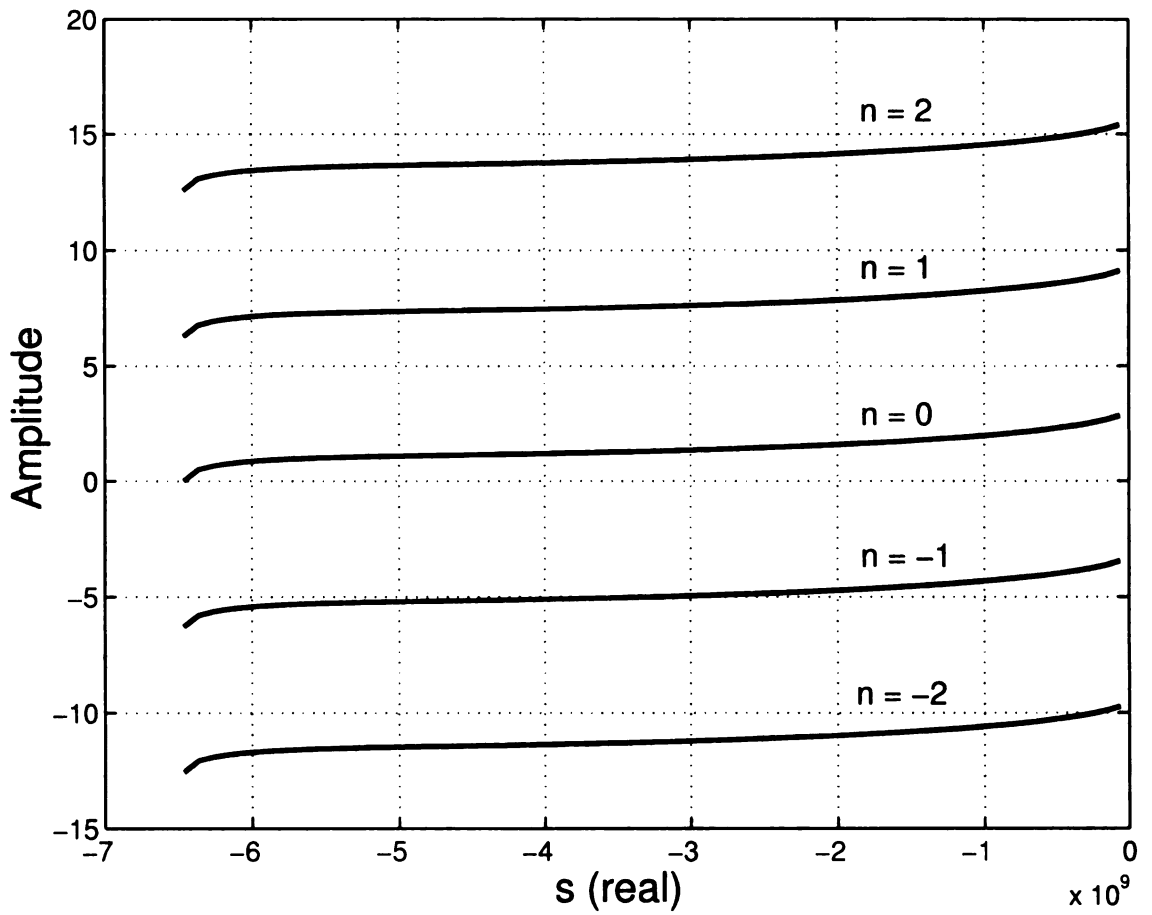

Figure 3.9: Characteristic function vs. real s, $\perp$ polarization ($\epsilon_r = 9$, $\Delta = 2$ cm, $\sigma = 0.5$ S/m, $\theta_i = 30°$).

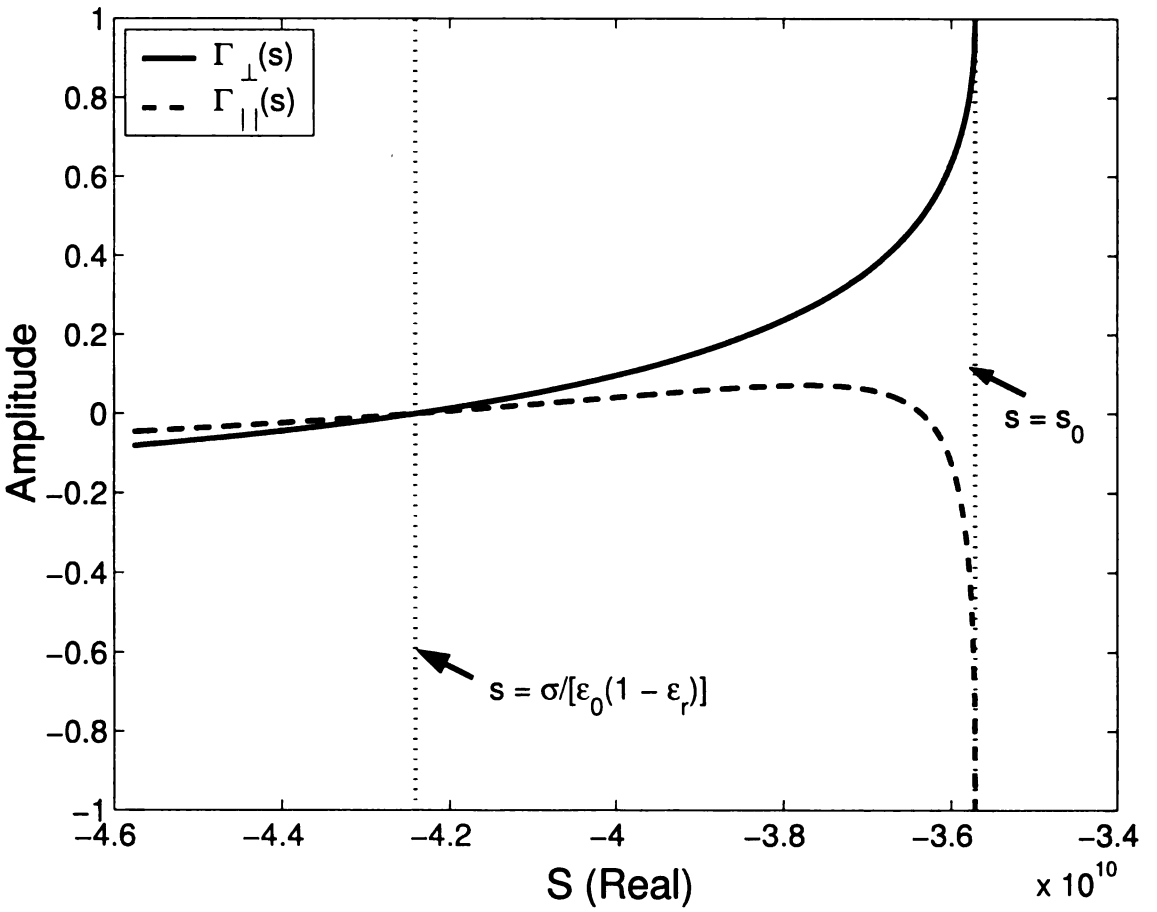

Figure 3.10: Amplitudes of the reflection coefficients ($\epsilon_r = 5$, $\Delta = 2$ cm, $\sigma = 1.5$ S/m, $\theta_i = 30°$).

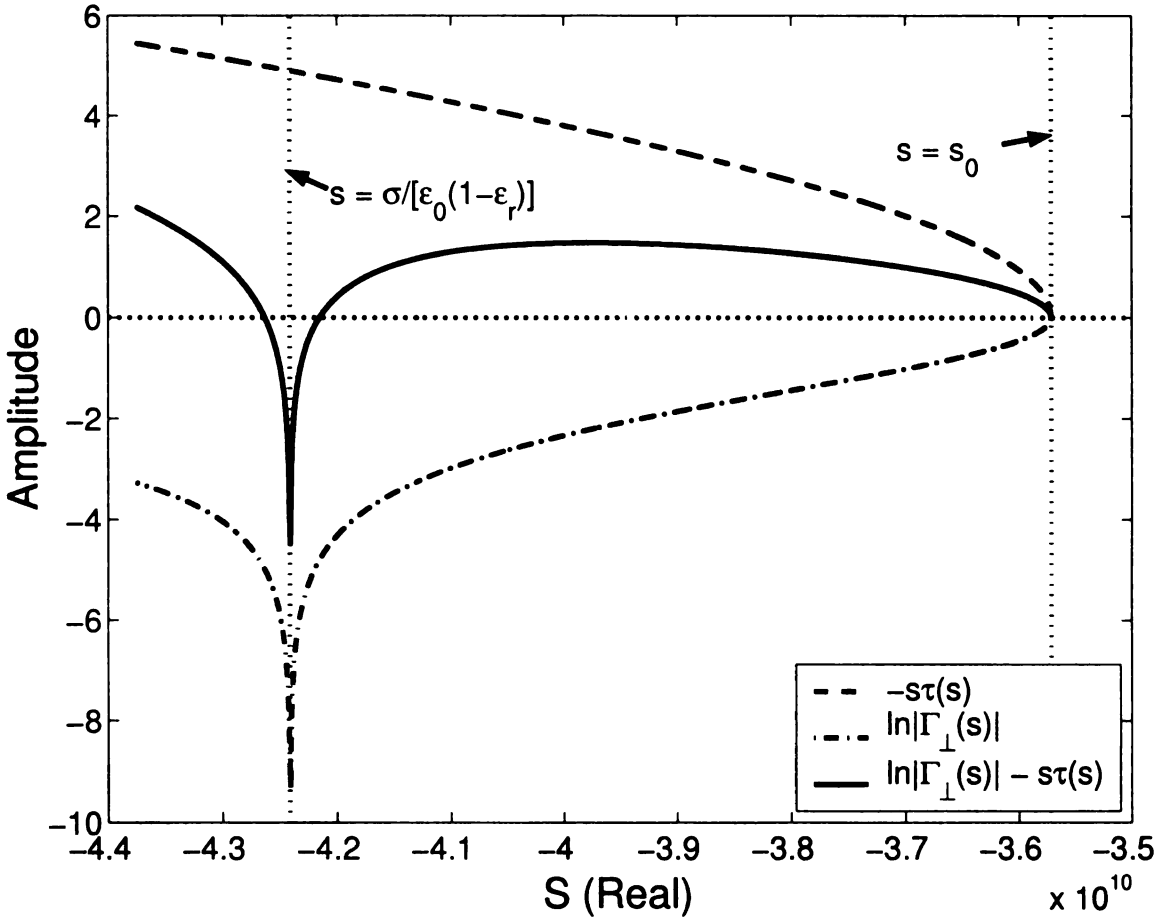

Figure 3.11: Real pole ($s < s_0$), ($\epsilon_r = 5$, $\Delta = 2$ cm, $\sigma = 1.5$ S/m, $\theta_i = 30°$).

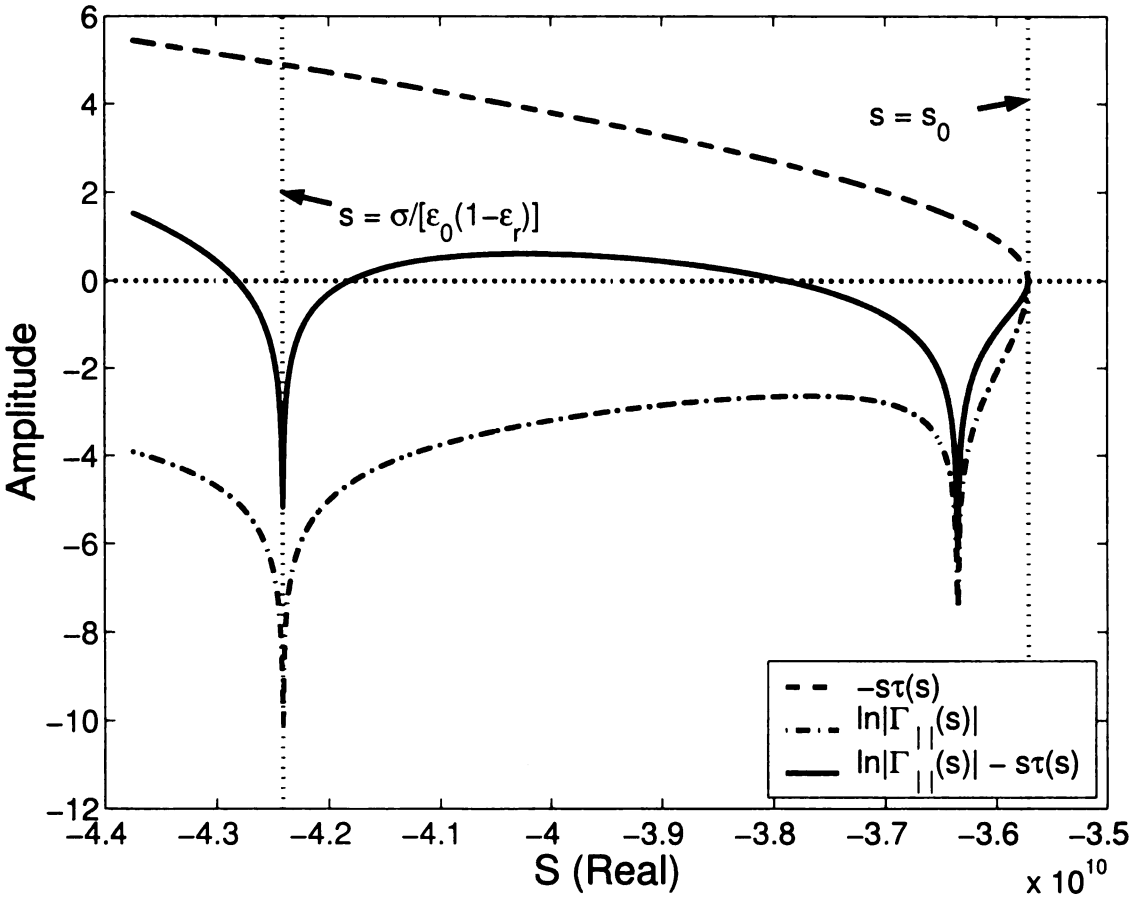

Figure 3.12: Real pole ($s < s_0$), ($\epsilon_r = 5$, $\Delta = 2$ cm, $\sigma = 1.5$ S/m, $\theta_i = 30°$).

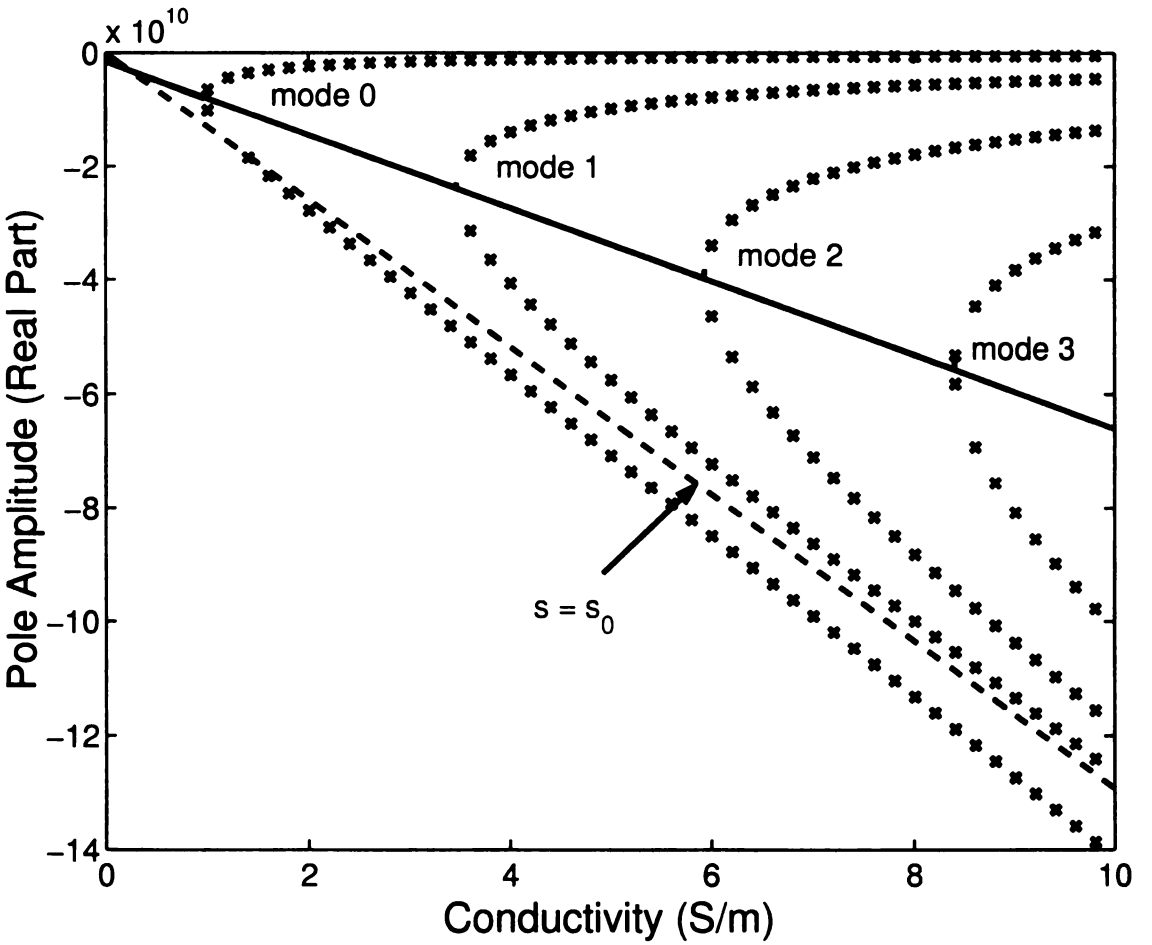

Figure 3.13: Complete sketch of the pole trajectories showing both complex and real poles, $\perp$ polarization ($\epsilon_r = 9$, $\Delta = 2$ cm, $\theta_i = 20°$).

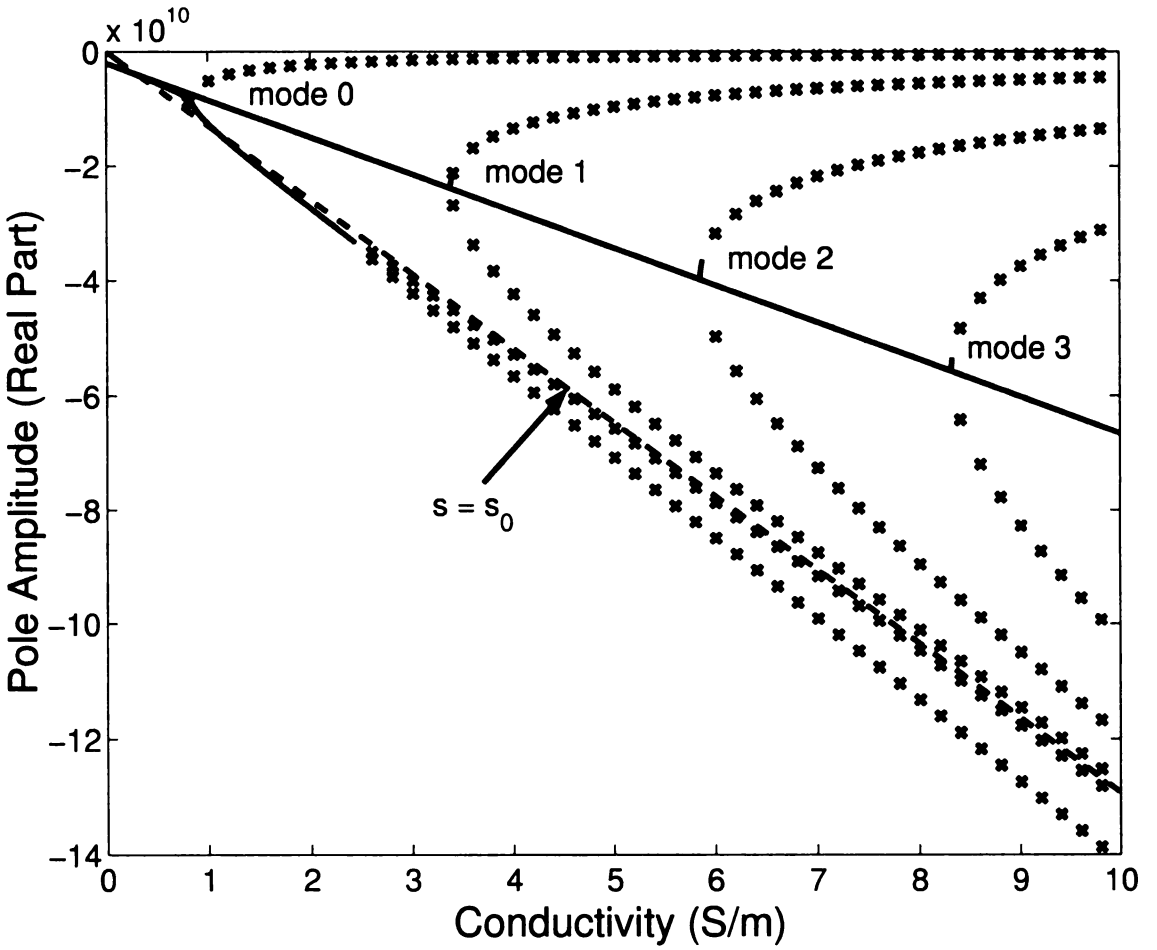

Figure 3.14: Complete sketch of the pole trajectories showing both complex and real poles, $\|$ polarization ($\epsilon_r = 9$, $\Delta = 2$ cm, $\theta_i = 20°$).

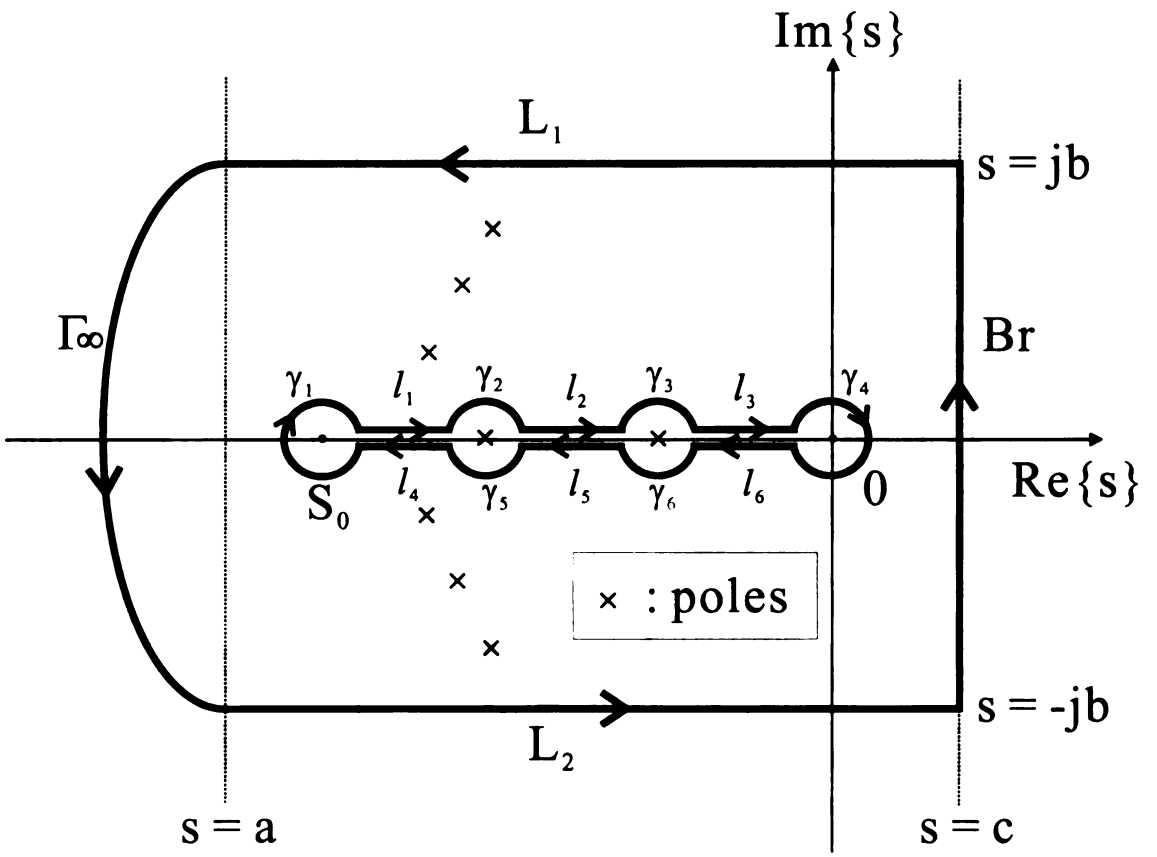

Figure 3.15: The integration contour when $t > \tau_0$. $|a|, |b| \to \infty$, $0 < c < \infty$.

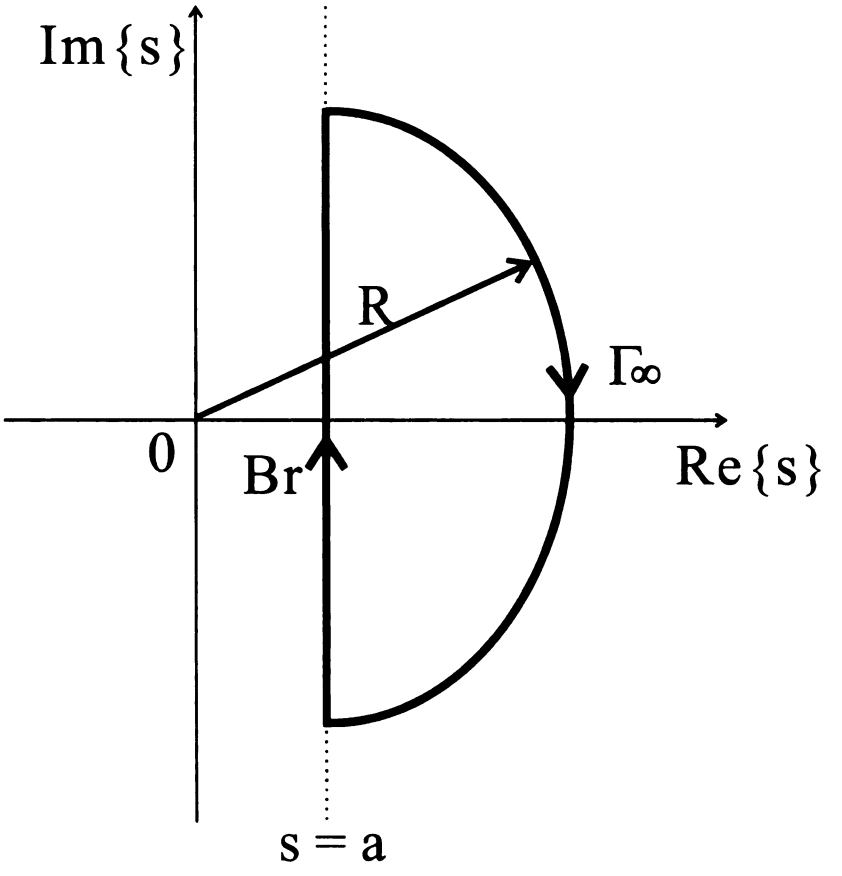

Figure 3.16: The integration contour when $t < \tau_0$. $R \to \infty$, $0 < a < \infty$.

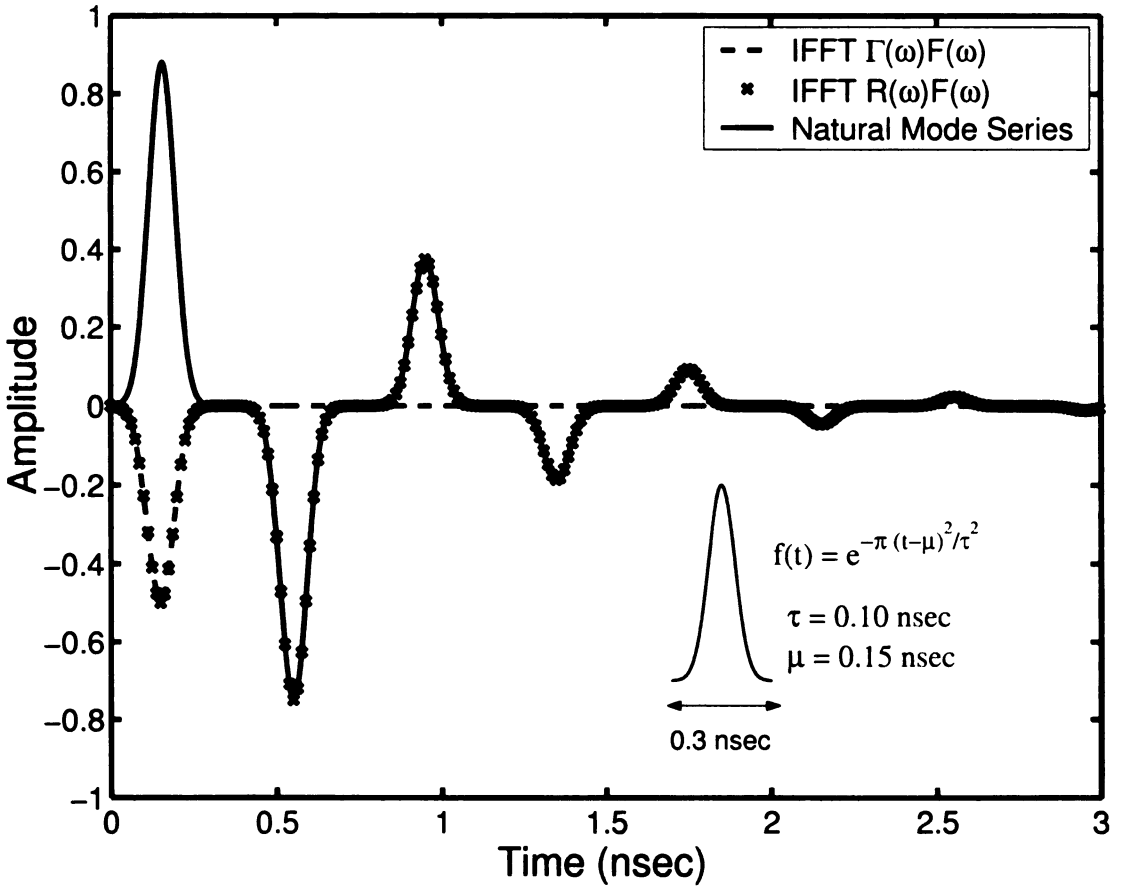

Figure 3.17: Time domain response, lossless case ($\epsilon_r = 9$, $\Delta = 2$ cm, $\theta_i = 0°$). Inset shows equivalent transmitted waveform.

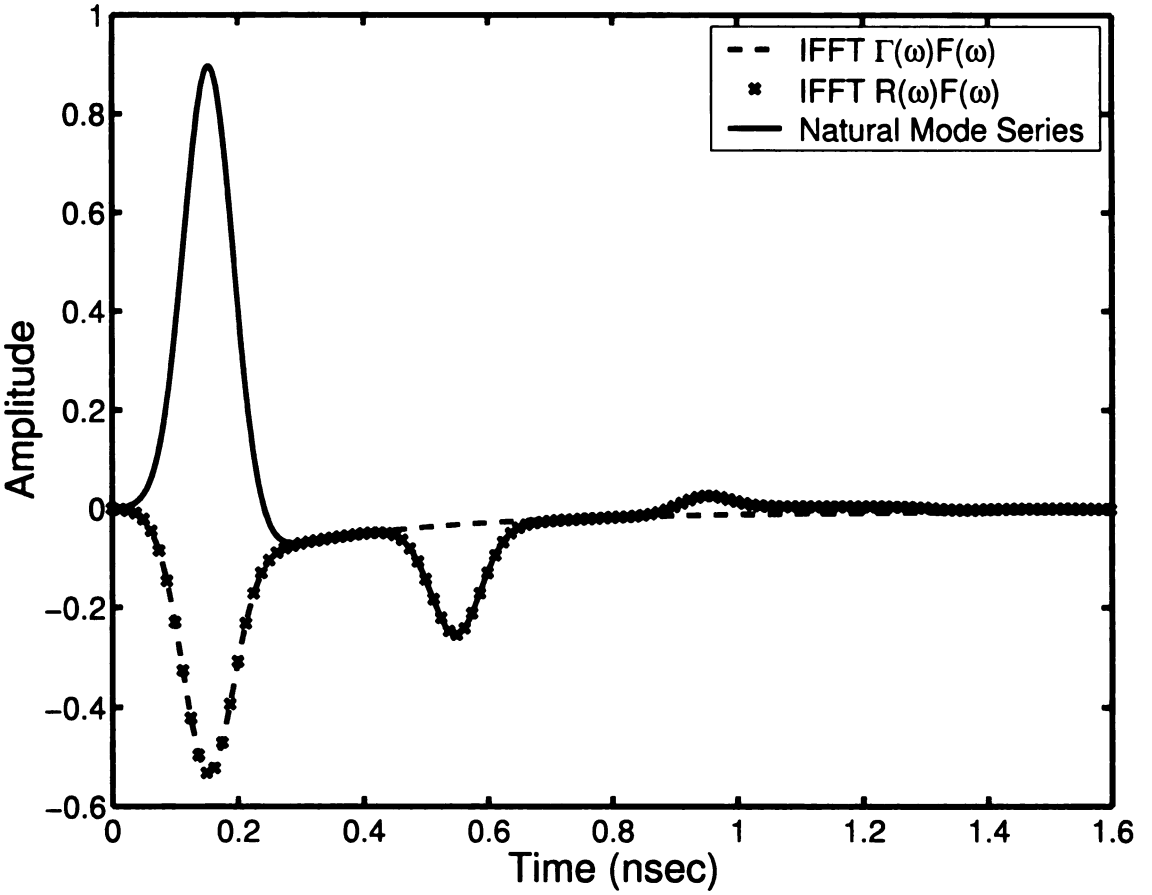

Figure 3.18: Time domain response, || polarization ($\epsilon_r = 9$, $\Delta = 2$ cm, $\theta_i = 20°$, $\sigma = 0.5$ S/m).

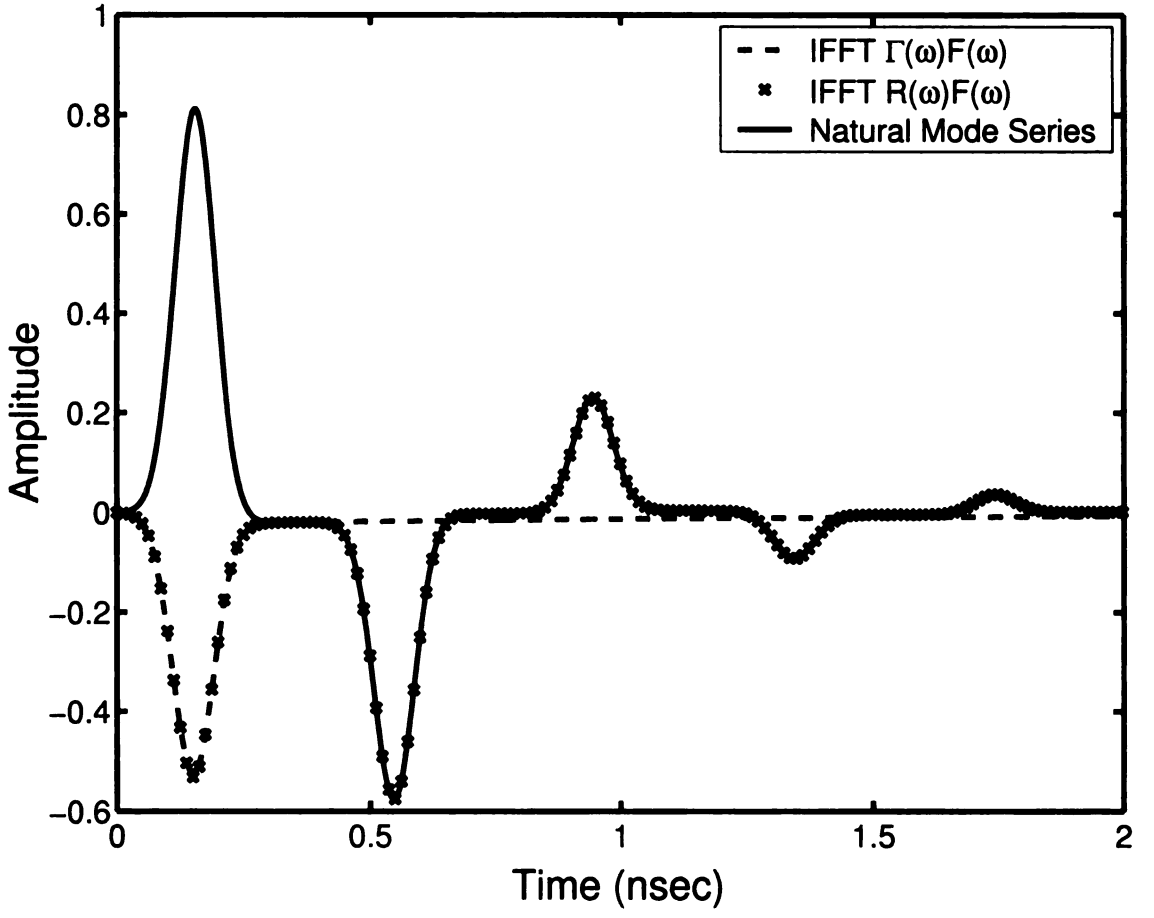

Figure 3.19: Time domain response, $\perp$ polarization ($\epsilon_r = 9$, $\Delta = 2$ cm, $\theta_i = 20°$, $\sigma = 0.1$ S/m).

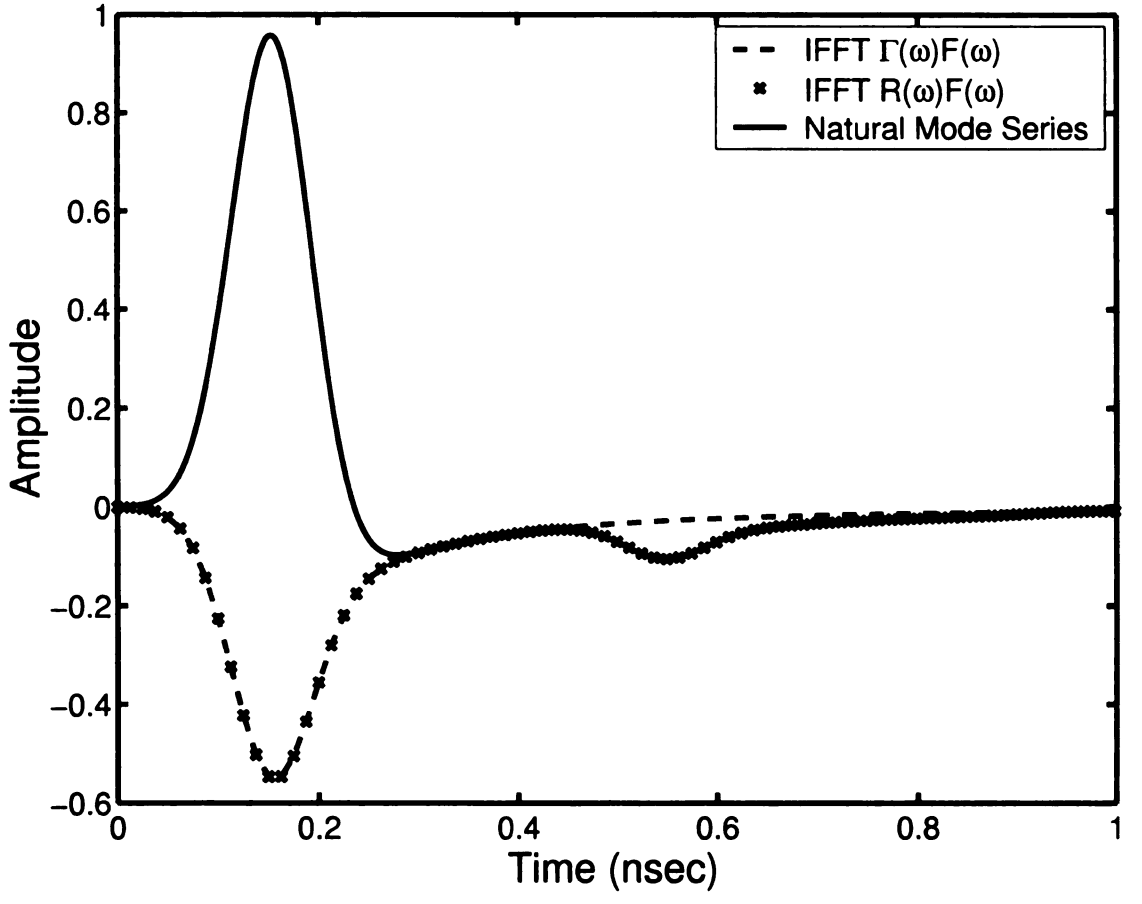

Figure 3.20: Time domain response, $\|$ polarization ($\epsilon_r = 9$, $\Delta = 2$ cm, $\theta_i = 30°$, $\sigma = 1.0$ S/m).

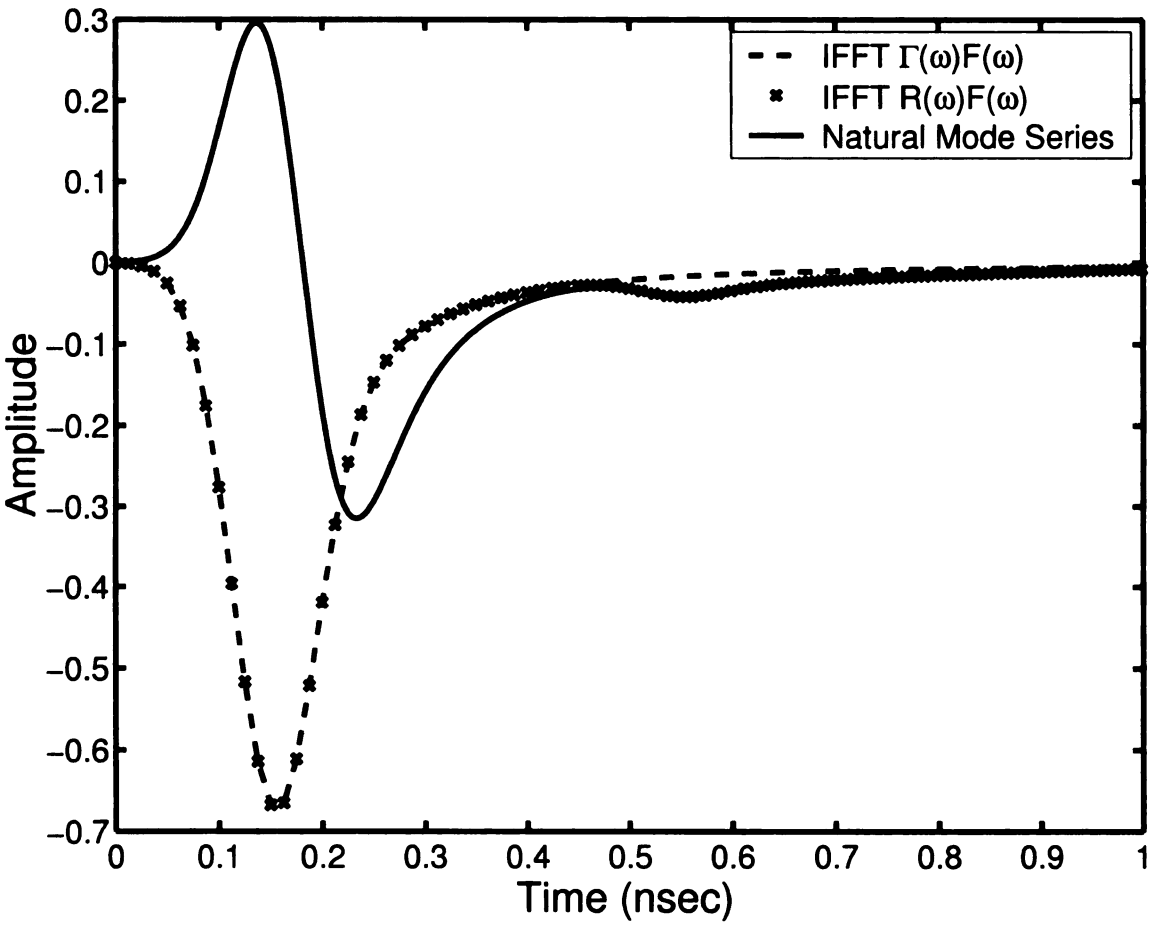

Figure 3.21: Time domain response, $\perp$ polarization ($\epsilon_r = 9$, $\Delta = 2$ cm, $\theta_i = 30°$, $\sigma = 1.5$ S/m).

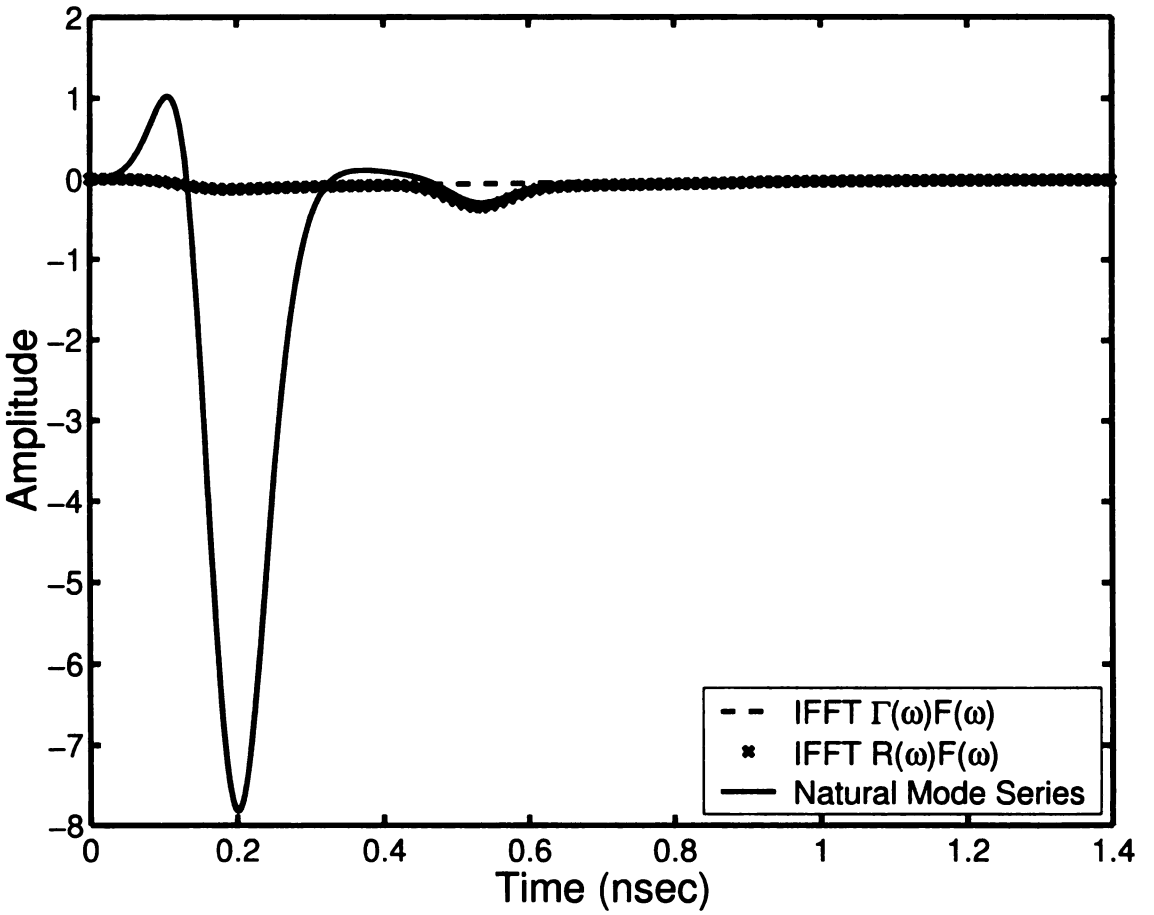

Figure 3.22: Time domain response, || polarization ($\epsilon_r = 9$, $\Delta = 2$ cm, $\theta_i = 70°$, $\sigma = 0.5$ S/m).

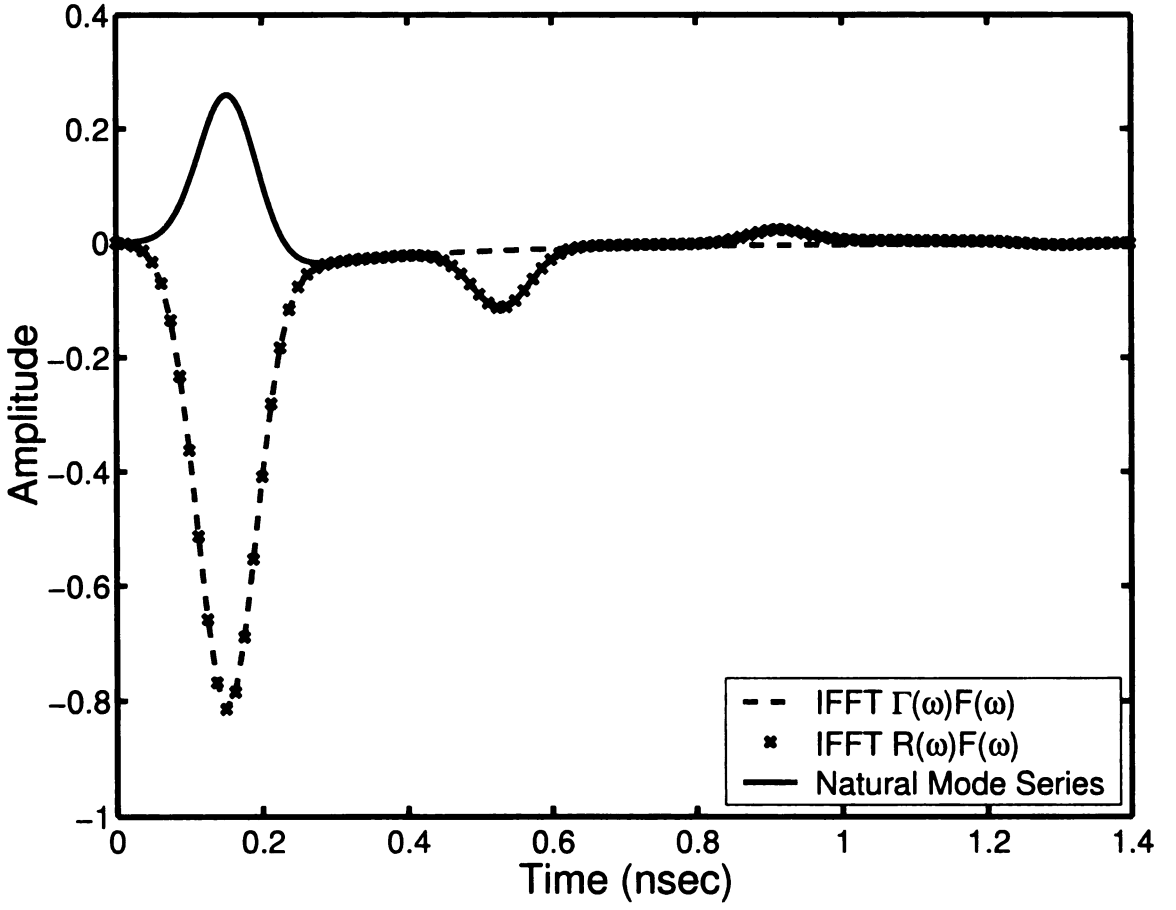

Figure 3.23: Time domain response, $\perp$ polarization ($\epsilon_r = 9$, $\Delta = 2$ cm, $\theta_i = 70°$, $\sigma = 0.5$ S/m).

Figure 3.2
$\sigma = 0.5$ S

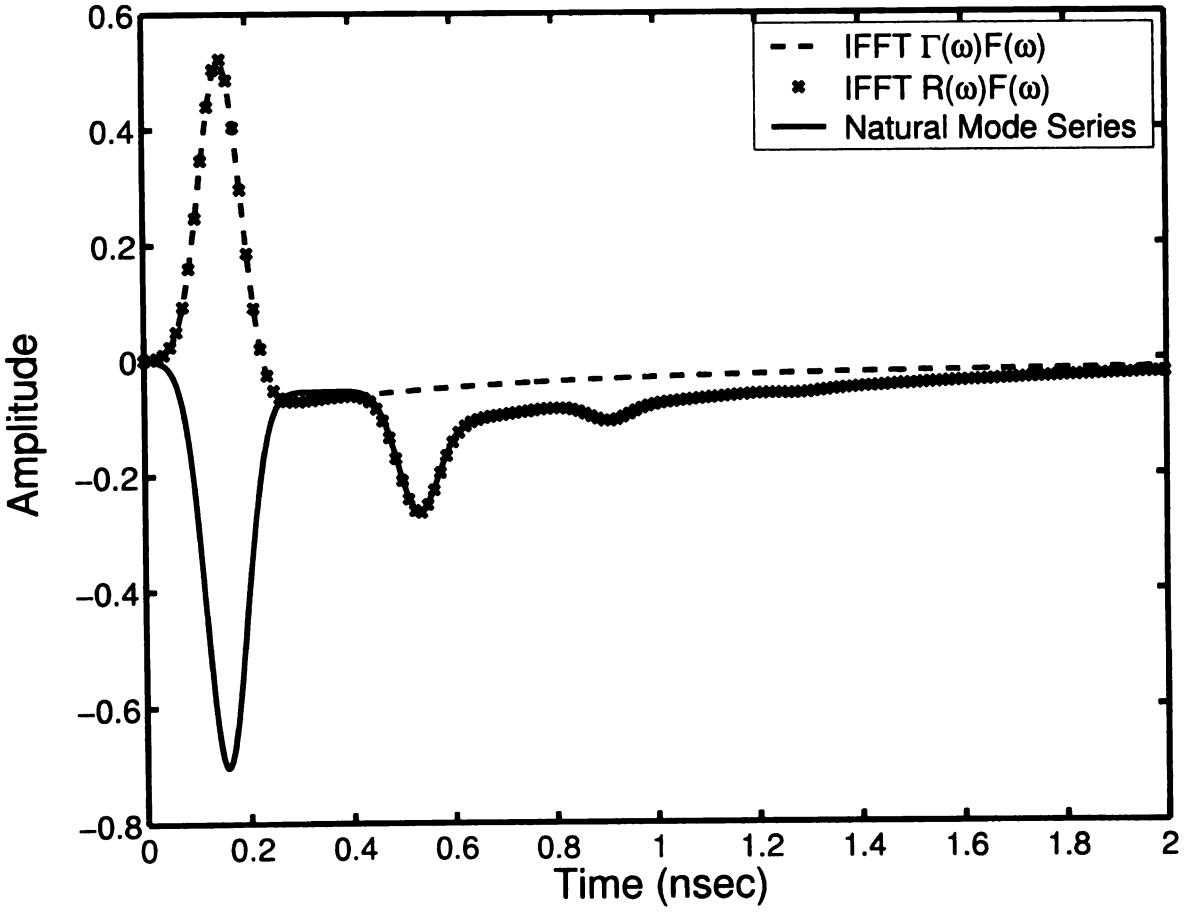

Figure 3.24: Time domain response, $\|$ polarization ($\epsilon_r = 9$, $\Delta = 2$ cm, $\theta_i = 85°$, $\sigma = 0.5$ S/m).

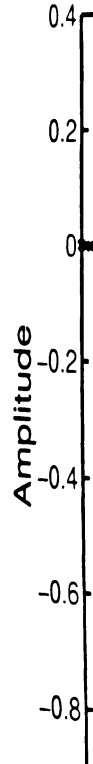

Figure 3.
$\sigma = 0.5$ S

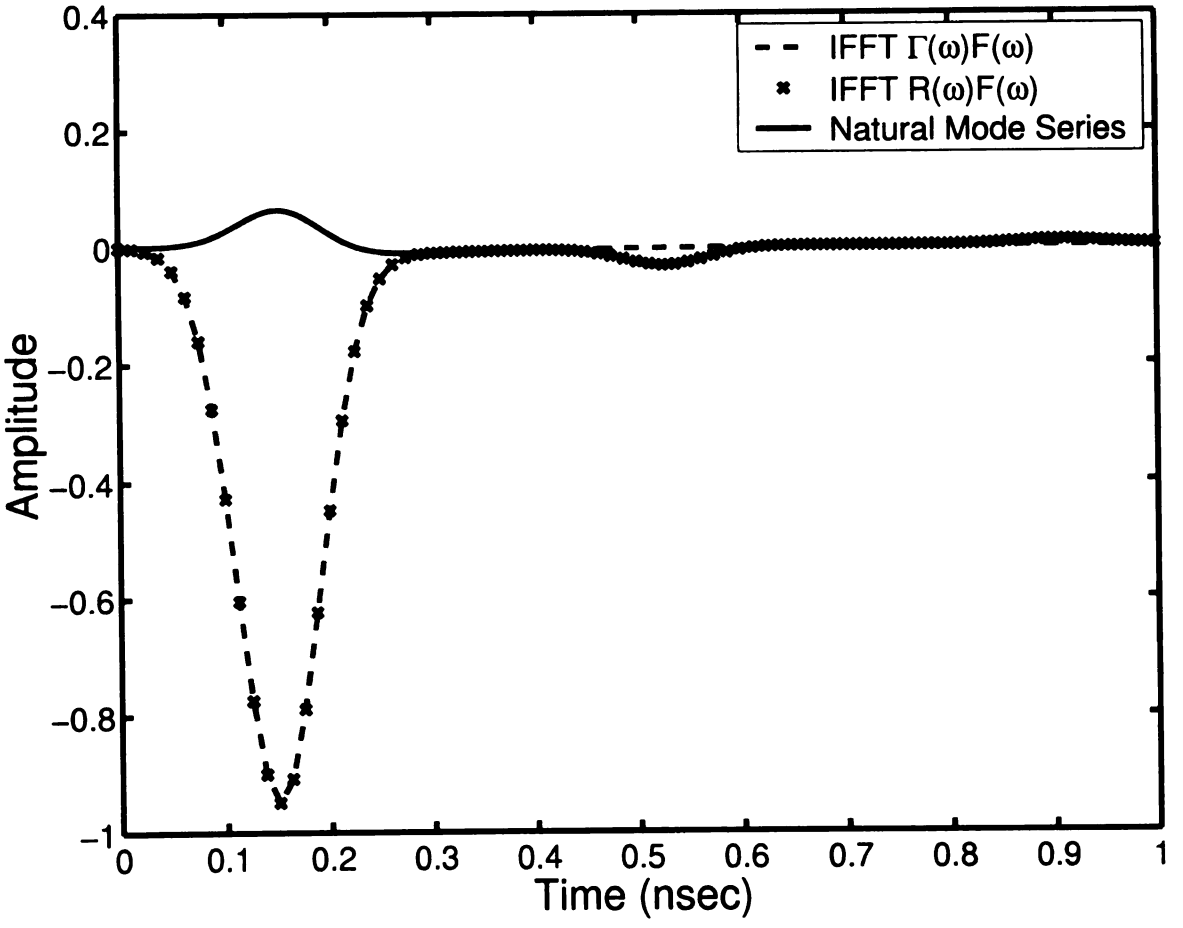

Figure 3.25: Time domain response, $\perp$ polarization ($\epsilon_r = 9$, $\Delta = 2$ cm, $\theta_i = 85°$, $\sigma = 0.5$ S/m).

Chapter 4: Natural Mode Analysis of an Air-Backed Slab

In the previous chapter, the transient response from the conductor backed slab has been discussed. For the air backed slab case, most of the previous developments can be used with a few modifications. The main difference from the previous case is that the reflection coefficient has the different form due to its different backing material. For the detail of the following discussion, refer to the conductor-backed case in the previous chapter. However, in some parts, the discussion will be repeated in order to clarify the developments.

4.1 Formulation of the frequency-domain reflection

Consider a plane wave of frequency ω incident from free space onto an interface between free space and an air backed slab of material with frequency independent material parameters $\epsilon = \epsilon_r\epsilon_0$, μ_0, and σ, and with thickness Δ, as shown in Figure 4.1. In the figure, region 0 and region 1 correspond to free space and the dielectric slab respectively. Likewise, for the subsequent discussion, the subscripts 0 and 1 correspond to free space and dielectric, respectively. As shown in (2.41), (3.3) and (3.4), the reflection coefficients have the general form

$$R(\omega) = \frac{\Gamma(\omega)[1 - e^{-j\omega\tau(\omega)}]}{1 - \Gamma^2(\omega)e^{-j\omega\tau(\omega)}} \tag{4.1}$$

where $\Gamma(\omega)$ is the interfacial reflection coefficient, given in general form by

$$\Gamma(\omega) = \frac{Z_1(\omega) - Z_0}{Z_1(\omega) + Z_0},$$

and

$$\tau(\omega) = \frac{2\Delta}{c} F(\omega), \quad F(\omega) = \sqrt{\bar{\epsilon} + \frac{\sigma}{j\omega\epsilon_0}}.$$

Since $R(\omega)$ exists, its Laplace domain representation also exists [21], and is given by

$$R(s) = R(\omega)|_{\omega=s/j} = \frac{\Gamma(s)[1 - e^{-s\tau(s)}]}{1 - \Gamma^2(s)e^{-s\tau(s)}}, \tag{4.2}$$

where

$$s\tau(s) = \frac{2\Delta}{\nu}\sqrt{s}\sqrt{s - s_0}, \tag{4.3}$$

$$\Gamma(s) = \frac{Z_1(s) - Z_0}{Z_1(s) + Z_0}, \tag{4.4}$$

as shown in (3.7) and (3.8). Here $\nu = c/\sqrt{\bar{\epsilon}}$ and $s_0 = -\sigma/(\epsilon_0\bar{\epsilon})$.

For perpendicular polarization the z-directed impedance $Z_1(s)$ is

$$\begin{aligned} Z_\perp(s) &= \left.\frac{\eta_0}{F(\omega)}\right|_{\omega=s/j} = \frac{\eta_0}{\sqrt{\bar{\epsilon} + \frac{\sigma}{s\epsilon_0}}} \\ &= \frac{\eta_0 s}{\sqrt{\bar{\epsilon}}\sqrt{s}\sqrt{s - s_0}}, \end{aligned} \tag{4.5}$$

and for parallel polarization

$$\begin{aligned} Z_\parallel(s) &= \left.\frac{\eta_0 F(\omega)}{\epsilon_r + \frac{\sigma}{j\omega\epsilon_0}}\right|_{\omega=s/j} = \frac{\eta_0\sqrt{\bar{\epsilon} + \frac{\sigma}{s\epsilon_0}}}{\epsilon_r + \frac{\sigma}{s\epsilon_0}} \\ &= \frac{\eta_0\sqrt{\bar{\epsilon}}\sqrt{s}\sqrt{s - s_0}}{s\epsilon_r + \frac{\sigma}{\epsilon_0}}. \end{aligned} \tag{4.6}$$

Therefore, the interfacial reflection coefficient $\Gamma(s)$ in (4.4) can be written as

$$\Gamma(s) = \begin{cases} \dfrac{s\cos\theta_i - \sqrt{\bar{\epsilon}}\sqrt{s}\sqrt{s-s_0}}{s\cos\theta_i + \sqrt{\bar{\epsilon}}\sqrt{s}\sqrt{s-s_0}}. & (\perp \text{ pol.}) \\ \dfrac{\sqrt{\bar{\epsilon}}\sqrt{s}\sqrt{s-s_0} - \cos\theta_i(s\epsilon_r + \frac{\sigma}{\epsilon_0})}{\sqrt{\bar{\epsilon}}\sqrt{s}\sqrt{s-s_0} + \cos\theta_i(s\epsilon_r + \frac{\sigma}{\epsilon_0})}. & (\| \text{ pol.}) \end{cases} \tag{4.7}$$

The reflection coefficient $R(s)$ is the transfer function of the system. Thus, the impulse response $r(t)$ is obtained by

$$r(t) = \mathcal{L}^{-1}\{R(s)\} = \frac{1}{j2\pi}\int_{Br} R(s)e^{st}\mathrm{d}s \tag{4.8}$$

where Br indicates the Bromwich path. This integral can be evaluated by contour integration. We must thus examine the singularities and define an appropriate branch for the integrand.

4.2 Singularities and the branch cut

From the complex square roots in $s\tau(s)$ and $Z_1(s)$, the branch points are located at $s = 0$ and $s = s_0$. In order to ensure the continuity of $R(s)$, the branch cut is taken along the negative real axis between the two branch points.

From (4.2), the poles are the roots of

$$1 - \Gamma^2(s)e^{-s\tau(s)} = 0. \tag{4.9}$$

Taking the logarithm of this equation and rearranging gives

$$\ln\left[\Gamma^2(s)e^{-s\tau(s)}\right] = \ln\left|\Gamma^2(s)e^{-s\tau(s)}\right| + j\arg\left[\Gamma^2(s)e^{-s\tau(s)}\right] \pm j2n\pi = 0, \quad (n = 0, 1, 2, \cdots).$$

Since $-\pi < \arg\left[\Gamma^2(s)e^{-s\tau(s)}\right] < \pi$ and the goal is to find roots, n can be set to 0.

Therefore, the poles should satisfy

$$\ln\left|\Gamma^2(s)e^{-s\tau(s)}\right| + j\arg\left[\Gamma^2(s)e^{-s\tau(s)}\right] = 0. \tag{4.10}$$

Except for the lossless case ($\sigma = 0$), wherein the poles can be calculated analytically, the above equation needs to be solved numerically. For the lossless case, both $\Gamma(s)$ and $\tau(s)$ are independent of s, and $-1 < \Gamma < 0$, i.e. $\arg(\Gamma) = \pi$. As a result, from (4.10), the lossless case poles are

$$s = \frac{2}{\tau}\left[\ln|\Gamma| \pm jn\pi\right], \quad n = 0, 1, 2, 3, \cdots \tag{4.11}$$

Note that, unlike the conductor-backed case, (4.11) has a real pole even for the lossless case. From (4.10) and (4.11), it is clear that the poles occur in complex conjugate pairs as expected for real signals. Table 4.1 shows the lossless case poles, where $\theta_i = 0°$, $\epsilon_r = 9$ and $\Delta = 2$ cm. In the table, only poles in the upper-half complex plane including the real axis are shown.

When the conductivity is nonzero, equation (4.10) can be solved by 2-D root search algorithms such as the Newton-Rahpson method [17] using the lossless case poles as the initial guesses. Again, it should be emphasized that the real part of a pole should be less than or equal to zero for a passive system. This can be shown to be true by noting that the magnitude of $\Gamma^2(s)e^{-s\tau(s)}$ in (4.10) is always less than 1 if $\mathrm{Re}\{s\}$ is greater than zero, since both the magnitudes of $\Gamma(s)$ and $e^{-s\tau(s)}$ are less than 1 as can be shown using (4.3) and (4.7). Here, it should be remembered that $s_0 = -\sigma/(\epsilon_0\bar{\epsilon})$ is a non-positive constant. As a result, no solution of (4.10) can exist if $\mathrm{Re}\{s\}$ is positive.

Figure 4.2 and Figure 4.3 show several pole trajectories obtained by the Newton-Rahpson method when the conductivity σ varies from 0 to 10 S/m for perpendicular and parallel polarization respectively. Here, only the complex poles

are shown and the mode number 0 is assigned to the pole with the smallest imaginary part and the mode number 1 for the next smallest, and so on. Similar to the conductor-backed case, when the conductivity reaches a certain value, each pole becomes purely real. In the figures, the conductivity values at which the poles become real are shown, and the corresponding pole locations in the complex s plane are shown as the cross-marks. As shown in the figures, when the conductivity increases, the magnitudes of the imaginary parts of the poles decrease whereas those of the real parts increase until the poles approach the real axis and become purely real. This phenomenon is clearly seen in Figure 4.4 and Figure 4.5. Note the difference between the mode 0 pole trajectories of the perpendicular and parallel polarization cases.

These pole trajectories of both polarizations suggest that when the conductivity becomes higher, the amplitude decay factors become larger, resulting in a smaller contribution to the late-time response.

In Figure 4.6 and Figure 4.7, the pole trajectories for varying angle of incidence are shown, where $\epsilon_r = 9$ and $\sigma = 1.0$ S/m. As seen in Figure 4.6, which depicts the pole amplitudes of the perpendicular polarization case, as the angle of incidence increases, the magnitudes of the real parts of the poles monotonically decrease whereas those of the imaginary parts are relatively unchanged. Again, it should be emphasized that the pole locations do not solely determine the late-time transient responses. In order to obtain the correct transient responses, the residues corresponding to the poles should be considered. For the parallel polarization case, as the angle of incidence increases, the magnitudes of the real parts of the poles show a dip around 70° of incidence angle which approximately corresponds to the Brewster angle calculated as [15]

$$\theta_{B\|} = \sin^{-1}\sqrt{\frac{\epsilon_2}{\epsilon_1+\epsilon_2}} = \sin^{-1}\sqrt{\frac{9}{1+9}} = 71.6°,$$

where we assume the dielectric material is lossless and $\epsilon_r = 9$. Similar to the conductor-backed case, for the air-backed case, the mode 0 pole also becomes real approximately at this angle. However, unlike the conductor-backed case where the mode 0 pole remained real beyond this incidence angle, it becomes complex pole again (in this case, it becomes real at 68° and becomes complex again at 72° of incidence angle), and it follows the trajectory of the bottom arc of the higher mode (mode 1) as shown in the top figure of Figure 4.7. The other modes also show the similar behavior, i.e. at a certain angle of incidence, they follow the bottom arc of the trajectories of the next higher modes. It seems that this particular behavior is due to the periodic nature of the arguments of the complex numbers. The behavior of the parallel polarization case evidently suggests that the late-time response may be affected by the Brewster angle. The existence condition for the real poles and the algorithm for finding such poles are examined next.

Let us assume a complex frequency s to be negative real and denote its magnitude as x, where $x > 0$. Then, if $s > s_0$, i.e., $\sigma > -s\epsilon_0\bar{\epsilon}$, from (3.7) and (3.11)

$$s\tau(s) = j\frac{2\Delta}{\nu}\sqrt{x}\sqrt{-(x+s_0)}, \tag{4.12}$$

and the reflection coefficient becomes

$$\Gamma(s) = \begin{cases} \dfrac{-x\cos\theta_i - j\sqrt{\bar{\epsilon}}\sqrt{x}\sqrt{-(x+s_0)}}{-x\cos\theta_i + j\sqrt{\bar{\epsilon}}\sqrt{x}\sqrt{-(x+s_0)}}. & (\perp \text{ pol.}) \\ \dfrac{j\sqrt{\bar{\epsilon}}\sqrt{x}\sqrt{-(x+s_0)} - \cos\theta_i(-x\epsilon_r + \frac{\sigma}{\epsilon_0})}{j\sqrt{\bar{\epsilon}}\sqrt{x}\sqrt{-(x+s_0)} + \cos\theta_i(-x\epsilon_r + \frac{\sigma}{\epsilon_0})}. & (\parallel \text{ pol.}) \end{cases} \tag{4.13}$$

It is now clear that the magnitudes of both $e^{-s\tau(s)}$ and $\Gamma(s)$ are 1. As a result, $\ln\left|\Gamma(s)^2 e^{-s\tau(s)}\right| = 0$, and the poles need to satisfy only the imaginary part of (4.10), i.e., $\arg\left[\Gamma(s)^2 e^{-s\tau(s)}\right] = 0$. Therefore, if we denote $-(2\Delta/\nu)\sqrt{x}\sqrt{-(x+s_0)}$, which

is $-s\tau(s)$, as ϕ_1 and $\arg[\Gamma^2(s)]$ as ϕ_2, the poles need to satisfy

$$\phi_1 + \phi_2 + 2n\pi = 0. \quad n = 0, 1, 2, \cdots \tag{4.14}$$

Here, only the positive sign in front of n is necessary, since ϕ_1 is always negative, when $s > s_0$ and $-\pi < \phi_2 < \pi$. The above equation, which we call the *characteristic function*, can be solved by any 1-D root search algorithm, such as the secant method. Here, it is very important to note that (4.14) does not always have solutions, and that the number of solutions is dependent upon the conductivity, permittivity and incident angle. In addition, great care should be taken when finding the real roots, especially for the $n = 0$ case where the characteristic function can have more than one root, which may cause the usual secant method to fail.

If $s < s_0$, $s\tau(s)$ becomes negative real causing $e^{-s\tau(s)}$ to be greater than 1, and $\Gamma(s)$ becomes real. Therefore, in (4.10), $\arg\left[\Gamma(s)^2 e^{-s\tau(s)}\right] = 0$. As a result, the poles only need to satisfy $2\ln|\Gamma(s)| - s\tau(s) = 0$. Figure 4.8 shows the amplitudes of the reflection coefficients for both polarizations, where $s < s_0$. As shown in the figure, for perpendicular polarization, the reflection coefficient $\Gamma(s) = 1$ when $s = s_0$ and monotonically decreases as s decreases. In particular, it becomes negative when $s < \frac{\sigma}{\epsilon_0(1-\epsilon_r)}$, since the reflection coefficient has roots

$$s = 0, \quad \frac{\sigma}{\epsilon_0(1-\epsilon_r)}.$$

As a result, two additional real pole can exist when $s < s_0$ for perpendicular polarization. Figure 4.9 shows the amplitudes of $-s\tau(s)$, $\ln|\Gamma(s)|$ and $2\ln|\Gamma(s)| - s\tau(s)$ for perpendicular polarization. In the figure, the points where $2\ln|\Gamma(s)| - s\tau(s)$ cross the 0 amplitude line represent the pole locations (there are 2). It should be noted that the apparent pole $s = s_0$ where both $e^{-s\tau(s)}$ and $\Gamma^2(s)$ are 1 is a removable pole, since the numerator of the reflection coefficient becomes

identical to the denominator.

For parallel polarization, $\Gamma(s) = -1$ when $s = s_0$, and it has two real roots at

$$s = \frac{\sigma}{\epsilon_0(1-\epsilon_r)}, \quad \frac{\sigma}{\epsilon_0(\tan^2\theta_i - \epsilon_r)}.$$

Therefore, depending on ϵ_r and θ_i, the amplitude of the reflection coefficient increases initially, then stays positive or monotonically decreases as s decreases. As a result, at most 4 real poles can exist when $s < s_0$ for parallel polarization. Figure 4.10 shows the case where 3 real poles exist.

A complete sketch of the poles is shown in Figure 4.11 and Figure 4.12. In the figures, the solid lines represent the trajectories of the complex poles, and the cross-marks represent the real poles. The real poles consist of the poles with magnitudes less than s_0 and those with magnitudes greater than s_0. Since the complex pole trajectories from different modes follow approximately the same curve in the complex s plane (before each mode becomes real and diverges), it is difficult to resolve each complex pole trajectory from the figures. As previously discussed, the complex poles gradually become real poles as the conductivity increases. Note that, except for mode 0, each single complex pole splits into a pair of real poles.

4.3 Evaluation of $r(t)$

Since all poles and branch points lie in the left half plane including the imaginary axis, the region of convergence is the right half plane. Therefore, the Bromwich path is put in the right half plane and the Laplace inversion integral is evaluated by contour integration. The evaluation is accomplished in two different time intervals, corresponding to the early-time period and the late-time period. The beginning of the late-time period is $\tau_0 = \frac{2\Delta}{\nu}$, which represents the two-way transit time of the wave inside the dielectric slab.

4.3.1 Case I: $t > \tau_0$

When $t > \tau_0$, the integration contour is closed in the left half plane as shown in Figure 4.13. Inside the contour, the branch cut lies from 0 to s_0 and there is a closed path enclosing the branch cut and several possible real poles on the branch cut (two of which are shown). We denote the outer integration contour which includes the Bromwich path as C_0 and the closed path which encloses the branch cut as C_1, such that

$$\begin{aligned} C_0 &= B_r + \Gamma_\infty + L_1 + L_2, \\ C_1 &= \gamma_1 + \gamma_2 + \cdots + \gamma_6 + l_1 + l_2 + \cdots + l_6. \end{aligned}$$

Then, by Cauchy's residue theorem,

$$\int_{C_0+C_1} R(s)e^{st}\,\mathrm{d}s = j2\pi \sum Res[R(s)e^{st}, poles] \tag{4.15}$$

Therefore, if the integral contribution from each path is known, the impulse response $r(t)$ can be determined.

The contribution from Γ_∞

On Γ_∞, from (4.3),

$$\begin{aligned} \mathrm{Re}\{\tau(s)\} &= \mathrm{Re}\left\{ \lim_{\mathrm{Re}\{s\}\to-\infty} \frac{2\Delta}{\nu}\sqrt{1+\frac{\sigma}{s\epsilon_0\bar{\epsilon}}} \right\} \\ &\simeq \frac{2\Delta}{\nu} = \tau_0 \end{aligned}$$

If we let $t_1 = t - \tau_0$, which is positive since we are evaluating the integral when $t > \tau_0$, then

$$\int_{\Gamma_\infty} R(s)e^{st}\,\mathrm{d}s = \int_{\Gamma_\infty} \frac{\Gamma(s)e^{s\tau_0} - \Gamma(s)e^{s\tau_0}e^{-s\tau(s)}}{1 - \Gamma^2(s)e^{-s\tau(s)}} e^{st_1}\,\mathrm{d}s = \int_{\Gamma_\infty} f(s)e^{st_1}\,\mathrm{d}s$$

Since $f(s) \to 0$ on Γ_∞, by *Jordan's Lemma* [20], [21],

$$\int_{\Gamma_\infty} R(s)e^{st}\,\mathrm{d}s = 0 \tag{4.16}$$

The contribution from L_1 and L_2

As seen in the conductor backed case, for L_1 and L_2, the same theorem [14] can be used to apply *Jordan's Lemma.* As a result, it can be shown that

$$\int_{L_1,L_2} R(s)e^{st}\,\mathrm{d}s = 0 \tag{4.17}$$

The contribution from C_1

The segments of the contour C_1 enclosing the branch cut can be divided into three groups as did in the conductor backed case. The first group consists of γ_1 and γ_4 that enclose the branch points s_0 and 0 respectively. The second group consists of the straight lines immediately below and above the branch cut, and those are designated $l_1, l_2, \cdots, l_6$. The last group consists of γ_2, γ_3, γ_5 and γ_6 that enclose the real poles on the branch cut. These groups will be examined separately.

Denote the radius of γ_1 as r, and let θ to be the angle measured counterclockwise from the real axis to the point on γ_1. Then, any point on γ_1 can be represented as

$$s = s_0 + re^{j\theta}.$$

The reflection coefficient on γ_1 with $r \to 0$, i.e. $s \to s_0$, becomes

$$\Gamma(s) = \begin{cases} \dfrac{s\eta_0 - Z_{0\perp}\sqrt{\bar{\epsilon}}\sqrt{s}\sqrt{s-s_0}}{s\eta_0 + Z_{0\perp}\sqrt{\bar{\epsilon}}\sqrt{s}\sqrt{s-s_0}} & \longrightarrow \quad 1, \quad \perp \text{ - pol} \\ \dfrac{\eta_0\sqrt{\bar{\epsilon}}\sqrt{s}\sqrt{s-s_0} - Z_{0\|}(s\epsilon_r + \frac{\sigma}{\epsilon_0})}{\eta_0\sqrt{\bar{\epsilon}}\sqrt{s}\sqrt{s-s_0} + Z_{0\|}(s\epsilon_r + \frac{\sigma}{\epsilon_0})} & \longrightarrow -1, \quad \| \text{ - pol} \end{cases} \tag{4.18}$$

Then,

$$R(s)e^{st} = \frac{\Gamma(s)[1 - e^{-s\tau(s)}]}{1 - \Gamma^2(s)e^{-s\tau(s)}}e^{st} = \begin{cases} e^{st} & , \quad \perp \text{ - pol} \\ -e^{st} & , \quad \| \text{ - pol} \end{cases}$$

and

$$\left|R(s)e^{st}\right| \leq e^{(s_0+r)t}.$$

Therefore,

$$\left|\int_{\gamma_1} R(s)e^{st}\,\mathrm{d}s\right| \leq 2\pi\, r\, e^{(s_0+r)t} \to 0, \quad (r \to 0).$$

As a result,

$$\int_{\gamma_1} R(s)e^{st}\,\mathrm{d}s = 0. \tag{4.19}$$

Similarly, it can be shown

$$\int_{\gamma_4} R(s)e^{st}\,\mathrm{d}s = 0. \tag{4.20}$$

For the second group, it is necessary to determine $\Gamma(s)$ and $s\tau(s)$ along a path immediately above the branch cut, which we denote as B^+, and immediately below the branch cut, which we denote as B^-. If we denote the magnitude of s as x $(s_0 + r < -x < -r < 0)$, then on B^+,

$$\sqrt{s}\sqrt{s-s_0} = j\sqrt{x}\sqrt{-x-s_0}\,,$$

and on B^-,

$$\sqrt{s}\sqrt{s-s_0} = -j\sqrt{x}\sqrt{-x-s_0}\,.$$

Now, let $Z(s)$ on B^+ be denoted as Z^+, and Z(s) on B^- as Z^-. Then, using (4.7), it can be shown that

$$Z^+ = -Z^-. \tag{4.21}$$

Since,

$$\begin{aligned} R(s) &= \frac{\Gamma^2(s)[1-e^{-s\tau(s)}]}{1-\Gamma^2(s)e^{-s\tau(s)}} \\ &= \frac{[Z^2(s)-Z_0^2]e^{\frac{1}{2}s\tau(s)}-[Z^2(s)+Z_0^2]e^{-\frac{1}{2}s\tau(s)}}{[Z(s)+Z_0]^2e^{\frac{1}{2}s\tau(s)}-[Z(s)-Z_0]^2e^{-\frac{1}{2}s\tau(s)}}, \end{aligned}$$

we have,

$$\begin{aligned} R(s)|_{B^+} &= \frac{[Z^{2+}-Z_0^2]e^{j\phi}-[Z^{2+}+Z_0^2]e^{-j\phi}}{[Z^+ + Z_0]^2e^{j\phi}-[Z^+-Z_0]^2e^{-j\phi}} \\ &= \frac{2j[Z^{2+}-Z_0^2]\sin\phi}{2j[Z^{2+}+Z_0^2]\sin\phi+2Z^+Z_0\cos\phi} \end{aligned}$$

where $j\phi = \frac{1}{2}s\tau(s)$, and

$$\begin{aligned} R(s)|_{B^-} &= \frac{[Z^{2-}-Z_0^2]e^{-j\phi}-[Z^{2-}+Z_0^2]e^{j\phi}}{[Z^- + Z_0]^2e^{-j\phi}-[Z^--Z_0]^2e^{j\phi}} \\ &= \frac{-2j[Z^{2-}-Z_0^2]\sin\phi}{-2j[Z^{2-}+Z_0^2]\sin\phi+2Z^-Z_0\cos\phi} \end{aligned}$$

Therefore, by (4.21)

$$R(s)|_{B^+} = R(s)|_{B^-}.$$

As a result,

$$\int_{l_1+l_2+l_3} R(s)|_{B^+}e^{st}\,ds + \int_{l_4+l_5+l_6} R(s)|_{B^-}e^{st}\,ds = 0 \tag{4.22}$$

The integral contributions from the third group and the other complex poles can be determined by calculating the residues of $R(s)^2e^{st}$ at the poles. It is found

that all of the poles of $R(s)$ are of first order and thus

$$Res\left[R(s)^2 e^{st},\, poles\right]|_{s=s_k} = \lim_{s\to s_k}(s-s_k)\left[\frac{\Gamma(s)[1-e^{-s\tau(s)}]}{1-\Gamma^2(s)e^{-s\tau(s)}}e^{st}\right] = A_k e^{s_k t}, \quad (4.23)$$

where

$$A_k = -\frac{\Gamma(s_k)[1-e^{-s_k\tau(s_k)}]}{\frac{d}{ds}\left[\Gamma^2(s)e^{-s\tau(s)}\right]|_{s=s_k}} \quad (4.24)$$

is the complex natural mode amplitude. Carrying out the details gives

$$A_k = \Gamma(s)e^{-\frac{2\Delta}{\nu}\sqrt{s}\sqrt{s-s_0}}\left[2G(s) - \frac{\Delta}{\nu}\Gamma(s)\frac{2s-s_0}{\sqrt{s}\sqrt{s-s_0}}\right], \quad (4.25)$$

where

$$G(s) = \frac{2\cos\theta_i\sqrt{\bar{\epsilon}}\sqrt{s}\sqrt{s-s_0} - \cos\theta_i\sqrt{\bar{\epsilon}}\frac{2s^2-ss_0}{\sqrt{s}\sqrt{s-s_0}}}{s^2\cos^2\theta_i + 2s\sqrt{\bar{\epsilon}}\sqrt{s}\sqrt{s-s_0} + \bar{\epsilon}s(s-s_0)},$$

for perpendicular polarization and

$$G(s) = \frac{\cos\theta_i(s\epsilon_r + \frac{\sigma}{\epsilon_0})\sqrt{\bar{\epsilon}}\frac{2s-s_0}{\sqrt{s}\sqrt{s-s_0}} - 2\epsilon_r\cos\theta_i\sqrt{\bar{\epsilon}}\sqrt{s}\sqrt{s-s_0}}{\bar{\epsilon}s(s-s_0) + 2\cos\theta_i(s\epsilon_r + \frac{\sigma}{\epsilon_0})\sqrt{\bar{\epsilon}}\sqrt{s}\sqrt{s-s_0} + \cos^2\theta_i(s\epsilon_r + \frac{\sigma}{\epsilon_0})^2}$$

for parallel polarization.

Collecting the results from (4.16)-(4.25), the impulse response $r(t)$ becomes

$$r(t) = \frac{1}{j2\pi}\int_{B_r} R(s)e^{st}\,ds = \sum A_k e^{s_k t}, \quad t > \tau_0\,, \quad (4.26)$$

and thus the late-time period is a pure natural resonance series, and contains no branch-cut contribution.

4.3.2 Case II: $t < \tau_0$

For $t < \tau_0$, $r(t)$ is found by computing the inverse Laplace transform of $R(s) = \Gamma(s) + \overline{R}(s)$, where

$$\overline{R}(s) = R(s) - \Gamma(s) = \left[\Gamma^2(s) - 1\right] \frac{\Gamma(s)e^{-s\tau(s)}}{1 - \Gamma^2(s)e^{-s\tau(s)}}.$$

Then

$$\overline{R}(t) = \mathcal{L}^{-1}\left\{\overline{R}(s)\right\} = \frac{1}{j2\pi} \int_{Br} \left[\Gamma^2(s) - 1\right] \frac{\Gamma(s)e^{-s\tau(s)}}{1 - \Gamma^2(s)e^{-s\tau(s)}} e^{st} ds.$$

To compute this integral, the integration contour is closed in the right half plane, as shown in Figure 4.14. On Γ_∞, from (4.3),

$$\begin{aligned} \mathrm{Re}\left\{\tau(s)\right\} &= \mathrm{Re}\left\{\lim_{\mathrm{Re}\{s\}\to\infty} \frac{2\Delta}{\nu}\sqrt{1 + \frac{\sigma}{s\epsilon_0\bar{\epsilon}}}\right\} \\ &\simeq \frac{2\Delta}{\nu} = \tau_0 \end{aligned}$$

If we let $t_1 = t - \tau_0$, which is negative since we are evaluating the integral when $t < \tau_0$, then

$$\int_{\Gamma_\infty} \overline{R}(s)e^{st}\,\mathrm{d}s = \int_{\Gamma_\infty} \left[\Gamma^2(s) - 1\right] \frac{\Gamma(s)e^{-s\tau(s)}e^{s\tau_0}}{1 - \Gamma^2(s)e^{-s\tau(s)}} e^{st_1}\,\mathrm{d}s = \int_{\Gamma_\infty} f(s)e^{st_1}\,\mathrm{d}s$$

Here, it is not possible to apply *Jordan's Lemma* directly, since $f(s)$ does not approach zero over the entire contour Γ_∞. However, if we use the theorem introduced earlier, it can be argued that

$$\int_{\Gamma_\infty} \overline{R}(s)e^{st}\,\mathrm{d}s = 0$$

The inverse transform of $\Gamma(s)$, denoted as $\Gamma(t)$, can be found in [26] and [27]. As a result, when $t < \tau_0$, $r(t)$ becomes

$$r(t) = \Gamma(t), \quad t < \tau_0. \tag{4.27}$$

Combining the results (4.26) and (4.27), the impulse response $r(t)$ is

$$r(t) = \begin{cases} \sum A_k e^{s_k t}, & t > \tau_0 \\ \Gamma(t), & t < \tau_0. \end{cases} \tag{4.28}$$

4.4 Results

As with the conductor-backed case, it has been shown analytically that the early-time response is a specular reflection from the interface between free-space and the dielectric slab, and the late-time response is a pure sum of damped sinusoids. In order to verify these results, the natural mode series is compared to the direct IFFT using a truncated Gaussian pulse as the input waveform. This waveform, which is identical to the conductor-backed case, is shown in the inset of Figure 4.15. Figures 4.15-4.21 show the transient responses calculated by the natural mode series and the IFFT. In addition, the IFFT of the interfacial reflection coefficients $\Gamma(s)$ are also shown in order to explain the early-time behavior. The natural resonant frequencies of the corresponding cases are shown in Table 4.1-4.7.

As an example of the results, in Figure 4.17 the incident wave is in perpendicular polarization with an incidence angle of 20°, and the material parameters are $\Delta = 2$ cm, $\epsilon_r = 9$ and $\sigma = 0.1$ S/m. Therefore, the beginning of the impulse response late-time, i.e., the two-way transit time of the wave inside the slab, is $\tau_0 = 0.397$ ns. As shown in Figure 4.17, during the early-time period, before τ_0, the IFFT of $R(\omega)F(\omega)$ (where $F(\omega)$ is the spectrum of the input waveform)

matches well with the IFFT of $\Gamma(\omega)F(\omega)$, which is the specular reflection from the interface. During the late-time, the IFFT of $R(\omega)F(\omega)$ matches well with the natural mode series. Again, it should be noted that when $t < \tau_0$ the response from the natural mode series does not have any meaning; i.e., the natural mode series is valid only when $t > \tau_0$, the late-time period. Since the frequency band of the input waveform is roughly $0 - 20$ GHz, it was found that the first 7 natural modes, which are shown in Table 4.17, are sufficient to represent the late-time reflected field.

Figure 4.15 shows the response from the lossless, normal incidence case. As seen in the figure, there are equally spaced replicas of the input waveform with gradually diminishing amplitudes during the late-time period.

Comparing Figures 4.18 and 4.19 to Figures 4.16 and 4.17, due to the relatively higher conductivity in the Figure 4.18 and 4.19 cases, relatively smaller late-time responses are observed. The corresponding natural resonance frequencies for these cases are shown in Tables 4.4 and 4.5.

The responses from both polarizations with the incidence angle $\theta_i = 70°$, which is close to the lossless case Brewster angle, are shown in Figures 4.20 and 4.21. As seen in Figure 4.20, there is neither interfacial reflection nor the late-time response for the parallel polarization case whereas both the interfacial reflection and the late-time response are observed for the perpendicular polarization case, as shown in Figure 4.21.

Table 4.1: Poles and corresponding complex natural mode amplitudes (A_k), loseless case ($\epsilon_r = 9$, $\Delta = 2$ cm, $\theta_i = 0°$)

	Pole Amplitude		Natural Mode Amplitude	
	Real Part	Imaginary Part	Real Part	Imaginary Part
mode 0	$-.34657 \times 10^{10}$	$.15708 \times 10^{11}$	$.37500 \times 10^{10}$	$.14164 \times 10^{-5}$
mode 1	$-.34657 \times 10^{10}$	$.31416 \times 10^{11}$	$.37500 \times 10^{10}$	$.28327 \times 10^{-5}$
mode 2	$-.34657 \times 10^{10}$	$.47124 \times 10^{11}$	$.37500 \times 10^{10}$	$.53593 \times 10^{-5}$
mode 3	$-.34657 \times 10^{10}$	$.62832 \times 10^{11}$	$.37500 \times 10^{10}$	$.56655 \times 10^{-5}$
mode 4	$-.34657 \times 10^{10}$	$.78540 \times 10^{11}$	$.37500 \times 10^{10}$	$.59717 \times 10^{-5}$
mode 5	$-.34657 \times 10^{10}$	$.94248 \times 10^{11}$	$.37500 \times 10^{10}$	$.10719 \times 10^{-4}$
mode 6	$-.34657 \times 10^{10}$	$.10996 \times 10^{12}$	$.37500 \times 10^{10}$	$.21431 \times 10^{-5}$
real	$-.34657 \times 10^{10}$	0.0	$.37500 \times 10^{10}$	0.0

Table 4.2: Poles and corresponding complex natural mode amplitudes (A_k), $\|$ polarization ($\epsilon_r = 9$, $\Delta = 2$ cm, $\theta_i = 20°$, $\sigma = 0.5$ S/m)

	Pole Amplitude		Natural Mode Amplitude	
	Real Part	Imaginary Part	Real Part	Imaginary Part
mode 0	$-.70815 \times 10^{10}$	$.14659 \times 10^{11}$	$.44840 \times 10^{10}$	$.10437 \times 10^{10}$
mode 1	$-.69320 \times 10^{10}$	$.31060 \times 10^{11}$	$.41426 \times 10^{10}$	$.51448 \times 10^{9}$
mode 2	$-.69078 \times 10^{10}$	$.47060 \times 10^{11}$	$.40902 \times 10^{10}$	$.34128 \times 10^{9}$
mode 3	$-.68995 \times 10^{10}$	$.62965 \times 10^{11}$	$.40725 \times 10^{10}$	$.25549 \times 10^{9}$
mode 4	$-.68957 \times 10^{10}$	$.78832 \times 10^{11}$	$.40644 \times 10^{10}$	$.20421 \times 10^{9}$
mode 5	$-.68937 \times 10^{10}$	$.94680 \times 10^{11}$	$.40601 \times 10^{10}$	$.17009 \times 10^{9}$
mode 6	$-.68925 \times 10^{10}$	$.11052 \times 10^{12}$	$.40575 \times 10^{10}$	$.14575 \times 10^{9}$
real	$-.10290 \times 10^{11}$	0.0	$.47555 \times 10^{10}$	0.0

Table 4.3: Poles and corresponding complex natural mode amplitudes (A_k), $\perp$ polarization ($\epsilon_r = 9$, $\Delta = 2$ cm, $\theta_i = 20°$, $\sigma = 0.1$ S/m)

	Pole Amplitude		Natural Mode Amplitude	
	Real Part	Imaginary Part	Real Part	Imaginary Part
mode 0	$-.39505 \times 10^{10}$	$.15660 \times 10^{11}$	$.35867 \times 10^{10}$	$.15824 \times 10^{9}$
mode 1	$-.39292 \times 10^{10}$	$.31545 \times 10^{11}$	$.35399 \times 10^{10}$	$.84744 \times 10^{8}$
mode 2	$-.39252 \times 10^{10}$	$.47382 \times 10^{11}$	$.35310 \times 10^{10}$	$.57184 \times 10^{8}$
mode 3	$-.39239 \times 10^{10}$	$.63206 \times 10^{11}$	$.35279 \times 10^{10}$	$.43069 \times 10^{8}$
mode 4	$-.39232 \times 10^{10}$	$.79024 \times 10^{11}$	$.35264 \times 10^{10}$	$.34521 \times 10^{8}$
mode 5	$-.39229 \times 10^{10}$	$.94841 \times 10^{11}$	$.35256 \times 10^{10}$	$.28799 \times 10^{8}$
mode 6	$-.39226 \times 10^{10}$	$.11066 \times 10^{12}$	$.35252 \times 10^{10}$	$.24700 \times 10^{8}$
real	$-.46054 \times 10^{10}$	0.0	$.36268 \times 10^{10}$	0.0

Table 4.4: Poles and corresponding complex natural mode amplitudes (A_k), $\|$ polarization ($\epsilon_r = 9$, $\Delta = 2$ cm, $\theta_i = 30°$, $\sigma = 1.0$ S/m)

	Pole Amplitude		Natural Mode Amplitude	
	Real Part	Imaginary Part	Real Part	Imaginary Part
mode 0	$-.11099 \times 10^{11}$	$.30179 \times 10^{11}$	$.58349 \times 10^{10}$	$.16527 \times 10^{10}$
mode 1	$-.10616 \times 10^{11}$	$.30297 \times 10^{11}$	$.46827 \times 10^{10}$	$.12227 \times 10^{10}$
mode 2	$-.10557 \times 10^{11}$	$.40767 \times 10^{11}$	$.45729 \times 10^{10}$	$.78779 \times 10^{9}$
mode 3	$-.10538 \times 10^{11}$	$.62959 \times 10^{11}$	$.45384 \times 10^{10}$	$.58407 \times 10^{9}$
mode 4	$-.10529 \times 10^{11}$	$.79044 \times 10^{11}$	$.45231 \times 10^{10}$	$.46481 \times 10^{9}$
mode 5	$-.10525 \times 10^{11}$	$.95077 \times 10^{11}$	$.45149 \times 10^{10}$	$.38624 \times 10^{9}$
mode 6	$-.10522 \times 10^{11}$	$.11108 \times 10^{12}$	$.45100 \times 10^{10}$	$.33050 \times 10^{9}$
real	$-.17321 \times 10^{11}$	0.0	$.63125 \times 10^{10}$	0.0

Table 4.5: Poles and corresponding complex natural mode amplitudes (A_k), $\perp$ polarization ($\epsilon_r = 9$, $\Delta = 2$ cm, $\theta_i = 30°$, $\sigma = 1.5$ S/m).

	Pole Amplitude		Natural Mode Amplitude	
	Real Part	Imaginary Part	Real Part	Imaginary Part
mode 0	$-.13152 \times 10^{11}$	95409×10^{10}	$.41542 \times 10^{10}$	$.45363 \times 10^{10}$
mode 1	$-.12817 \times 10^{11}$	$.29278 \times 10^{11}$	$.33528 \times 10^{10}$	$.13039 \times 10^{10}$
mode 2	$-.12780 \times 10^{11}$	$.46117 \times 10^{11}$	$.32903 \times 10^{10}$	$.81773 \times 10^{9}$
mode 3	$-.12768 \times 10^{11}$	$.62478 \times 10^{11}$	$.32709 \times 10^{10}$	$.60124 \times 10^{9}$
mode 4	$-.12762 \times 10^{11}$	$.78662 \times 10^{11}$	$.32623 \times 10^{10}$	$.47670 \times 10^{9}$
mode 5	$-.12759 \times 10^{11}$	$.94760 \times 10^{11}$	$.32578 \times 10^{10}$	$.39535 \times 10^{9}$
mode 6	$-.12758 \times 10^{11}$	$.11081 \times 10^{12}$	$.32550 \times 10^{10}$	$.33790 \times 10^{9}$
real	$-.23152 \times 10^{11}$	0.0	$.49068 \times 10^{10}$	0.0

Table 4.6: Poles and corresponding complex natural mode amplitudes (A_k), $\|$ polarization ($\epsilon_r = 9$, $\Delta = 2$ cm, $\theta_i = 70°$, $\sigma = 0.5$ S/m)

	Pole Amplitude		Natural Mode Amplitude	
	Real Part	Imaginary Part	Real Part	Imaginary Part
mode 0	$-.55910 \times 10^{10}$	0.0	$-.11317 \times 10^{10}$	$-.65568 \times 10^{1}$
mode 1	$-.20677 \times 10^{11}$	$.26650 \times 10^{11}$	$.31069 \times 10^{11}$	$.77117 \times 10^{11}$
mode 2	$-.20636 \times 10^{11}$	$.45526 \times 10^{11}$	$.53730 \times 10^{11}$	$.50664 \times 10^{11}$
mode 3	$-.20624 \times 10^{11}$	$.63136 \times 10^{11}$	$.60330 \times 10^{11}$	$.37697 \times 10^{11}$
mode 4	$-.20619 \times 10^{11}$	$.80298 \times 10^{11}$	$.63188 \times 10^{11}$	$.30038 \times 10^{11}$
mode 5	$-.20616 \times 10^{11}$	$.97246 \times 10^{11}$	$.64693 \times 10^{11}$	$.24975 \times 10^{11}$
mode 6	$-.20614 \times 10^{11}$	$.11408 \times 10^{12}$	$.65584 \times 10^{11}$	$.21378 \times 10^{11}$
real	$-.37516 \times 10^{11}$	0.0	$.58574 \times 10^{12}$	0.0
	$-.21023 \times 10^{11}$	0.0	$-.15778 \times 10^{12}$	0.0
	$-.39937 \times 10^{11}$	0.0	$.41373 \times 10^{12}$	0.0

Table 4.7: Poles and corresponding complex natural mode amplitudes (A_k), $\perp$ polarization ($\epsilon_r = 9$, $\Delta = 2$ cm, $\theta_i = 70°$, $\sigma = 0.5$ S/m)

	Pole Amplitude		Natural Mode Amplitude	
	Real Part	Imaginary Part	Real Part	Imaginary Part
mode 0	$-.47744 \times 10^{10}$	$.15888 \times 10^{11}$	$.13251 \times 10^{10}$	$.29387 \times 10^{9}$
mode 1	$-.47586 \times 10^{10}$	$.32760 \times 10^{11}$	$.12925 \times 10^{10}$	$.14088 \times 10^{9}$
mode 2	$-.47558 \times 10^{10}$	$.49408 \times 10^{11}$	$.12869 \times 10^{10}$	$.93218 \times 10^{8}$
'mode 3	$-.47548 \times 10^{10}$	$.66002 \times 10^{11}$	$.12850 \times 10^{10}$	$.69733 \times 10^{8}$
mode 4	$-.47544 \times 10^{10}$	$.82574 \times 10^{11}$	$.12841 \times 10^{10}$	$.55719 \times 10^{8}$
mode 5	$-.47541 \times 10^{10}$	$.99136 \times 10^{11}$	$.12837 \times 10^{10}$	$.46403 \times 10^{8}$
mode 6	$-.47540 \times 10^{10}$	$.11569 \times 10^{12}$	$.12834 \times 10^{10}$	$.39758 \times 10^{8}$
real	$-.82716 \times 10^{10}$	0.0	$.13535 \times 10^{10}$	0.0

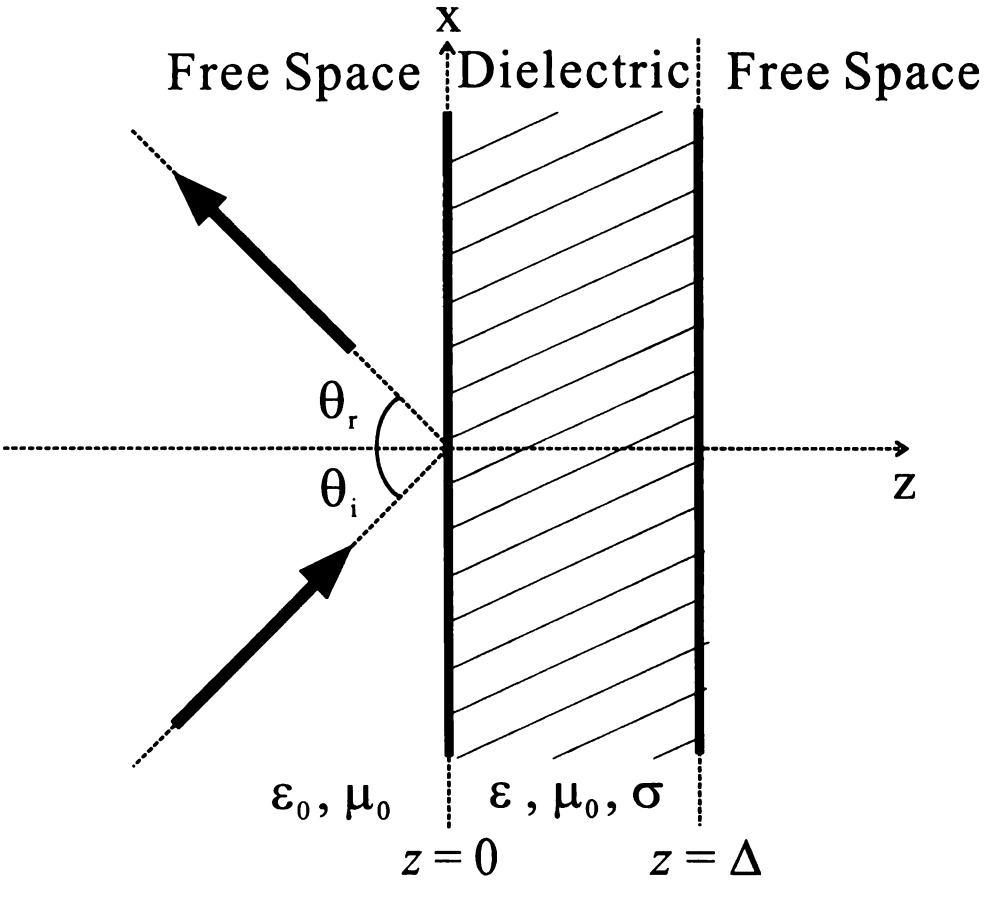

Figure 4.1: A uniform plane wave incident from free space upon a Air-backed lossy slab.

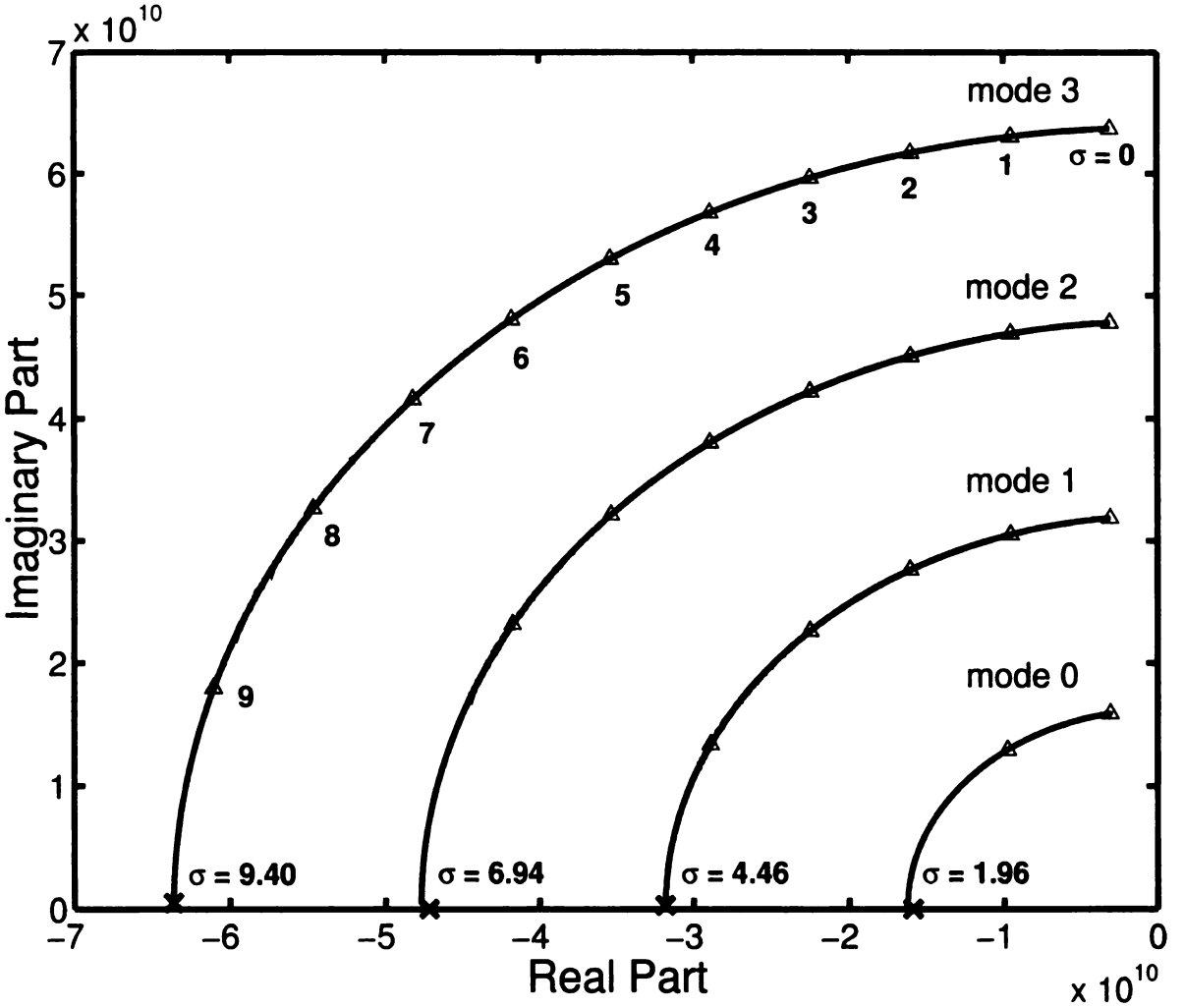

Figure 4.2: Pole trajectories of the reflection coefficient, $\perp$ polarization ($\epsilon_r = 9$, $\Delta = 2$ cm, $\theta_i = 30°$).

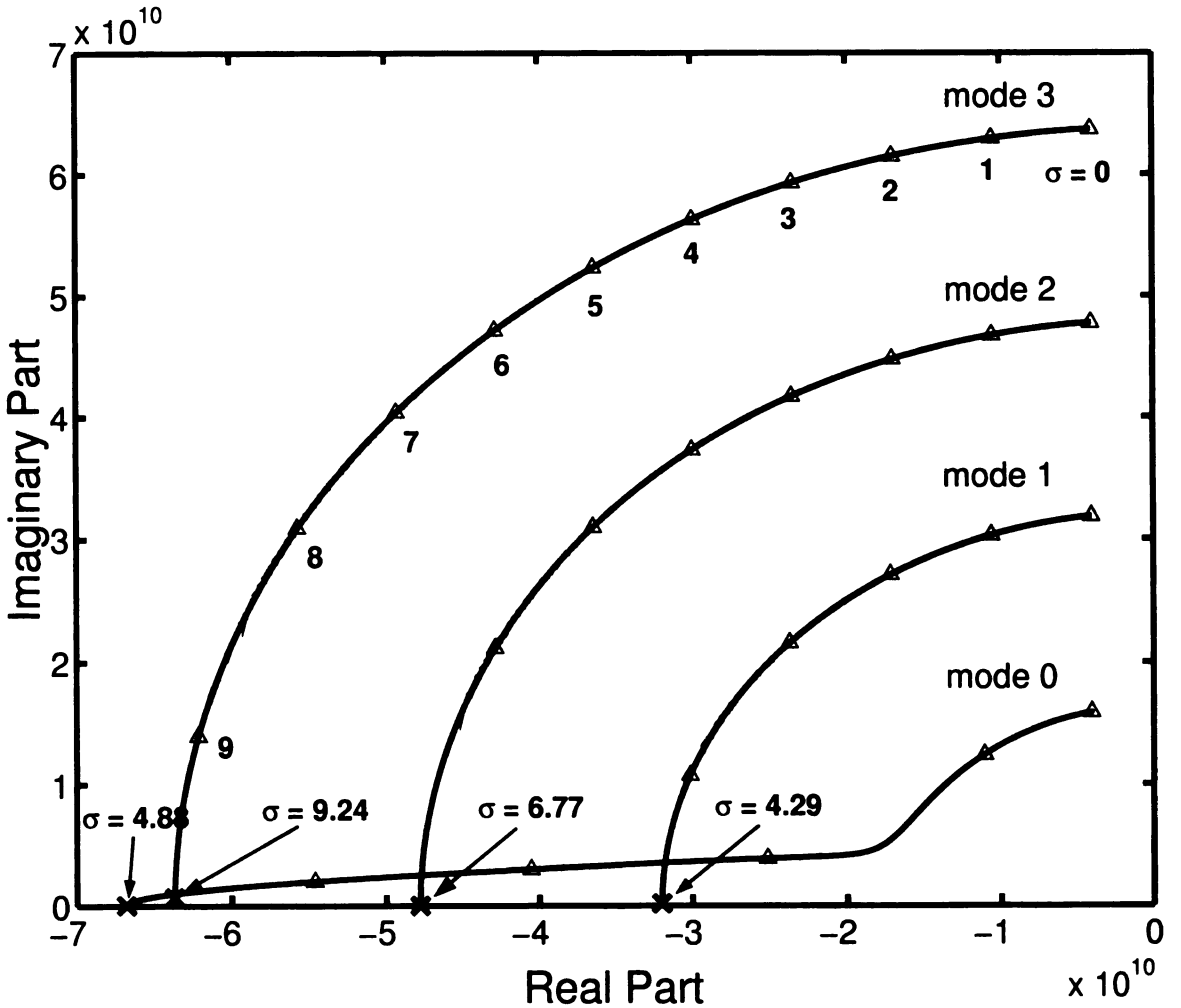

Figure 4.3: Pole trajectories of the reflection coefficient, || polarization ($\epsilon_r = 9$, $\Delta = 2$ cm, $\theta_i = 30°$).

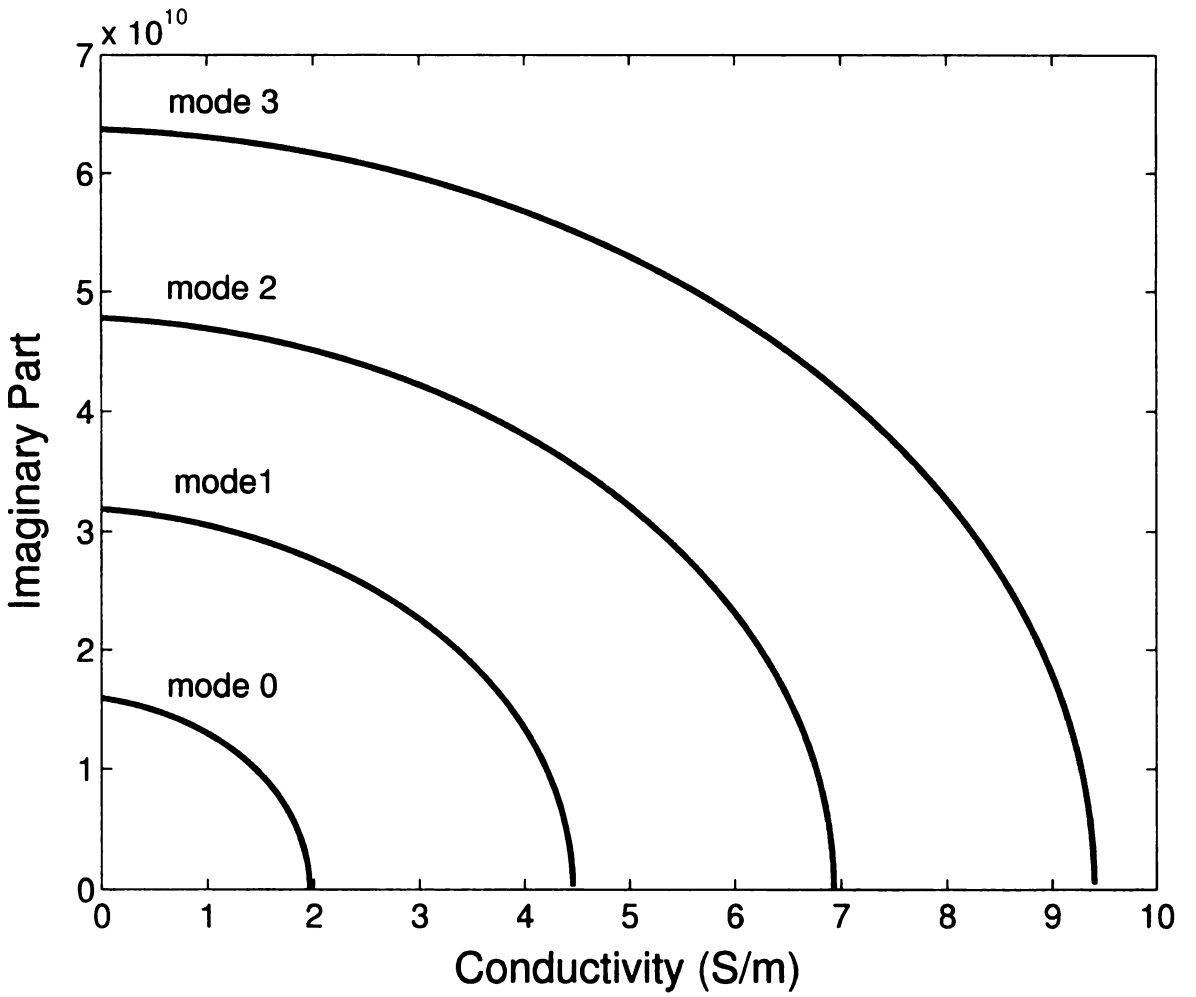

Figure 4.4: The amplitude of the imaginary parts of poles vs. conductivity, $\perp$ polarization ($\epsilon_r = 9$, $\Delta = 2$ cm, $\theta_i = 30°$, $\sigma = 0 \rightarrow 10.0$ S/m).

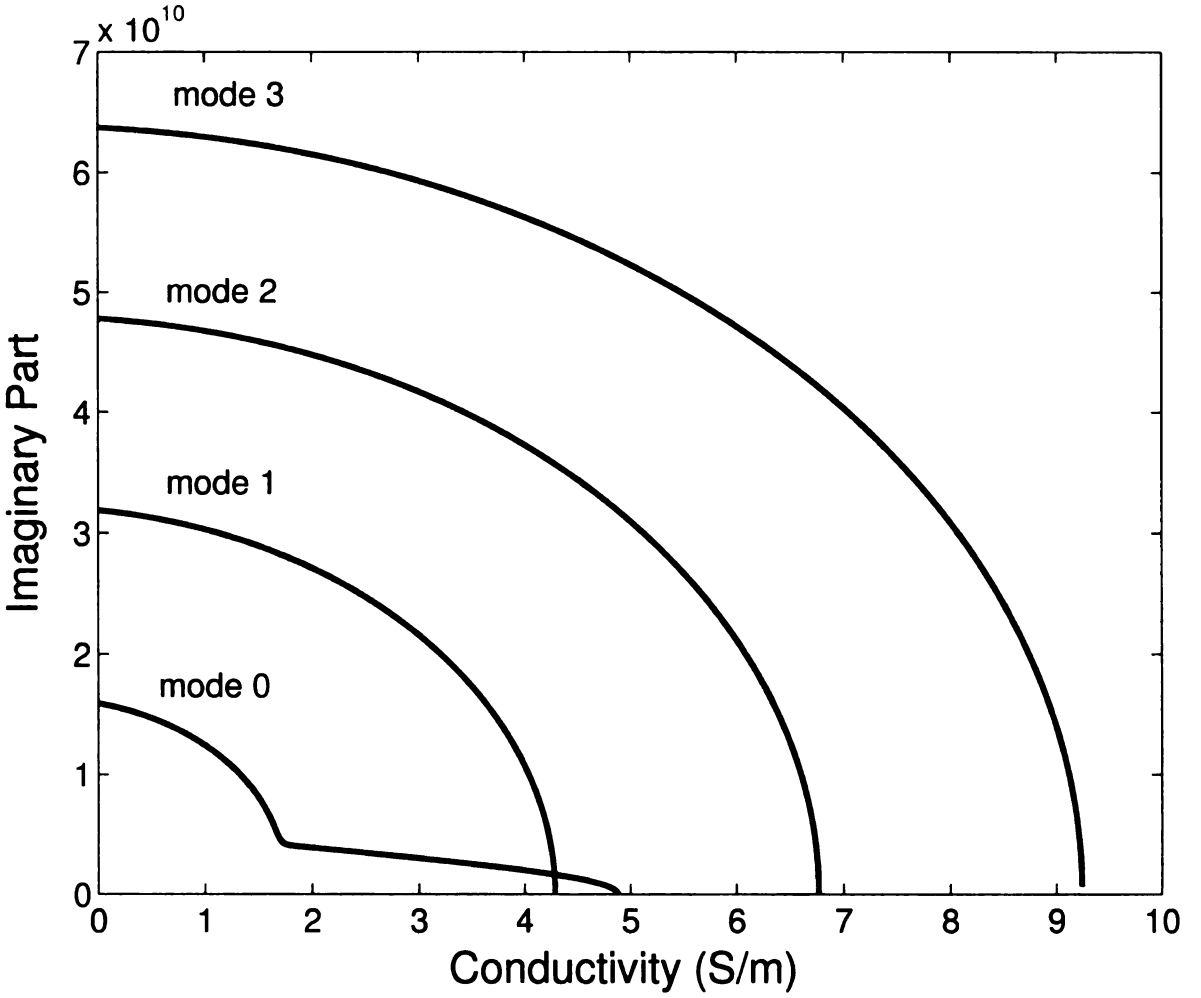

Figure 4.5: The amplitude of the imaginary parts of poles vs. conductivity, $\|$ polarization ($\epsilon_r = 9$, $\Delta = 2$ cm, $\theta_i = 30°$, $\sigma = 0 \rightarrow 10.0$ S/m).

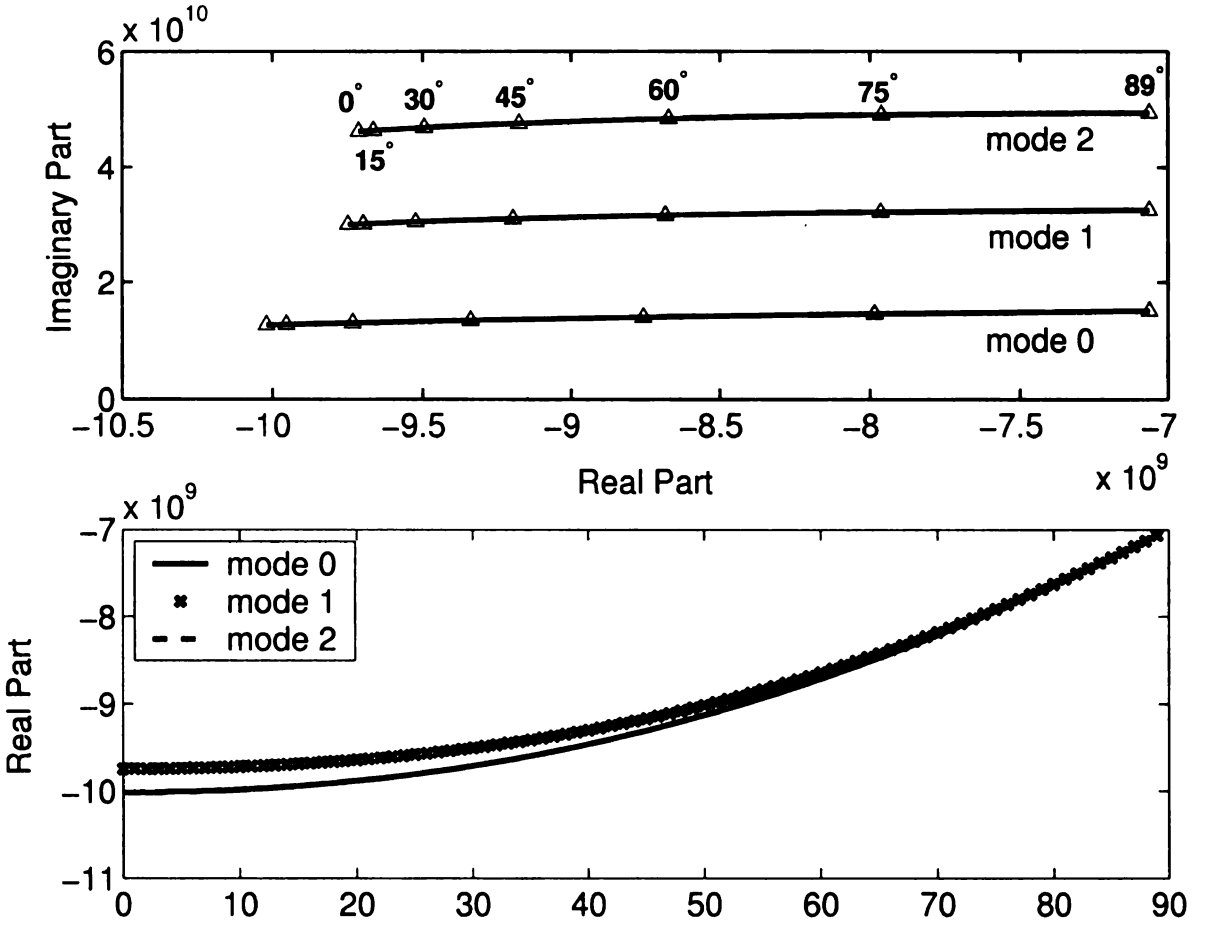

Figure 4.6: Pole trajectories of the reflection coefficient vs. angle of incidence, $\perp$ polarization ($\epsilon_r = 9$, $\Delta = 2$ cm, $\sigma = 1.0$ S/m).

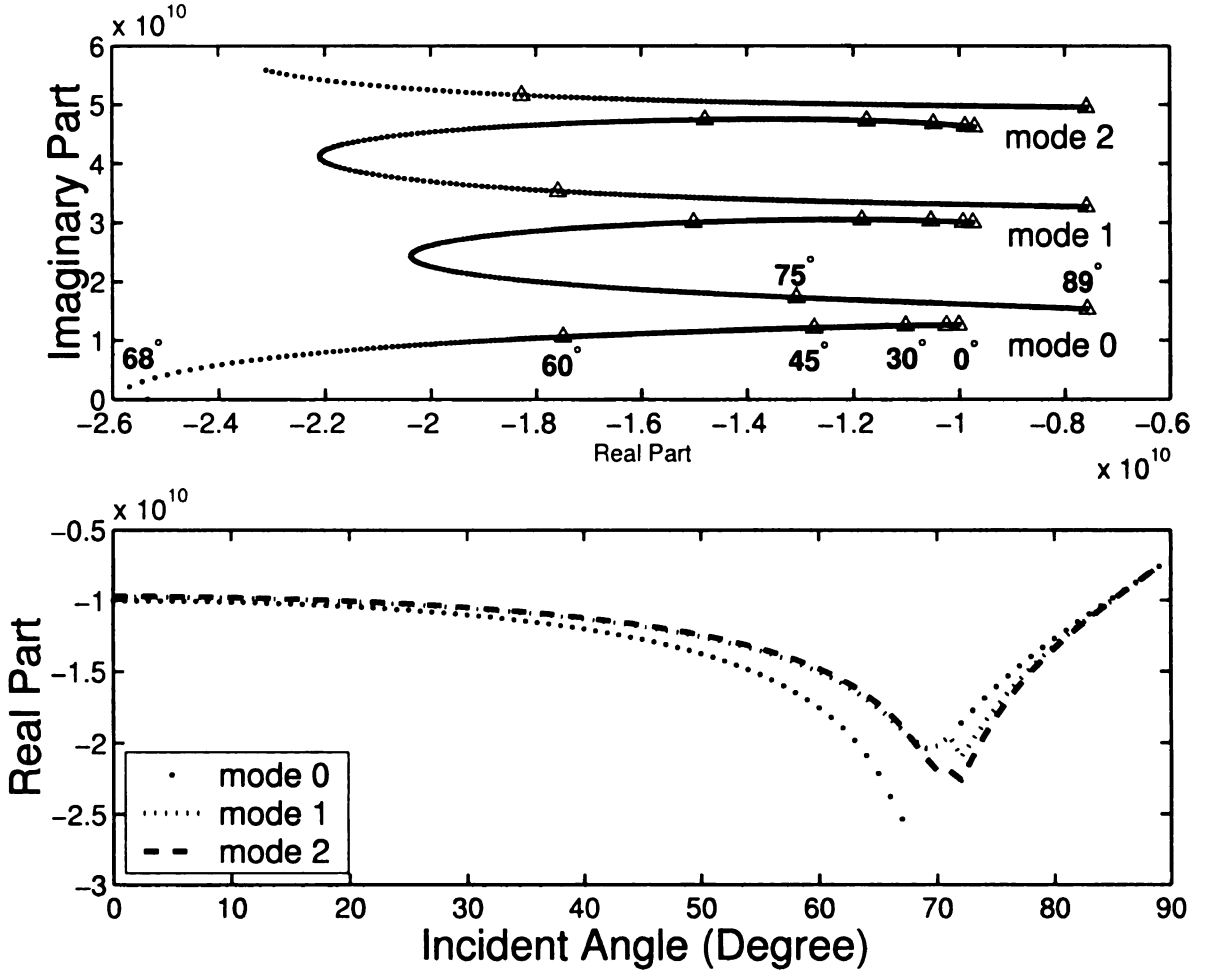

Figure 4.7: Pole trajectories of the reflection coefficient vs. angle of incidence, $\|$ polarization ($\epsilon_r = 9$, $\Delta = 2$ cm, $\sigma = 1.0$ S/m).

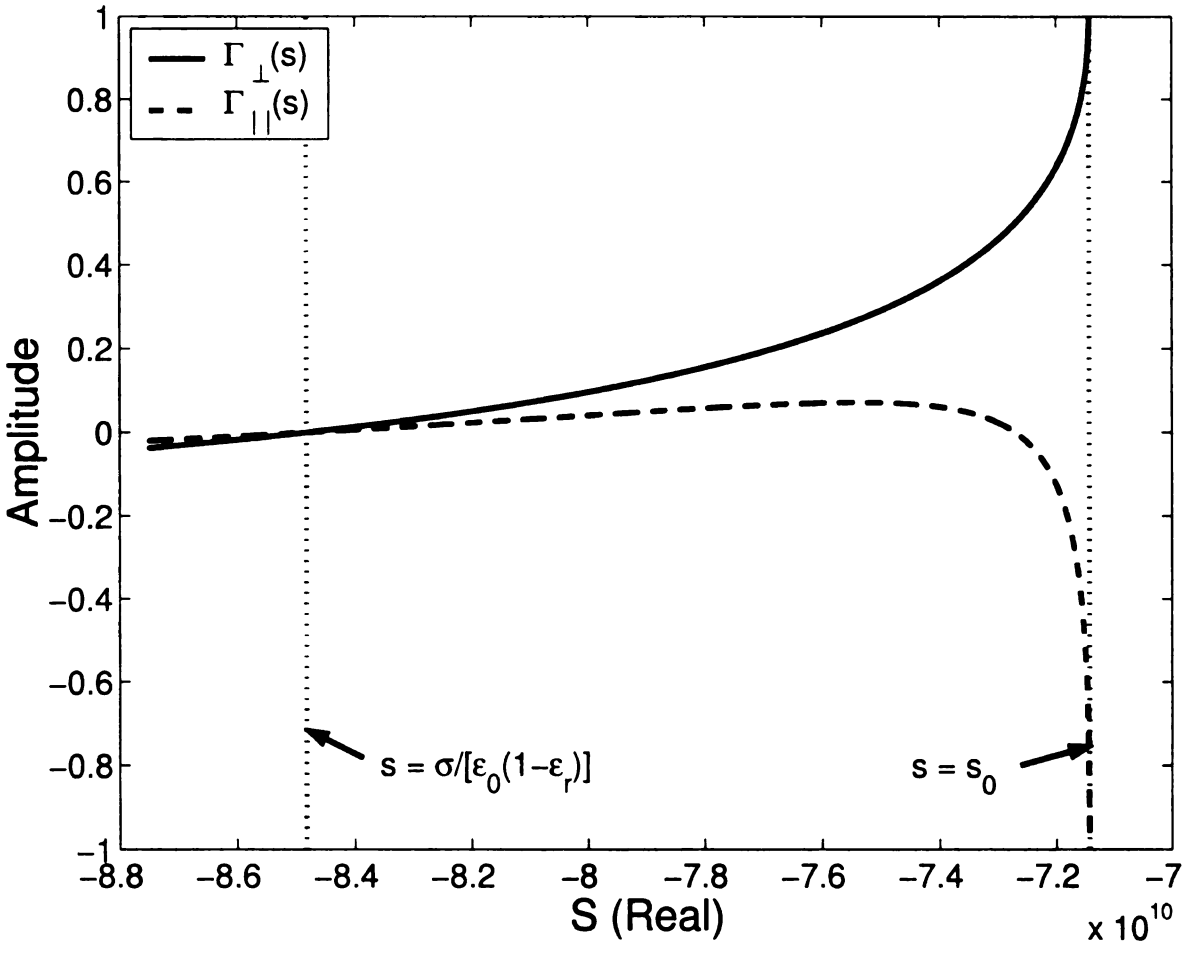

Figure 4.8: Amplitudes of the reflection coefficients ($\epsilon_r = 5$, $\Delta = 2$ cm, $\sigma = 3.0$ S/m, $\theta_i = 30°$).

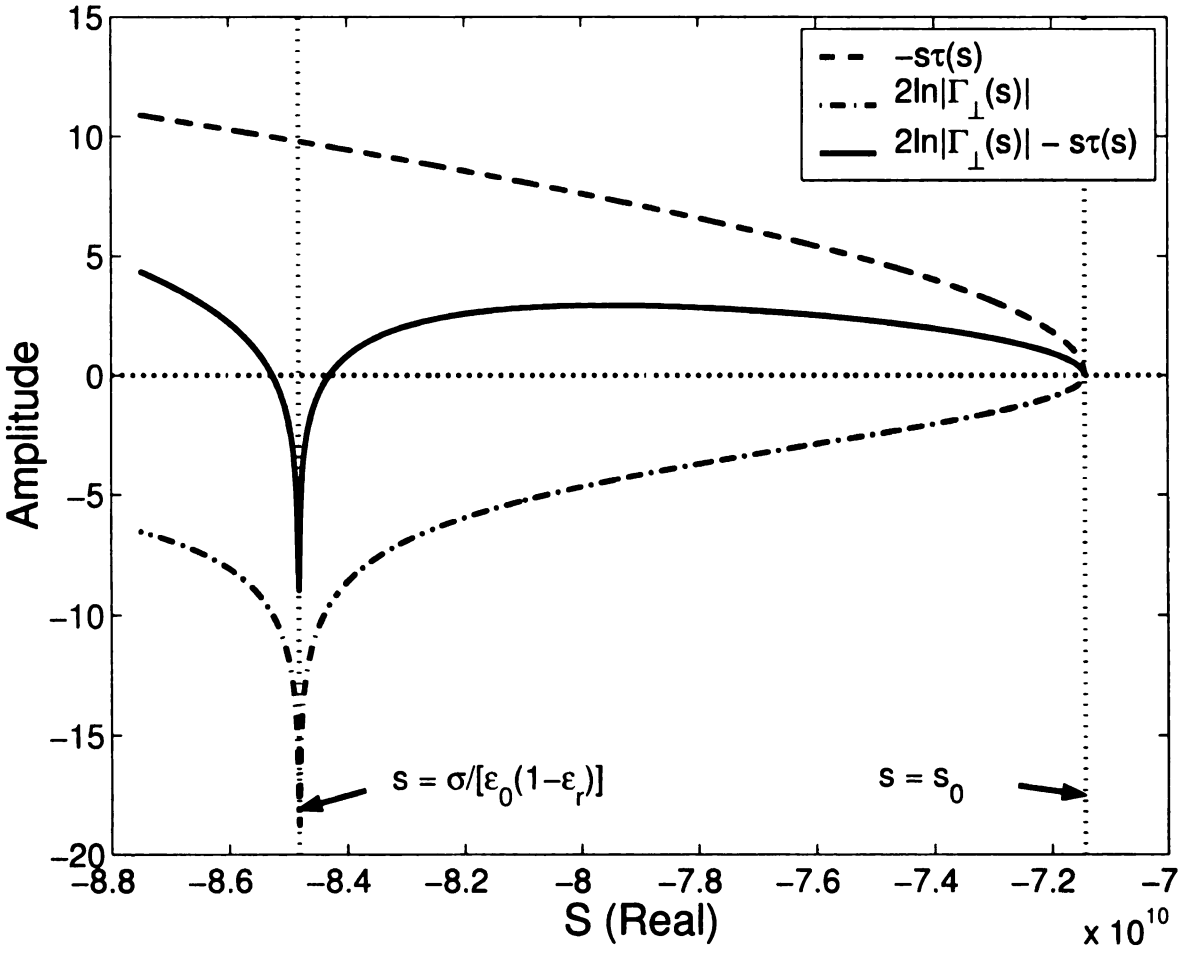

Figure 4.9: Real pole ($s < s_0$), ($\epsilon_r = 5$, $\Delta = 2$ cm, $\sigma = 3.0$ S/m, $\theta_i = 30°$).

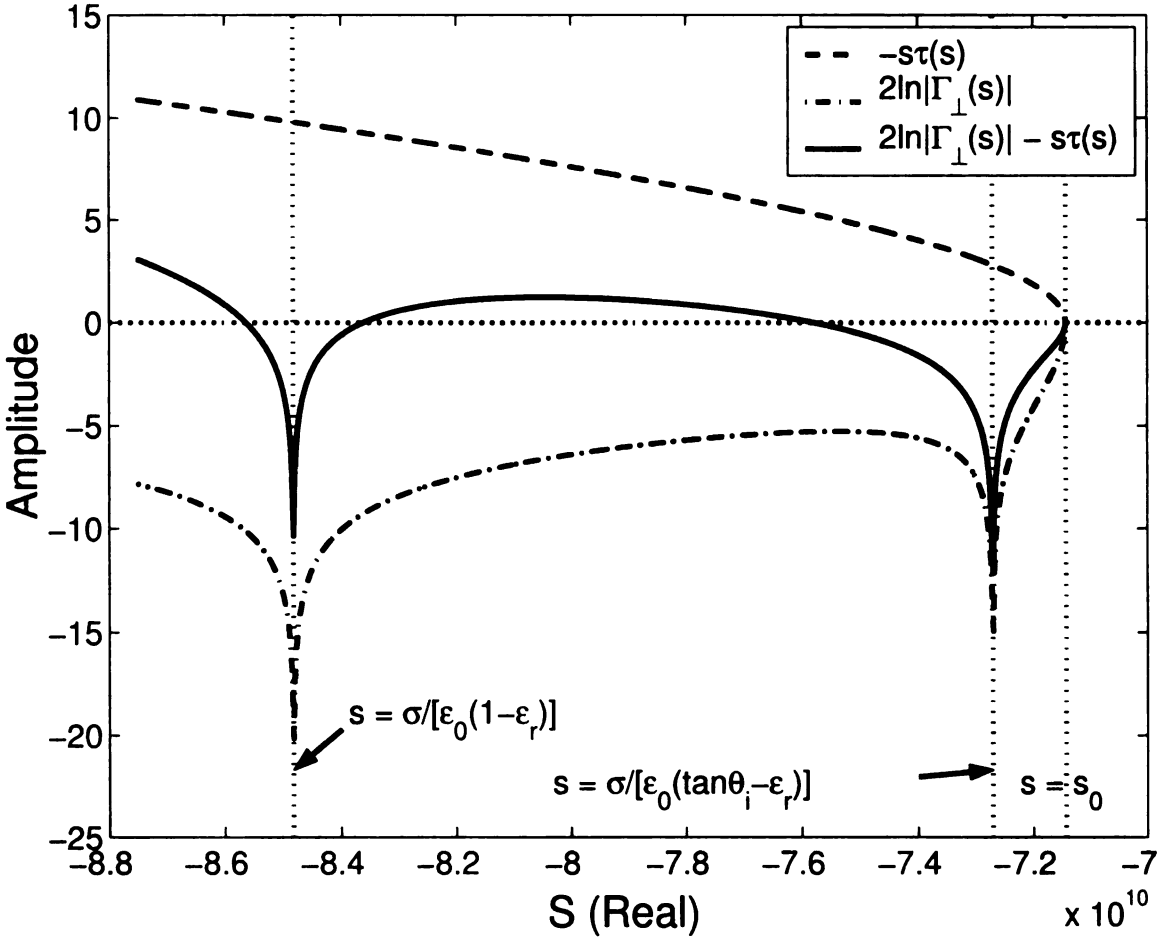

Figure 4.10: Real pole ($s < s_0$), ($\epsilon_r = 5$, $\Delta = 2$ cm, $\sigma = 3.0$ S/m, $\theta_i = 30°$).

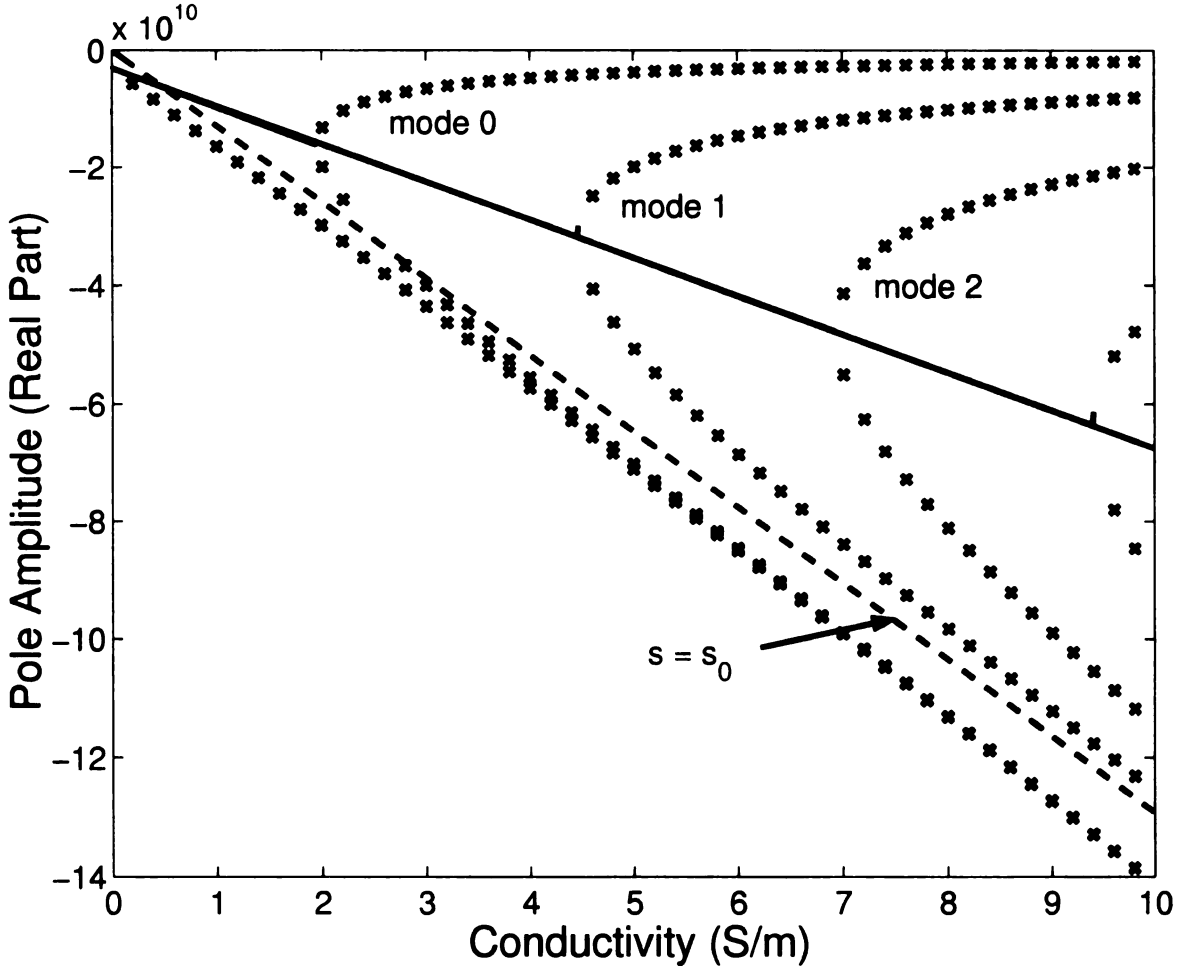

Figure 4.11: Complete sketch of the pole trajectories showing both complex and real poles, $\perp$ polarization ($\epsilon_r = 9$, $\Delta = 2$ cm, $\theta_i = 30°$).

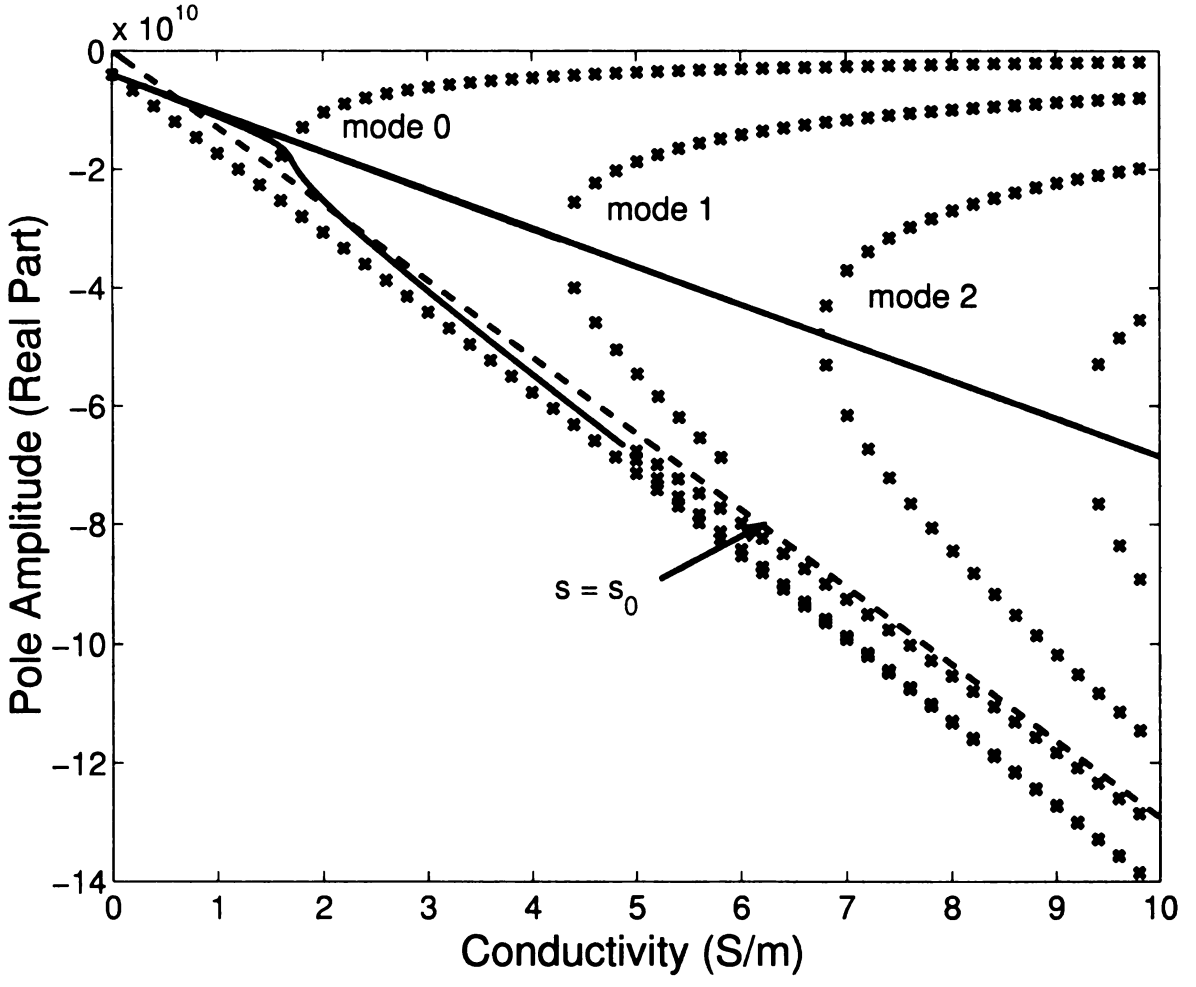

Figure 4.12: Complete sketch of the pole trajectories showing both complex and real poles, $\|$ polarization ($\epsilon_r = 9$, $\Delta = 2$ cm, $\theta_i = 30°$).

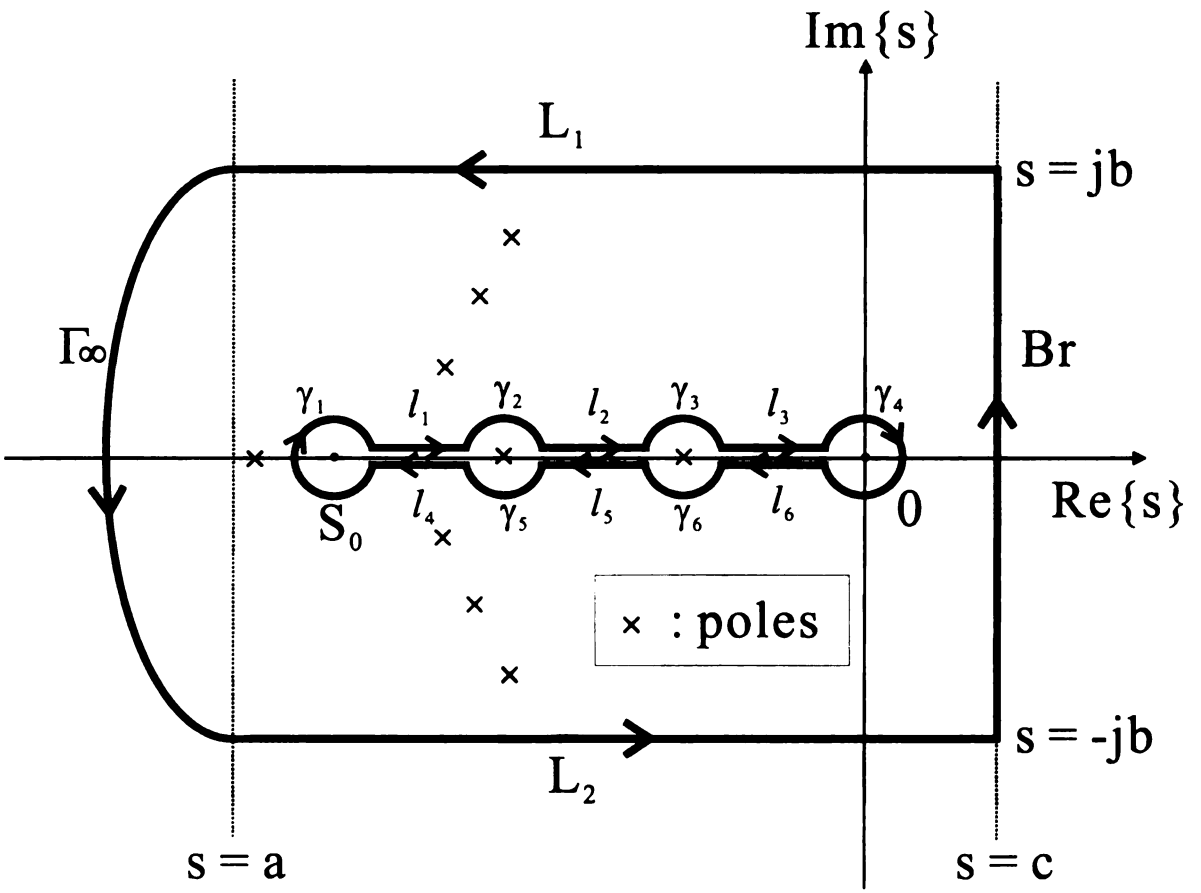

Figure 4.13: The integration contour when $t > \tau_0$. $|a|, |b| \to \infty$, $0 < c < \infty$.

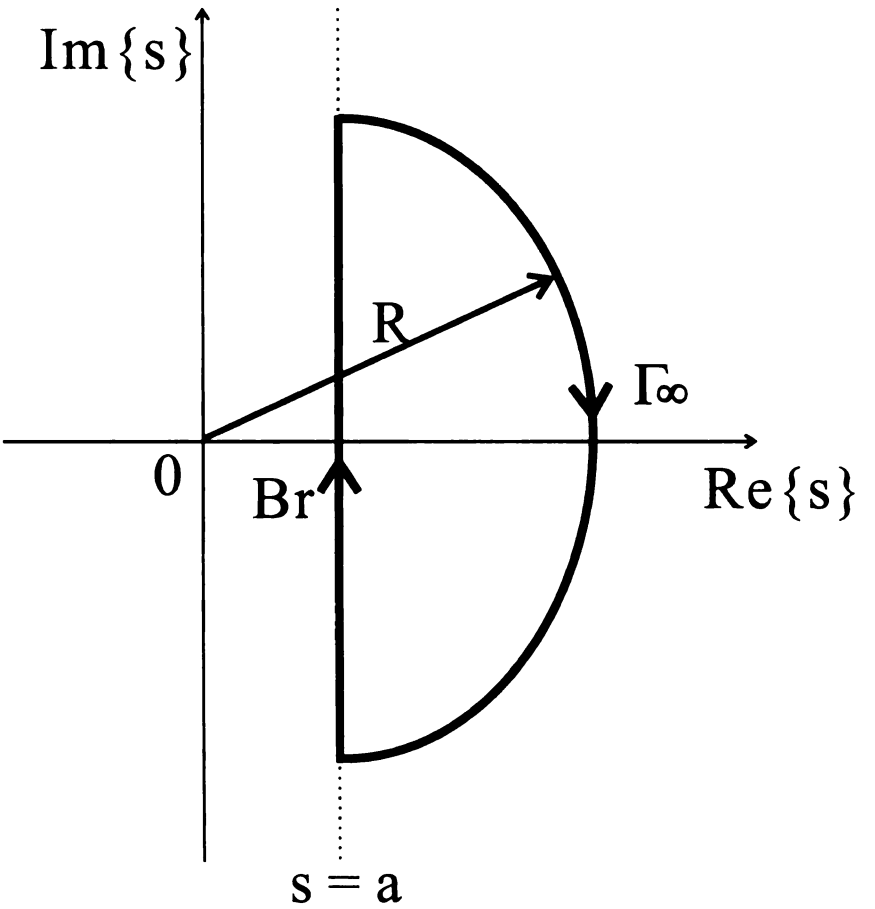

Figure 4.14: The integration contour when $t < \tau_0$. $R \to \infty$, $0 < a < \infty$.

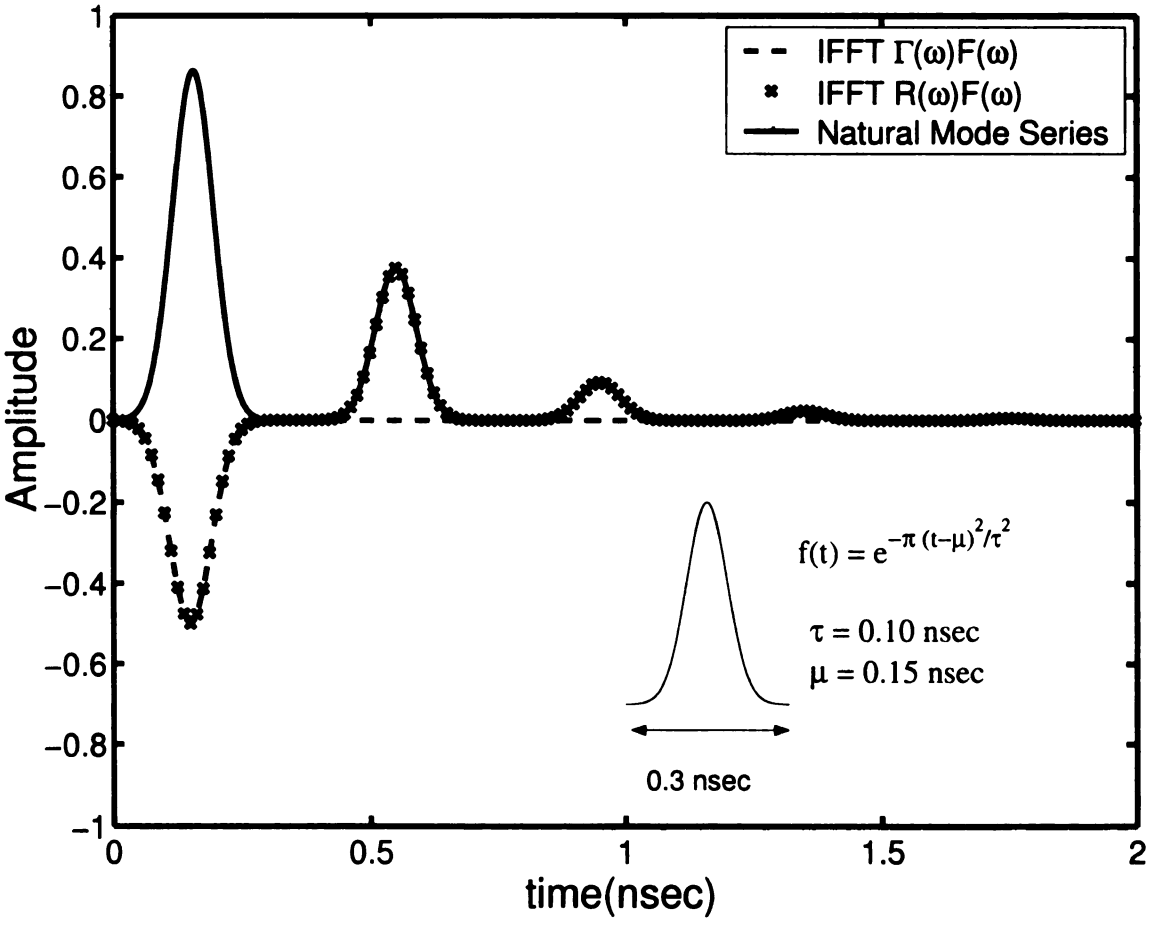

Figure 4.15: Time domain response, lossless case ($\epsilon_r = 9$, $\Delta = 2$ cm, $\theta_i = 0°$). Inset shows equivalent transmitted waveform.

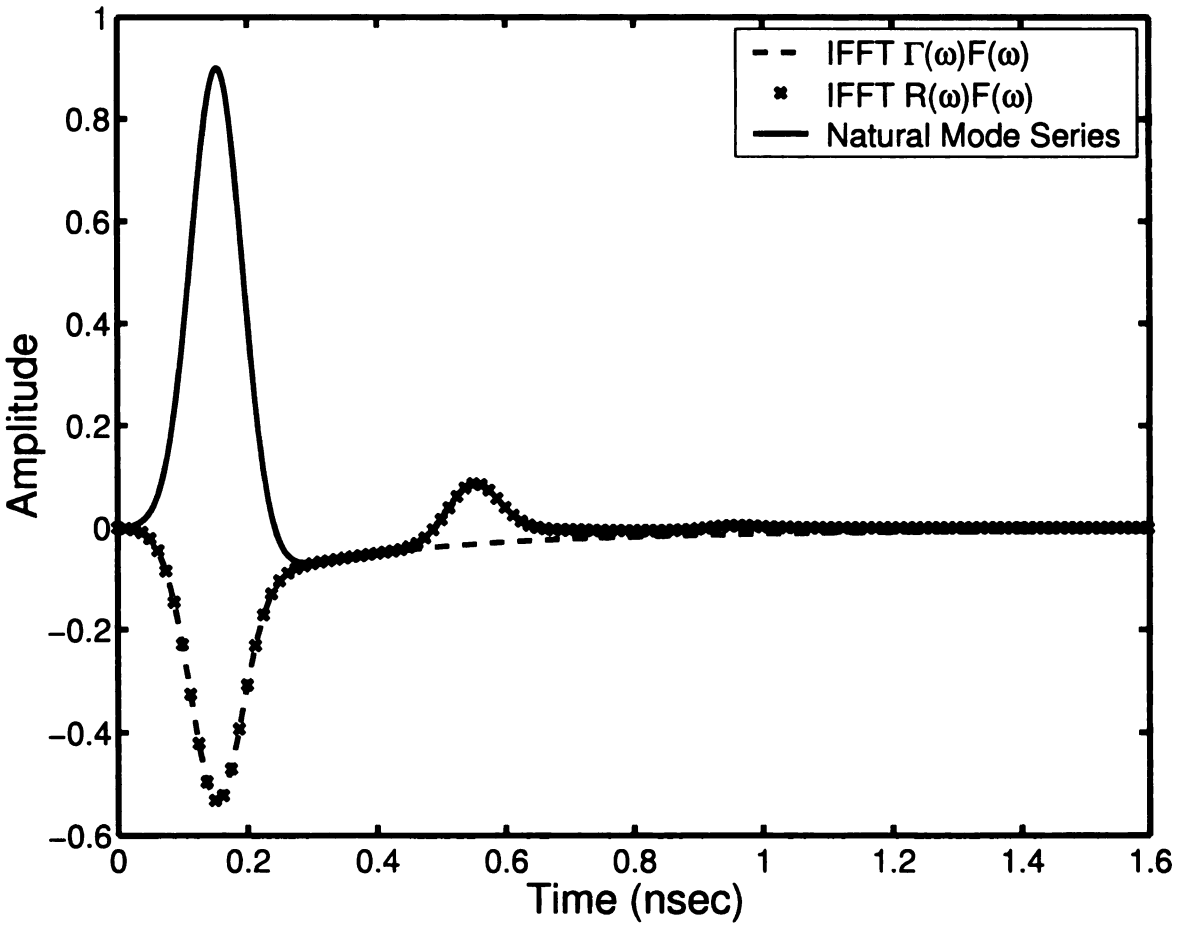

Figure 4.16: Time domain response, $\|$ polarization ($\epsilon_r = 9$, $\Delta = 2$ cm, $\theta_i = 20°$, $\sigma = 0.5$ S/m).

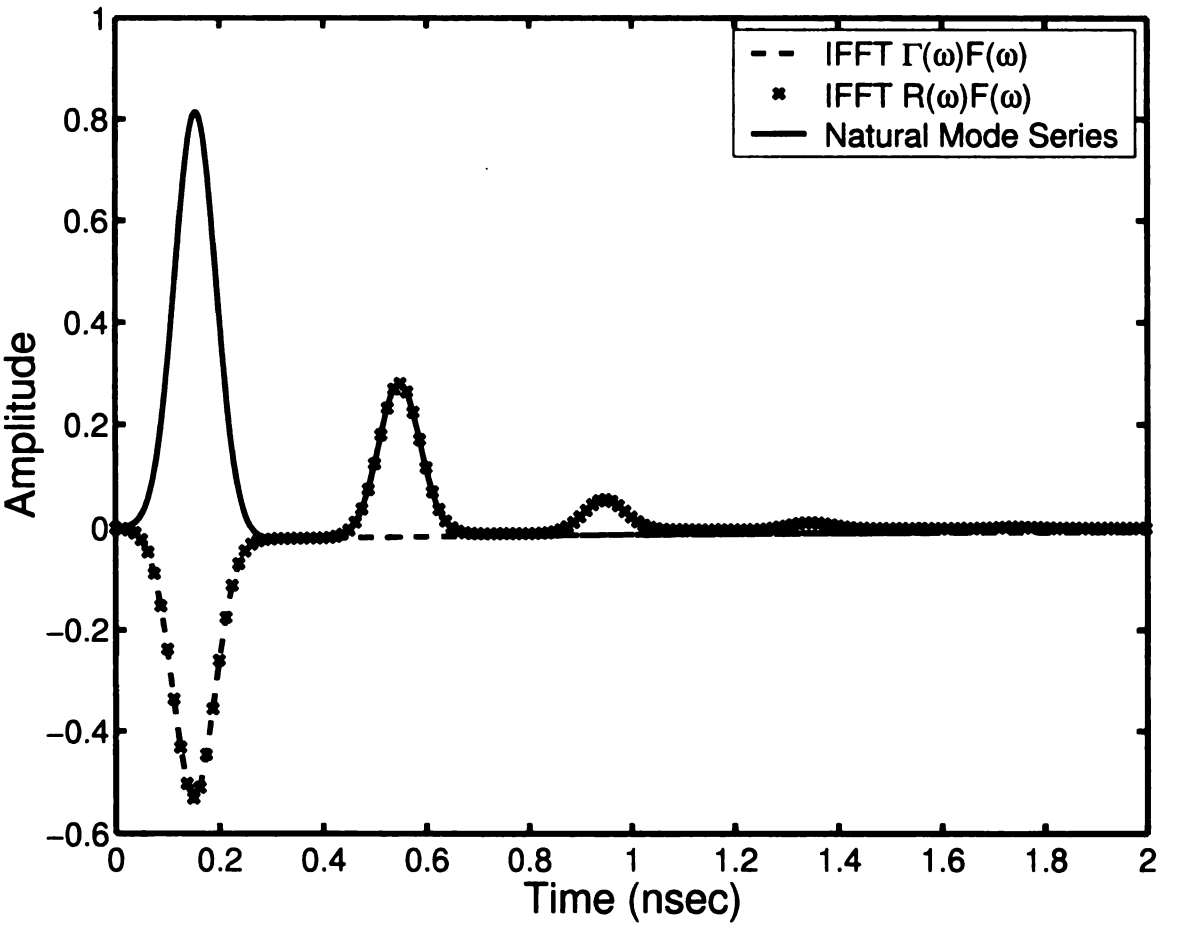

Figure 4.17: Time domain response, $\perp$ polarization ($\epsilon_r = 9$, $\Delta = 2$ cm, $\theta_i = 20°$, $\sigma = 0.1$ S/m).

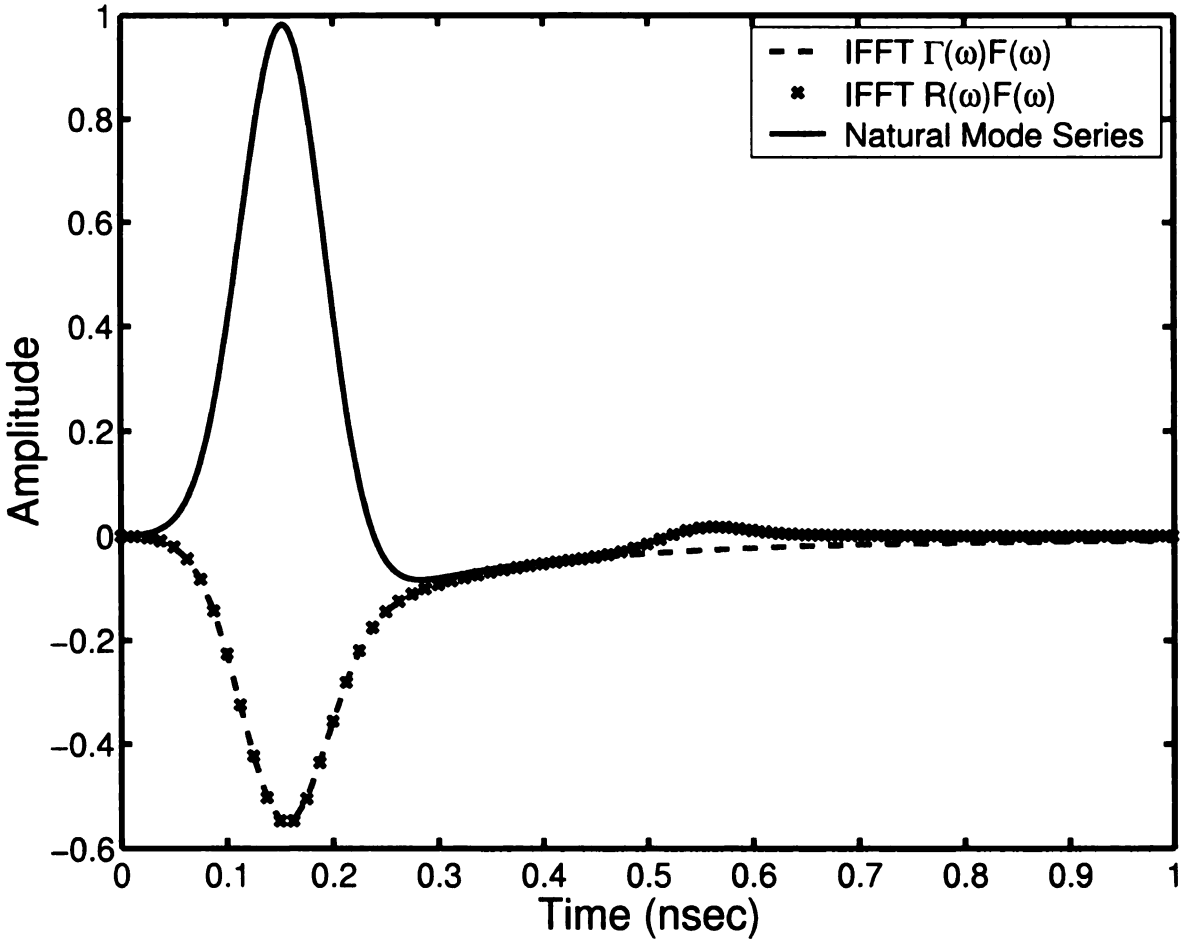

Figure 4.18: Time domain response, $\|$ polarization ($\epsilon_r = 9$, $\Delta = 2$ cm, $\theta_i = 30°$, $\sigma = 1.0$ S/m).

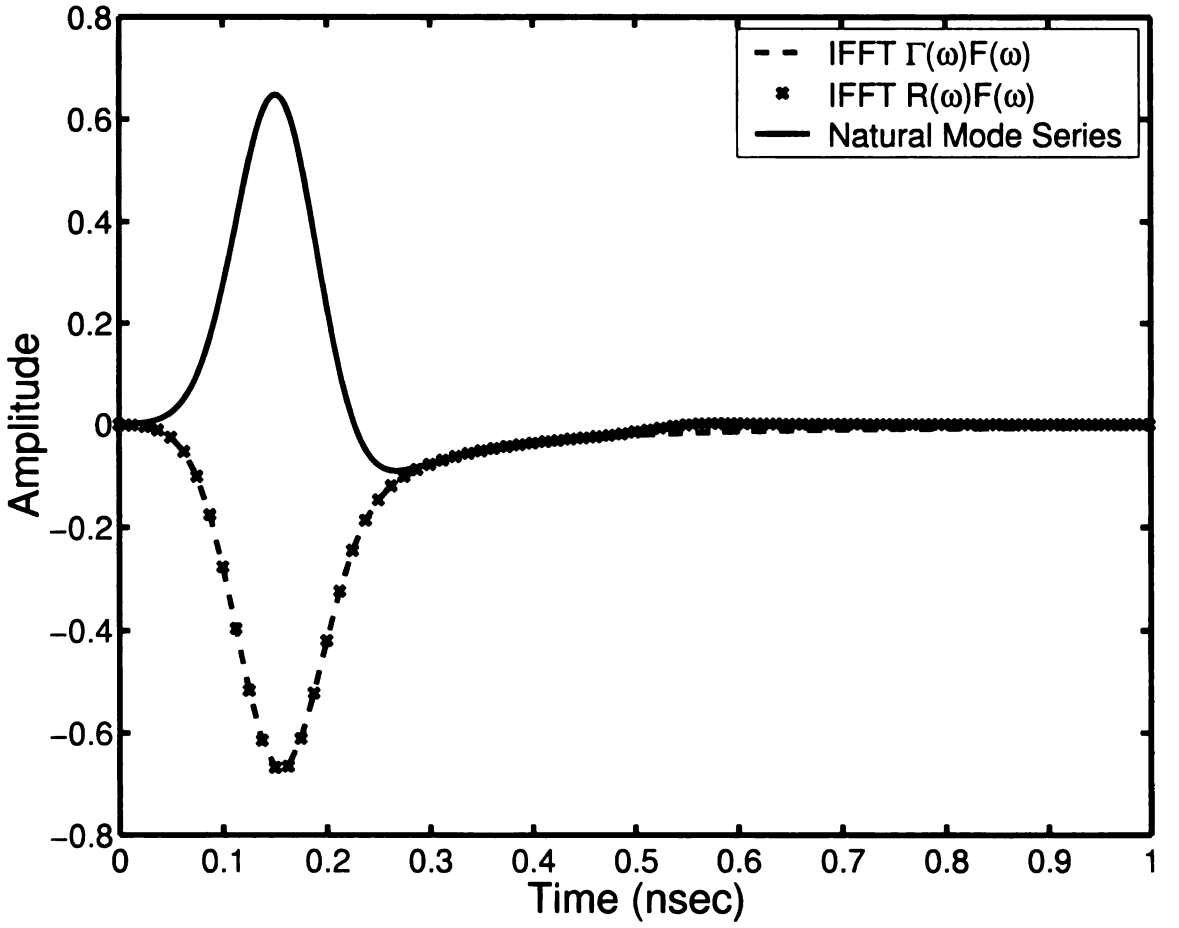

Figure 4.19: Time domain response, $\perp$ polarization ($\epsilon_r = 9$, $\Delta = 2$ cm, $\theta_i = 30°$, $\sigma = 1.5$ S/m).

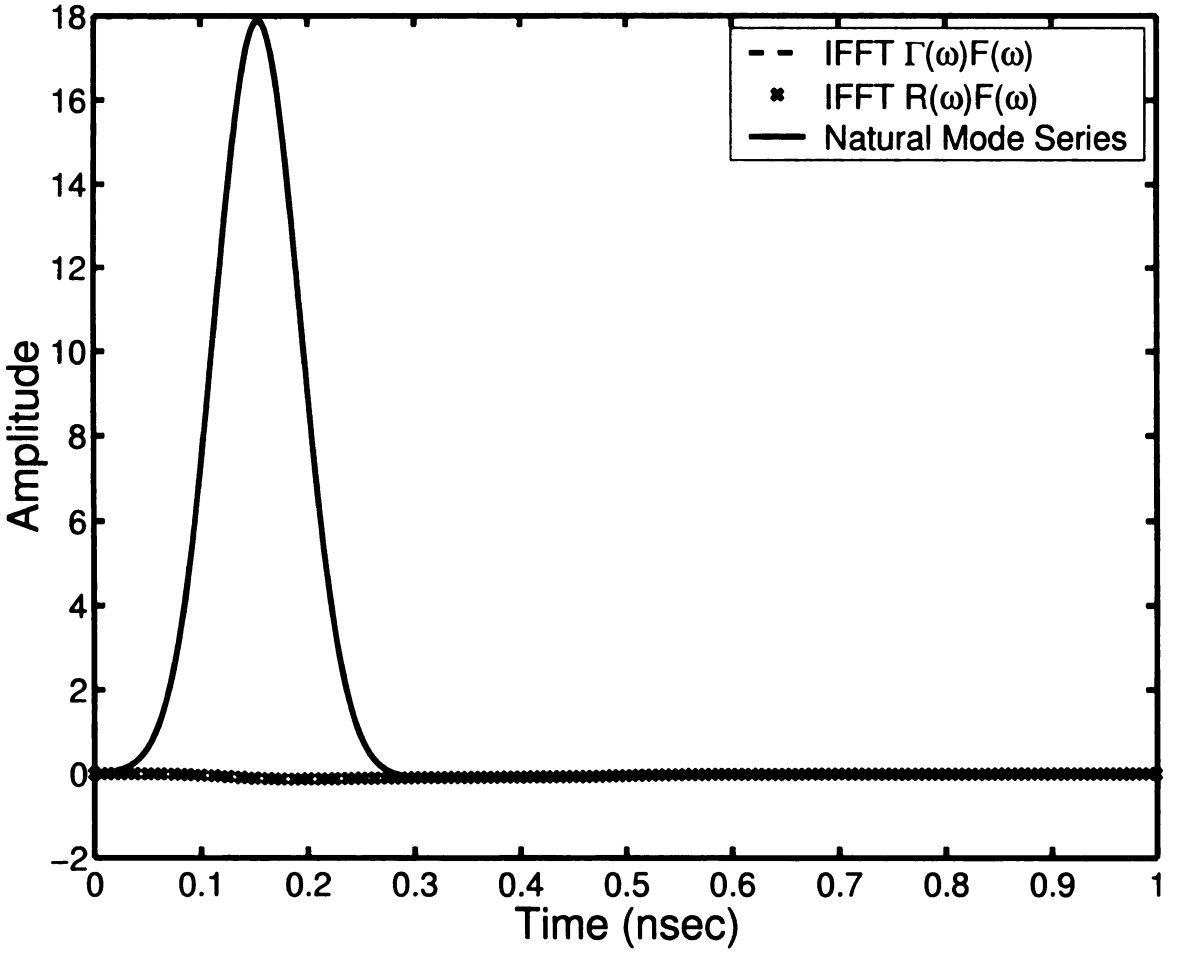

Figure 4.20: Time domain response, $\|$ polarization ($\epsilon_r = 9$, $\Delta = 2$ cm, $\theta_i = 70°$, $\sigma = 0.5$ S/m).

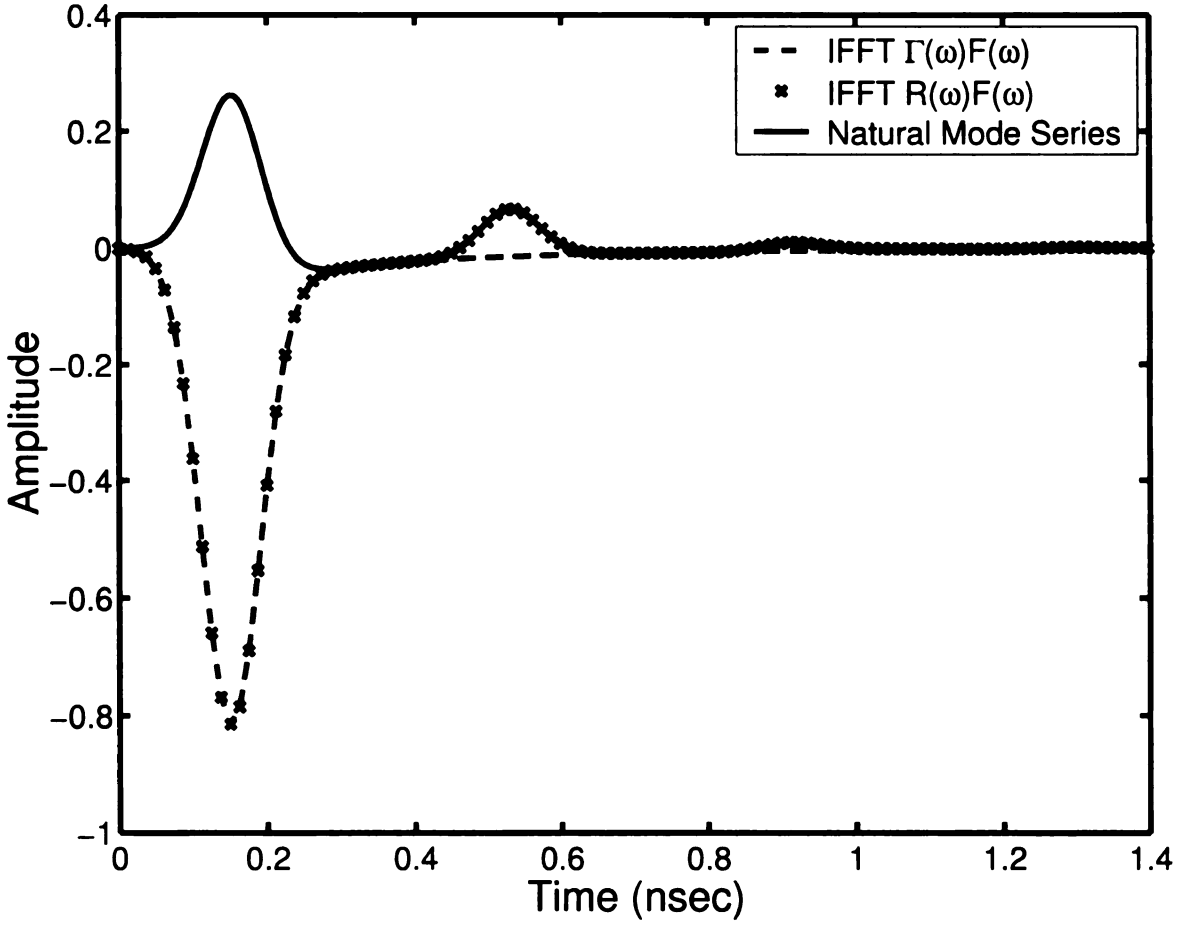

Figure 4.21: Time domain response, $\perp$ polarization ($\epsilon_r = 9$, $\Delta = 2$ cm, $\theta_i = 70°$, $\sigma = 0.5$ S/m).

Chapter 5: Natural Mode Analysis of a Single Layer with Debye Material

In Chapter 3 and Chapter 4, a lossy slab of material with frequency independent material parameters $\epsilon = \epsilon_r\epsilon_0$, μ_0, and σ was considered. However, the time and frequency dependence of the dielectric response necessitates the use of the time and frequency dependent permittivity models such as the Debye and the Cole-Cole models [28]-[31]. In this chapter, the Debye model, which is especially suitable for representing liquid polar materials, will be considered. Note that the primary purpose of this chapter is to show the validity and the applicability of the natural resonance representation of the transient dielectric response, rather than to discuss the theory of the dielectric properties. In the following discussion, both the conductor-backed and the air-backed cases will be considered, and the developments made in the previous chapters will be applied without discussing the details. However, in some parts the discussions will be repeated in order to clarify the developments.

5.1 Formulation of the frequency-domain reflection

The geometry of the Debye material case is the same as the frequency-independent material case except for the frequency-dependent

permittivity represented by the Debye equation [15], which is written as

$$\epsilon(s) = \epsilon_\infty + \frac{\epsilon_s - \epsilon_\infty}{1 + s\xi}, \tag{5.1}$$

where $s = j\omega$, ξ is the relaxation time of the dielectric, ϵ_s is the real static permittivity obtained when $\omega \to 0$, and ϵ_∞ is the real optical permittivity describing the high frequency behavior. Note that $\epsilon_s > \epsilon_\infty$ in order to describe the dielectric loss. Also, note that both ω and s will appear in the following discussions for clarifying the developments.

The Debye model often includes a conductivity term. Then the complex permittivity becomes [29], [32]

$$\epsilon_c(s) = \epsilon_\infty + \frac{\epsilon_s - \epsilon_\infty}{1 + s\xi} + \frac{\sigma}{s}. \tag{5.2}$$

Here, the last term represents the loss due to the conduction current. It cannot be absorbed into (5.1), since they represent different processes. Hence, the $\hat{z}$ directed wave number of the dielectric slab becomes

$$\begin{aligned}
k_{z,1} &= \sqrt{k_1^2 - k_{x,1}^2} \\
&= \sqrt{\omega^2\mu_0\epsilon_c(\omega) - \omega^2\mu_0\epsilon_0\sin^2\theta_i} \\
&= \omega\sqrt{\mu_0\epsilon_0}\sqrt{\frac{\epsilon_c(\omega)}{\epsilon_0} - \sin^2\theta_i} \\
&= \frac{\omega}{c}\sqrt{\frac{\epsilon_\infty}{\epsilon_0} - \sin^2\theta_i + \frac{s(\epsilon_s - \epsilon_\infty) + \sigma(1 + s\xi)}{\epsilon_0 s(1 + s\xi)}} \\
&= -j\frac{s}{c}\sqrt{\frac{(\epsilon_\infty - \epsilon_0\sin^2\theta_i)(s + s^2\xi) + s(\epsilon_s - \epsilon_\infty) + \sigma(1 + s\xi)}{\epsilon_0 s(1 + s\xi)}} \\
&= -j\frac{s}{c}\sqrt{\frac{s^2\xi(\epsilon_\infty - \epsilon_0\sin^2\theta_i) + s(\epsilon_s + \sigma\xi - \epsilon_0\sin^2\theta_i) + \sigma}{\epsilon_0 s(1 + s\xi)}} \\
&= -j\frac{\chi}{c}\frac{\sqrt{s}}{\sqrt{s + 1/\xi}}\sqrt{s^2 + Bs + C},
\end{aligned} \tag{5.3}$$

where

$$\begin{aligned}
\chi &= \sqrt{\frac{\epsilon_\infty}{\epsilon_0} - \sin^2\theta_i}, \\
B &= \frac{\epsilon_s + \xi\sigma - \epsilon_0 \sin^2\theta_i}{\xi(\epsilon_\infty - \epsilon_0 \sin^2\theta_i)}, \\
C &= \frac{\sigma}{\xi(\epsilon_\infty - \epsilon_0 \sin^2\theta_i)}
\end{aligned}$$

The roots of the quadratic equation in (5.3) are

$$s = \frac{-B \pm \sqrt{B^2 - 4C}}{2}.$$

Here, it can be shown that these roots are non-positive real, since

$$B^2 - 4C = \frac{(\epsilon_s + \xi\sigma - \epsilon_0 \sin^2\theta_i)^2 - 4\xi\sigma(\epsilon_\infty - \epsilon_o \sin^2\theta_i)}{\xi^2(\epsilon_\infty - \epsilon_0 \sin^2\theta_i)^2}, \tag{5.4}$$

and the numerator of this equation becomes

$$\begin{aligned}
& (\epsilon_s + \xi\sigma - \epsilon_0 \sin^2\theta_i)^2 - 4\xi\sigma(\epsilon_\infty - \epsilon_o \sin^2\theta_i) \\
= \;& \epsilon_s^2 + 2\epsilon_s\xi\sigma + \xi^2\sigma^2 - 2\epsilon_s\epsilon_0 \sin^2\theta_i - 2\xi\sigma\epsilon_0 \sin^2\theta_i + \epsilon_0^2 \sin^4\theta_i - 4\xi\sigma\epsilon_\infty + 4\xi\sigma\epsilon_0 \sin^2\theta_i \\
= \;& \epsilon_s^2 - 2\epsilon_s\xi\sigma + \xi^2\sigma^2 - 2\epsilon_s\epsilon_0 \sin^2\theta_i + 2\xi\sigma\epsilon_0 \sin^2\theta_i + \epsilon_0^2 \sin^4\theta_i - 4\xi\sigma\epsilon_\infty + 4\epsilon_s\xi\sigma \\
= \;& (\epsilon_s - \xi\sigma - \epsilon_0 \sin^2\theta_i)^2 + 4\xi\sigma(\epsilon_s - \epsilon_\infty),
\end{aligned}$$

which is always positive ($\epsilon_s > \epsilon_\infty$).

As a result,

$$k_{z,1} = -j\frac{\chi}{c}\frac{\sqrt{s}\sqrt{s - s_1}\sqrt{s - s_3}}{\sqrt{s - s_2}}, \tag{5.5}$$

where

$$\begin{aligned} s_1 &= \frac{-B+\sqrt{B^2-4C}}{2}, \\ s_2 &= -\frac{1}{\xi}, \\ s_3 &= \frac{-B-\sqrt{B^2-4C}}{2}. \end{aligned}$$

Here, it is found that $s_3 < s_2 < s_1 \leq 0$ by substituting s_2 for s into the quadratic equation in (5.3) and examining the sign of the result.

Therefore, by (3.3), (3.4) and (3.2) from Chapter 3,

$$s\tau(s) = jk_{z,1}2\Delta = \frac{2\Delta}{c}\chi\frac{\sqrt{s}\sqrt{s-s_1}\sqrt{s-s_3}}{\sqrt{s-s_2}}, \tag{5.6}$$

$$\begin{aligned} Z_1(s) &\equiv Z_\perp(s) = \frac{k_1\eta_1}{k_{z,1}} \\ &= \frac{\eta_0 s\sqrt{s-s_2}}{\chi\sqrt{s}\sqrt{s-s_1}\sqrt{s-s_3}}, \end{aligned} \tag{5.7}$$

$$\begin{aligned} Z_1(s) &\equiv Z_\parallel(s) = \frac{k_{z,1}\eta_1}{k_1} \\ &= \frac{\eta_0\epsilon_0\chi\sqrt{s}\sqrt{s-s_1}\sqrt{s-s_2}\sqrt{s-s_3}}{s(s\epsilon_\infty - s_2\epsilon_s)+\sigma(s-s_2)}. \end{aligned} \tag{5.8}$$

Hence for perpendicular polarization, the interfacial reflection coefficient is written as

$$\Gamma_\perp(s) = \frac{\cos\theta_i\sqrt{s}\sqrt{s-s_2} - \chi\sqrt{s-s_1}\sqrt{s-s_3}}{\cos\theta_i\sqrt{s}\sqrt{s-s_2} + \chi\sqrt{s-s_1}\sqrt{s-s_3}}, \tag{5.9}$$

and for parallel polarization

$$\Gamma_\parallel(s) = \frac{\epsilon_0\chi\sqrt{s}\sqrt{s-s_1}\sqrt{s-s_2}\sqrt{s-s_3} - \cos\theta_i[s(s\epsilon_\infty - s_2\epsilon_s)+\sigma(s-s_2)]}{\epsilon_0\chi\sqrt{s}\sqrt{s-s_1}\sqrt{s-s_2}\sqrt{s-s_3} + \cos\theta_i[s(s\epsilon_\infty - s_2\epsilon_s)+\sigma(s-s_2)]}. \tag{5.10}$$

The reflection coefficients $R(s)$ remain the same as in previous chapters, such that

$$R(s) = \frac{\Gamma(s) - e^{-s\tau(s)}}{1-\Gamma(s)e^{-s\tau(s)}}, \tag{5.11}$$

for the conductor-backed case and

$$R(s) = \frac{\Gamma(s)[1 - e^{-s\tau(s)}]}{1 - \Gamma^2(s)e^{-s\tau(s)}}. \tag{5.12}$$

for the air-backed case.

Thus, the impulse response $r(t)$ is obtained by

$$r(t) = \mathcal{L}^{-1}\{R(s)\} = \frac{1}{j2\pi}\int_{Br} R(s)e^{st}\mathrm{d}s \tag{5.13}$$

where Br indicates the Bromwich path. This integral can be evaluated by contour integration. We must thus examine the singularities and define an appropriate branch for the integrand.

Comparison with the frequency-independent material parameters case

If we let the static real permittivity ϵ_s be the same as the optical permittivity ϵ_∞, then from (5.4),

$$\begin{aligned}\sqrt{B^2 - 4C} &= \sqrt{\frac{(\epsilon_\infty - \xi\sigma - \epsilon_0 \sin^2\theta_i)^2}{\xi^2(\epsilon_\infty - \epsilon_0 \sin^2\theta_i)^2}} \\ &= \frac{(\epsilon_\infty - \xi\sigma - \epsilon_0 \sin^2\theta_i)}{\xi(\epsilon_\infty - \epsilon_0 \sin^2\theta_i)}.\end{aligned}$$

Therefore, s_3 becomes

$$s_3 = \frac{-B - \sqrt{B^2 - 4C}}{2} = -\frac{1}{\xi}, \tag{5.14}$$

which is equal to s_2, and

$$s_1 = \frac{-B + \sqrt{B^2 - 4C}}{2} = -\frac{\sigma}{\epsilon_\infty - \epsilon_0 \sin^2\theta_i} = -\frac{\sigma}{\epsilon_0\chi}. \tag{5.15}$$

Here, $\chi = \sqrt{\epsilon_\infty/\epsilon_0 - \sin^2\theta_i}$ is same as $\sqrt{\bar{\epsilon}}$, where $\bar{\epsilon} = \epsilon_r - \sin^2\theta_i$ as defined in Chapter 3, by letting $\epsilon_\infty/\epsilon_0 = \epsilon_r$. Note that $\sqrt{s-s_3}$ and $\sqrt{s-s_2}$ in (5.5) cancel each other, since $s_3 = s_2$. As a result, (5.5)-(5.8) become the same as (3.2), (3.7), (3.9) and (3.10) respectively; i.e., the current case becomes the frequency-independent material parameters case if $\epsilon_s = \epsilon_\infty$.

On the other hand, if the DC conductivity σ is 0, then s_1 becomes 0 resulting in

$$k_{z,1} = -j\frac{\chi}{c}s\frac{\sqrt{s-s_3}}{\sqrt{s-s_2}}. \tag{5.16}$$

It should be noted that there are only two branch points left for the above special cases.

5.2 Singularities and the branch cut

From the complex square roots in $s\tau(s)$ and $Z_1(s)$, the branch points are located at $s = 0$, $s = s_1$, $s = s_2$ and $s = s_3$. These branch points are non-positive real, and are related by $s_3 < s_2 < s_1 \leq 0$. It should be noted that $R(s)$ is continuous about the negative real axis between s_1 and s_2, i.e., $s\tau(s)$ and $\Gamma(s)$ are continuous. Therefore, unlike the previous cases, in order to ensure the continuity of $R(s)$, two separate branch cuts are made, such that one is taken along the negative real axis between 0 and s_1 and the other is taken along the negative real axis between s_2 and s_3.

From (5.11) and (5.12), the poles should satisfy

$$\ln\left|\Gamma(s)e^{-s\tau(s)}\right| + j\arg\left[\Gamma(s)e^{-s\tau(s)}\right] = 0, \tag{5.17}$$

for the conductor backed case, and

$$\ln\left|\Gamma^2(s)e^{-s\tau(s)}\right| + j\arg\left[\Gamma^2(s)e^{-s\tau(s)}\right] = 0, \tag{5.18}$$

for the air-backed case.

Except for the lossless case ($\epsilon_s = \epsilon_\infty$ and $\sigma = 0$), wherein the poles can be calculated analytically, the above equations need to be solved numerically. When calculating the poles numerically, it is very important to have good initial guesses and to know the approximate pole behavior. In this work, the lossless case poles were used as the initial guesses. In order to trace the poles correctly, first the poles are traced by gradually increasing the conductivity while keeping ϵ_s the same as ϵ_∞. When the conductivity reaches the target value, ϵ_s is then increased to its desired value.

Figures 5.1-5.3 show the pole trajectories obtained by the Newton-Rahpson method for the conductor-backed, parallel polarization case, when the ϵ_s varies from $5.0\epsilon_0$ to $78.3\epsilon_0$, where $\epsilon_\infty = 5.0\epsilon_0$, $\xi = 9.6 \times 10^{-12}$ sec and $\sigma = 0.5$ S/m. In the figures the amplitudes vs. the ratios of ϵ_s to ϵ_∞ are shown. As seen in the figures, when the real static permittivities ϵ_s become larger, the magnitudes of the real and imaginary parts of the poles become smaller suggesting that the amplitude decay factors become smaller.

The pole trajectories for the air-backed, perpendicular polarization case with the same conditions are shown in Figures 5.4-5.6. The air-backed case also shows the same behavior as the conductor-backed case. The existence condition for the real poles and the algorithm for finding such poles are examined next.

Let us assume a complex frequency s to be negative real and denote its

magnitude as x, where $x > 0$. Then, if $s > s_1$, from (5.6), (5.9) and (5.10)

$$s\tau(s) = j\frac{2\Delta}{c}\chi\frac{\sqrt{x(x+s_1)(x+s_3)}}{\sqrt{-(x+s_2)}},$$

and the reflection coefficient becomes

$$\Gamma_\perp(s) = \frac{j\cos\theta_i\sqrt{-x(x+s_2)} - \chi\sqrt{(x+s_1)(x+s_3)}}{j\cos\theta_i\sqrt{-x(x+s_2)} + \chi\sqrt{(x+s_1)(x+s_3)}}$$

for perpendicular polarization, and

$$\Gamma_\parallel(s) = \frac{j\epsilon_0\chi\sqrt{-x(x+s_1)(x+s_2)(x+s_3)} - \cos\theta_i[x(x\epsilon_\infty + s_2\epsilon_s) - \sigma(x+s_2)]}{j\epsilon_0\chi\sqrt{-x(x+s_1)(x+s_2)(x+s_3)} + \cos\theta_i[x(x\epsilon_\infty + s_2\epsilon_s) - \sigma(x+s_2)]}$$

for parallel polarization.

As seen from the above equations, the magnitudes of both $e^{-s\tau(s)}$ and $\Gamma(s)$ are 1. As a result, the real parts of (5.17) and (5.18) become 0, i.e., $\ln\left|\Gamma(s)e^{-s\tau(s)}\right| = 0$ and $\ln\left|\Gamma(s)^2e^{-s\tau(s)}\right| = 0$. Therefore, the poles need to satisfy only the imaginary part of (5.17) or (5.18), i.e., $\arg\left[\Gamma(s)e^{-s\tau(s)}\right] = 0$ or $\arg\left[\Gamma(s)^2e^{-s\tau(s)}\right] = 0$ for the conductor-backed and the air-backed case respectively. Here, if we denote $-s\tau(s)$ as ϕ_1 and $\arg[\Gamma(s)]$ or $\arg[\Gamma^2(s)]$ as ϕ_2 for the conductor-backed or the air-backed case respectively, the poles need to satisfy

$$\phi_1 + \phi_2 + 2n\pi = 0. \quad n = 0, 1, 2, \cdots \tag{5.19}$$

Here, only the positive sign in front of n is necessary, since ϕ_1 is always negative, when $s > s_1$ and $-\pi < \phi_2 < \pi$. The above equation, which we call the *characteristic function*, can be solved by any 1-D root search algorithm, such as the secant method. Again, it is very important to note that (5.19) does not always have solutions, and that the number of solutions is dependent upon the conductivity,

permittivities and incident angle.

If $s_2 < s < s_1$, i.e., $-s_1 < x < -s_2$,

$$s\tau(s) = -\frac{2\Delta}{c}\chi\sqrt{\frac{x(x+s_1)(x+s_3)}{x+s_2}},$$

and the reflection coefficient becomes

$$\Gamma_\perp(s) = \frac{\cos\theta_i\sqrt{-x(x+s_2)} - \chi\sqrt{-(x+s_1)(x+s_3)}}{\cos\theta_i\sqrt{-x(x+s_2)} + \chi\sqrt{-(x+s_1)(x+s_3)}}$$

for perpendicular polarization, and

$$\Gamma_\parallel(s) = \frac{-\epsilon_0\chi\sqrt{x(x+s_1)(x+s_2)(x+s_3)} - \cos\theta_i[x(x\epsilon_\infty + s_2\epsilon_s) - \sigma(x+s_2)]}{-\epsilon_0\chi\sqrt{x(x+s_1)(x+s_2)(x+s_3)} + \cos\theta_i[x(x\epsilon_\infty + s_2\epsilon_s) - \sigma(x+s_2)]}$$

for parallel polarization.

As seen from the equations, when $s_2 < s < s_1$, $s\tau(s)$ becomes negative real causing $e^{-s\tau(s)}$ to be greater than 1, and $\Gamma(s)$ becomes pure real. Therefore, the imaginary parts of (5.17) is zero as long as $\Gamma(s)$ is positive, whereas that of (5.18) is always zero regardless of the sign of $\Gamma(s)$. When the imaginary parts of (5.17) and (5.18) are zero, the poles only need to satisfy the real parts of the equations, i.e. $\ln\left|\Gamma(s)e^{-s\tau(s)}\right| = 0$ and $\ln\left|\Gamma(s)^2e^{-s\tau(s)}\right| = 0$ for the conductor-backed and the air-backed case respectively.

The cases where $s_3 < s < s_2$ and $s < s_3$ are analogous to the cases where $s_1 < s < 0$ and $s_2 < s < s_1$ respectively. Figure 5.7 and Figure 5.8 show the amplitudes of the interfacial reflection coefficients for the perpendicular and the parallel polarization case, where $\epsilon_s = 5.0\epsilon_0$, $\epsilon_\infty = 3.0\epsilon_0$ and $\sigma = 1.0$ S/m. From the figures, it can be observed that $\Gamma(s)$ follows the above discussion.

Finally, it should be emphasized that the real poles in the region where $s > s_1$ dominate the other real poles due to their relatively smaller magnitudes. The

greatest care should be given to calculating these poles.

5.3 Evaluation of $r(t)$

Since all poles and branch points lie in the left half plane including the imaginary axis, the region of convergence is the right half plane. Therefore, the Bromwich path is put in the right half plane and the Laplace inversion integral is evaluated by contour integration. The evaluation is accomplished in two different time intervals, corresponding to the early-time period and the late-time period. The beginning of the late-time period is $\tau_0 = \frac{2\Delta}{c}\chi$. It should be emphasized that, unlike with the previous cases, τ_0 does not represents the two-way transit time of the wave inside the dielectric.

In this section, the evaluation will be done for the conductor-backed case. The air-backed case follows the same procedure giving similar results; for the details refer to Chapter 4.

5.3.1 Case I: $t > \tau_0$

When $t > \tau_0$, the integration contour is closed in the left half plane as shown in Figure 5.9. Inside the contour, the branch cuts lie from 0 to s_1 and from s_2 to s_3, and there are corresponding closed paths enclosing the branch cuts. Note that the possible real poles are not shown in the figure. We denote the outer integration contour which includes the Bromwich path as C_0 and the closed paths which enclose the branch cuts as C_1, such that

$$\begin{aligned} C_0 &= B_r + \Gamma_\infty + L_1 + L_2, \\ C_1 &= \gamma_1 + \gamma_2 + \gamma_3 + \gamma_4 + l_1 + l_2 + l_3 + l_4. \end{aligned}$$

Then, by Cauchy's residue theorem,

$$\int_{C_0+C_1} R(s)e^{st}\,\mathrm{d}s = j2\pi \sum Res[R(s)e^{st}, poles] \tag{5.20}$$

Therefore, if the integral contribution from each path is known, the impulse response $r(t)$ can be determined.

The contribution from Γ_∞

On Γ_∞, from (5.6),

$$\begin{aligned} \mathrm{Re}\{s\tau(s)\} &= \mathrm{Re}\left\{ \lim_{\mathrm{Re}\{s\}\to-\infty} \frac{2\Delta}{c}\chi \frac{\sqrt{s}\sqrt{s-s_1}\sqrt{s-s_3}}{\sqrt{s-s_2}} \right\} \\ &\simeq s\frac{2\Delta}{c}\chi = s\tau_0 \end{aligned}$$

If we let $t_1 = t - \tau_0$, which is positive since we are evaluating the integral when $t > \tau_0$, then

$$\int_{\Gamma_\infty} R(s)e^{st}\,\mathrm{d}s = \int_{\Gamma_\infty} \frac{\Gamma(s)e^{s\tau_0} - e^{-s\tau(s)}e^{s\tau_0}}{1-\Gamma(s)e^{-s\tau(s)}} e^{st_1}\,\mathrm{d}s = \int_{\Gamma_\infty} f(s)e^{st_1}\,\mathrm{d}s$$

Since $f(s) \to 0$ on Γ_∞, by *Jordan's Lemma* [20], [21],

$$\int_{\Gamma_\infty} R(s)e^{st}\,\mathrm{d}s = 0 \tag{5.21}$$

The contribution from L_1 and L_2

As seen in the previous chapters, for L_1 and L_2, the same theorem [14] can be used to apply *Jordan's Lemma.* As a result, it can be shown that

$$\int_{L_1,L_2} R(s)e^{st}\,\mathrm{d}s = 0 \tag{5.22}$$

The contribution from C_1

The segments of the contour C_1 enclosing the branch cut can be divided into three groups. The first group consists of γ_1, γ_2, γ_3 and γ_4 that enclose the branch points s_3, s_2, s_1 and 0 respectively. The second group consists of the straight lines immediately below and above the branch cut, and those are designated l_1, l_2, l_3 and l_4. The last group consists of the paths that enclose the real poles on the branch cut which are not shown in Figure 5.9. For the third group, refer to the previous chapters. The first two groups will be examined separately.

Denote the radius of γ_1 as r, and let θ to be the angle measured counterclockwise from the real axis to the point on γ_1. Then, any point on γ_1 can be represented as

$$s = s_0 + re^{j\theta}.$$

The reflection coefficient on γ_1 with $r \to 0$, i.e. $s \to s_0$, becomes -1 for parallel polarization and 1 for perpendicular polarization. Then,

$$R(s)e^{st} = \frac{\Gamma(s) - e^{-s\tau(s)}}{1 - \Gamma(s)e^{-s\tau(s)}}e^{st} = \begin{cases} e^{st} & , \quad \perp \text{ - pol} \\ -e^{st} & , \quad \| \text{ - pol} \end{cases}$$

and

$$\left|R(s)e^{st}\right| \leq e^{(s_0+r)t}.$$

Therefore,

$$\left|\int_{\gamma_1} R(s)e^{st}\,\mathrm{d}s\right| \leq 2\pi\, r\, e^{(s_0+r)t} \to 0, \quad (r \to 0).$$

As a result,

$$\int_{\gamma_1} R(s)e^{st}\,\mathrm{d}s = 0. \tag{5.23}$$

Similarly, it can be shown

$$\int_{\gamma_2,\gamma_3,\gamma_4} R(s)e^{st}\,ds = 0. \tag{5.24}$$

For the second group, it is necessary to determine $\Gamma(s)$ and $s\tau(s)$ along a path immediately above the branch cut, which we denote as B^+, and immediately below the branch cut, which we denote as B^-. Also, if we let $Z(s)$ on B^+ be denoted as Z^+, and Z(s) on B^- as Z^-, using (5.7) and (5.8), it can be shown that

$$Z^+ = -Z^-. \tag{5.25}$$

Since,

$$\begin{aligned} R(s) &= \frac{\Gamma(s) - e^{-s\tau(s)}}{1 - \Gamma(s)e^{-s\tau(s)}} \\ &= \frac{[Z(s) - Z_0]e^{\frac{1}{2}s\tau(s)} - [Z(s) + Z_0]e^{-\frac{1}{2}s\tau(s)}}{[Z(s) + Z_0]e^{\frac{1}{2}s\tau(s)} - [Z(s) - Z_0]e^{-\frac{1}{2}s\tau(s)}}, \end{aligned}$$

we have,

$$\begin{aligned} R(s)|_{B^+} &= \frac{[Z^+ - Z_0]e^{j\phi} - [Z^+ + Z_0]e^{-j\phi}}{[Z^+ + Z_0]e^{j\phi} - [Z^+ - Z_0]e^{-j\phi}} \\ &= \frac{jZ^+ \sin\phi - Z_0 \cos\phi}{jZ^+ \sin\phi + Z_0 \cos\phi} \end{aligned}$$

where $j\phi = \frac{1}{2}s\tau(s)$, and

$$\begin{aligned} R(s)|_{B^-} &= \frac{[Z^- - Z_0]e^{-j\phi} - [Z^- + Z_0]e^{j\phi}}{[Z^- + Z_0]e^{-j\phi} - [Z^- - Z_0]e^{j\phi}} \\ &= \frac{-jZ^- \sin\phi - Z_0 \cos\phi}{-jZ^- \sin\phi + Z_0 \cos\phi} \end{aligned}$$

Therefore, by (5.25)

$$R(s)|_{B^+} = R(s)|_{B^-}.$$

As a result,

$$\int_{l_1+l_2} R(s)|_{B^+} e^{st}\,\mathrm{d}s + \int_{l_3+l_4} R(s)|_{B^-} e^{st}\,\mathrm{d}s = 0 \tag{5.26}$$

The integral contributions from the third group and the other complex poles can be determined by calculating the residues of $R(s)e^{st}$ at the poles. It is found that all of the poles of $R(s)$ are of first order and thus

$$Res\left[R(s)e^{st},\, poles\right]|_{s=s_k} = \lim_{s\to s_k}(s-s_k)\left[\frac{\Gamma(s)-e^{-s\tau(s)}}{1-\Gamma(s)e^{-s\tau(s)}}e^{st}\right] = A_k e^{s_k t}, \tag{5.27}$$

where

$$A_k = -\frac{\Gamma(s_k)-e^{-s_k\tau(s_k)}}{\frac{d}{ds}\left[\Gamma(s)e^{-s\tau(s)}\right]|_{s=s_k}}$$

is the complex natural mode amplitude. In this chapter, A_k is calculated by using the numerically obtained Jacobian at the pole locations.

Collecting the results from (5.21)-(5.27), the impulse response $r(t)$ becomes

$$r(t) = \frac{1}{j2\pi}\int_{B_r} R(s)e^{st}\,\mathrm{d}s = \sum A_k e^{s_k t}, \quad t > \tau_0\,, \tag{5.28}$$

and thus the late-time period is a pure natural resonance series, and contains no branch-cut contribution.

5.3.2 Case II: $t < \tau_0$

For $t < \tau_0$, $r(t)$ is found by computing the inverse Laplace transform of $R(s) = \Gamma(s) + \overline{R}(s)$, where

$$\overline{R}(s) = R(s) - \Gamma(s) = \left[\Gamma^2(s) - 1\right]\frac{e^{-s\tau(s)}}{1-\Gamma(s)e^{-s\tau(s)}}.$$

Then

$$\overline{R}(t) = \mathcal{L}^{-1}\left\{\overline{R}(s)\right\} = \frac{1}{j2\pi}\int_{Br}\left[\Gamma^2(s)-1\right]\frac{e^{-s\tau(s)}}{1-\Gamma(s)e^{-s\tau(s)}}e^{st}ds.$$

To compute this integral, the integration contour is closed in the right half plane, as shown in Figure 5.10. On Γ_∞, from (5.6),

$$\begin{aligned} \mathrm{Re}\{s\tau(s)\} &= \mathrm{Re}\left\{ \lim_{\mathrm{Re}\{s\}\to\infty} \frac{2\Delta}{c}\chi \frac{\sqrt{s}\sqrt{s-s_1}\sqrt{s-s_3}}{\sqrt{s-s_2}} \right\} \\ &\simeq s\frac{2\Delta}{c}\chi = s\tau_0 \end{aligned}$$

If we let $t_1 = t - \tau_0$, which is negative since we are evaluating the integral when $t < \tau_0$, then

$$\int_{\Gamma_\infty} \overline{R}(s)e^{st}\,\mathrm{d}s = \int_{\Gamma_\infty} \left[\Gamma^2(s) - 1\right] \frac{e^{-s\tau(s)}e^{s\tau_0}}{1 - \Gamma(s)e^{-s\tau(s)}} e^{st_1}\,\mathrm{d}s = \int_{\Gamma_\infty} f(s)e^{st_1}\,\mathrm{d}s$$

Here, it is not possible to apply *Jordan's Lemma* directly, since $f(s)$ does not approach zero over the entire contour Γ_∞. However, if we use the theorem introduced in the previous chapters, it can be argued that

$$\int_{\Gamma_\infty} \overline{R}(s)e^{st}\,\mathrm{d}s = 0$$

The inverse transform of $\Gamma(s)$, denoted as $\Gamma(t)$, is the interfacial reflection coefficient and can be obtained numerically. Note that we are interested in the late-time responses, rather than the early-time specular reflections. As a result, when $t < \tau_0$, $r(t)$ becomes

$$r(t) = \Gamma(t), \quad t < \tau_0. \tag{5.29}$$

Combining the results (5.28) and (5.29), the impulse response $r(t)$ is

$$r(t) = \begin{cases} \sum A_k e^{s_k t}, & t > \tau_0 \\ \Gamma(t), & t < \tau_0. \end{cases} \tag{5.30}$$

5.4 Results

As with the frequency-independent parameter cases, it has been shown analytically with the Debye material that the early-time response is a specular reflection from the interface between free-space and the dielectric slab, and the late-time response is a pure sum of damped sinusoids. In order to verify these results, the natural mode series is compared to the direct IFFT using the same input waveform used for the previous cases. Figures 5.11-5.16 show the transient responses calculated by the natural mode series and the IFFT. In addition, the IFFT of the interfacial reflection coefficients $\Gamma(s)$ are also shown in order to explain the early-time behavior. The natural resonant frequencies of the corresponding cases are shown in Table 5.1-5.6.

Figure 5.11 and Figure 5.14 show the responses from the pure water at room temperature from the conductor-backed and the air-backed case respectively, where $\epsilon_s = 78.3\epsilon_0$, $\epsilon_\infty = 5.0\epsilon_0$, $\xi = 9.6 \times 10^{-12}$ sec, $\sigma = 0$ S/m, $\theta_i = 0°$ and $\Delta = 2$ cm. For these cases, the beginning of the impulse response late-time is $\tau_0 = 0.291$ ns. As shown in figures, during the early-time period, before τ_0, the IFFT of $R(\omega)F(\omega)$ (where $F(\omega)$ is the spectrum of the input waveform) matches well with the IFFT of $\Gamma(\omega)F(\omega)$, which is the specular reflection from the interface. During the late-time, the IFFT of $R(\omega)F(\omega)$ matches well with the natural mode series. Note that, even though $\tau_0 = 0.291$ ns, the first amplitude peak during the late-time occurs at about 1.3 ns due to the high real static permittivity ϵ_s. Again, it should be noted that when $t < \tau_0$ the response from the natural mode series does not have any meaning; i.e., the natural mode series is valid only when $t > \tau_0$, the late-time period. Since the frequency band of the input waveform is roughly $0 - 20$ GHz, the first 7 natural modes, which are shown in Table 5.1 and Table 5.4, are sufficient to represent the late-time reflected field.

Figure 5.12 and Figure 5.15 show the responses from the same material except

for nonzero conductivity $\sigma = 0.1$, and with the incidence angle $\theta_i = 30°$ for perpendicular polarization. Figure 5.13 and Figure 5.16 represent the responses obtained with the same condition except for a higher conductivity $\sigma = 0.5$ and for parallel polarization.

Comparing Figures 5.12 and 5.14 to Figures 5.13 and 5.16, due to the relatively higher conductivity in the Figure 5.13 and 5.16 cases, relatively smaller late-time responses are observed. The corresponding natural resonance frequencies for these cases are shown in Tables 5.3 and 5.6. Note that there is one real pole for each air-backed case.

Table 5.1: Poles and corresponding complex natural mode amplitudes (A_k), conductor-backed case, normal incidence ($\epsilon_s = 78.3\epsilon_0$, $\epsilon_\infty = 5.0\epsilon_0$, $\xi = 9.6 \times 10^{-12}$ sec, $\Delta = 2$ cm, $\theta_i = 0°$, $\sigma = 0.0$ S/m)

	Pole Amplitude		Natural Mode Amplitude	
	Real Part	Imaginary Part	Real Part	Imaginary Part
mode 0	$-.22382 \times 10^9$	$.26557 \times 10^{10}$	$.38655 \times 10^9$	$.13994 \times 10^8$
mode 1	$-.47802 \times 10^9$	$.79638 \times 10^{10}$	$.38497 \times 10^9$	$.41972 \times 10^8$
mode 2	$-.98686 \times 10^9$	$.13262 \times 10^{11}$	$.38180 \times 10^9$	$.69914 \times 10^8$
mode 3	$-.17512 \times 10^{10}$	$.18543 \times 10^{11}$	$.37703 \times 10^9$	$.97797 \times 10^8$
mode 4	$-.27725 \times 10^{10}$	$.23801 \times 10^{11}$	$.37063 \times 10^9$	$.12560 \times 10^9$
mode 5	$-.40525 \times 10^{10}$	$.29028 \times 10^{11}$	$.36264 \times 10^9$	$.15329 \times 10^9$
mode 6	$-.55934 \times 10^{10}$	$.34217 \times 10^{12}$	$.35291 \times 10^9$	$.18084 \times 10^9$

Table 5.2: Poles and corresponding complex natural mode amplitudes (A_k), conductor-backed case, $\perp$ polarization ($\epsilon_s = 78.3\epsilon_0$, $\epsilon_\infty = 5.0\epsilon_0$, $\xi = 9.6 \times 10^{-12}$ sec, $\Delta = 2$ cm, $\theta_i = 30°$, $\sigma = 0.1$ S/m)

	Pole Amplitude		Natural Mode Amplitude	
	Real Part	Imaginary Part	Real Part	Imaginary Part
mode 0	$-.27087 \times 10^9$	$.26527 \times 10^{10}$	$.33517 \times 10^9$	$.21358 \times 10^8$
mode 1	$-.52625 \times 10^9$	$.79695 \times 10^{10}$	$.33277 \times 10^9$	$.39472 \times 10^8$
mode 2	$-.10379 \times 10^{10}$	$.13273 \times 10^{11}$	$.32992 \times 10^9$	$.62452 \times 10^8$
mode 3	$-.18065 \times 10^{10}$	$.18559 \times 10^{11}$	$.32573 \times 10^9$	$.86082 \times 10^8$
mode 4	$-.28333 \times 10^{10}$	$.23820 \times 10^{11}$	$.32013 \times 10^9$	$.10987 \times 10^9$
mode 5	$-.41202 \times 10^{10}$	$.29050 \times 10^{11}$	$.31316 \times 10^9$	$.13366 \times 10^9$
mode 6	$-.56692 \times 10^{10}$	$.34240 \times 10^{11}$	$.30466 \times 10^9$	$.15738 \times 10^9$

Table 5.3: Poles and corresponding complex natural mode amplitudes (A_k), conductor-backed case, $\|$ polarization ($\epsilon_s = 78.3\epsilon_0$, $\epsilon_\infty = 5.0\epsilon_0$, $\xi = 9.6 \times 10^{-12}$ sec, $\Delta = 2$ cm, $\theta_i = 30°$, $\sigma = 0.5$ S/m)

	Pole Amplitude		Natural Mode Amplitude	
	Real Part	Imaginary Part	Real Part	Imaginary Part
mode 0	$-.61336 \times 10^9$	$.25908 \times 10^{10}$	$.45231 \times 10^9$	$.79609 \times 10^8$
mode 1	$-.86535 \times 10^9$	$.79163 \times 10^{10}$	$.44129 \times 10^9$	$.69074 \times 10^8$
mode 2	$-.13741 \times 10^{10}$	$.13202 \times 10^{11}$	$.43689 \times 10^9$	$.92938 \times 10^8$
mode 3	$-.21385 \times 10^{10}$	$.18466 \times 10^{11}$	$.43112 \times 10^9$	$.12148 \times 10^9$
mode 4	$-.31597 \times 10^{10}$	$.23704 \times 10^{11}$	$.42357 \times 10^9$	$.15149 \times 10^9$
mode 5	$-.44396 \times 10^{10}$	$.28911 \times 10^{11}$	$.41418 \times 10^9$	$.18208 \times 10^9$
mode 6	$-.59800 \times 10^{10}$	$.34078 \times 10^{11}$	$.40280 \times 10^9$	$.21285 \times 10^9$

Table 5.4: Poles and corresponding complex natural mode amplitudes (A_k), air-backed case, normal incidence ($\epsilon_s = 78.3\epsilon_0$, $\epsilon_\infty = 5.0\epsilon_0$, $\xi = 9.6 \times 10^{-12}$ sec, $\Delta = 2$ cm, $\theta_i = 0°$, $\sigma = 0.0$ S/m)

	Pole Amplitude		Natural Mode Amplitude	
	Real Part	Imaginary Part	Real Part	Imaginary Part
mode 0	$-.51014 \times 10^9$	$.52968 \times 10^{10}$	$.38462 \times 10^9$	$.27874 \times 10^8$
mode 1	$-.89043 \times 10^9$	$.10587 \times 10^{11}$	$.38225 \times 10^9$	$.55725 \times 10^8$
mode 2	$-.15250 \times 10^{10}$	$.15864 \times 10^{11}$	$.37830 \times 10^9$	$.83529 \times 10^8$
mode 3	$-.24149 \times 10^{10}$	$.21120 \times 10^{11}$	$.37274 \times 10^9$	$.11126 \times 10^9$
mode 4	$-.35617 \times 10^{10}$	$.26350 \times 10^{11}$	$.36554 \times 10^9$	$.13889 \times 10^9$
mode 5	$-.49676 \times 10^{10}$	$.31545 \times 10^{11}$	$.35676 \times 10^9$	$.16641 \times 10^9$
mode 6	$-.66349 \times 10^{10}$	$.36699 \times 10^{12}$	$.34621 \times 10^9$	$.19376 \times 10^9$
real	$-.38345 \times 10^9$	0.0	$.38540 \times 10^9$	0.0

Table 5.5: Poles and corresponding complex natural mode amplitudes (A_k), air-backed case, $\perp$ polarization ($\epsilon_s = 78.3\epsilon_0$, $\epsilon_\infty = 5.0\epsilon_0$, $\xi = 9.6 \times 10^{-12}$ sec, $\Delta = 2$ cm, $\theta_i = 30°$, $\sigma = 0.1$ S/m)

	Pole Amplitude		Natural Mode Amplitude	
	Real Part	Imaginary Part	Real Part	Imaginary Part
mode 0	$-.53216 \times 10^9$	$.15660 \times 10^{10}$	$.33307 \times 10^9$	$.28773 \times 10^8$
mode 1	$-.91452 \times 10^9$	$.10598 \times 10^{11}$	$.33058 \times 10^9$	$.50640 \times 10^8$
mode 2	$-.15528 \times 10^{10}$	$.15882 \times 10^{11}$	$.32704 \times 10^9$	$.73977 \times 10^8$
mode 3	$-.24479 \times 10^{10}$	$.21145 \times 10^{11}$	$.32215 \times 10^9$	$.97629 \times 10^8$
mode 4	$-.36014 \times 10^{10}$	$.26379 \times 10^{11}$	$.31585 \times 10^9$	$.12134 \times 10^9$
mode 5	$-.50153 \times 10^{10}$	$.31579 \times 10^{11}$	$.30818 \times 10^9$	$.14503 \times 10^9$
mode 6	$-.66918 \times 10^{10}$	$.36735 \times 10^{11}$	$.29896 \times 10^9$	$.16859 \times 10^9$
real	$-.47724 \times 10^9$	0.0	$.33412 \times 10^9$	0.0

Table 5.6: Poles and corresponding complex natural mode amplitudes (A_k), air-backed case, $\|$ polarization ($\epsilon_s = 78.3\epsilon_0$, $\epsilon_\infty = 5.0\epsilon_0$, $\xi = 9.6 \times 10^{-12}$ sec, $\Delta = 2$ cm, $\theta_i = 30°$, $\sigma = 0.5$ S/m)

	Pole Amplitude		Natural Mode Amplitude	
	Real Part	Imaginary Part	Real Part	Imaginary Part
mode 0	$-.92647 \times 10^9$	$.52329 \times 10^{10}$	$.44466 \times 10^9$	$.63070 \times 10^8$
mode 1	$-.13048 \times 10^{10}$	$.10523 \times 10^{11}$	$.43808 \times 10^9$	$.79647 \times 10^8$
mode 2	$-.19388 \times 10^{10}$	$.15784 \times 10^{11}$	$.43277 \times 10^9$	$.10647 \times 10^9$
mode 3	$-.28282 \times 10^{10}$	$.21022 \times 10^{11}$	$.42603 \times 10^9$	$.13578 \times 10^9$
mode 4	$-.39743 \times 10^{10}$	$.26230 \times 10^{11}$	$.41752 \times 10^9$	$.16599 \times 10^9$
mode 5	$-.53792 \times 10^{10}$	$.31403 \times 10^{11}$	$.40719 \times 10^9$	$.19656 \times 10^9$
mode 6	$-.70450 \times 10^{10}$	$.36532 \times 10^{11}$	$.39484 \times 10^9$	$.22720 \times 10^9$
real	$-.11590 \times 10^{10}$	0.0	$.44881 \times 10^9$	0.0

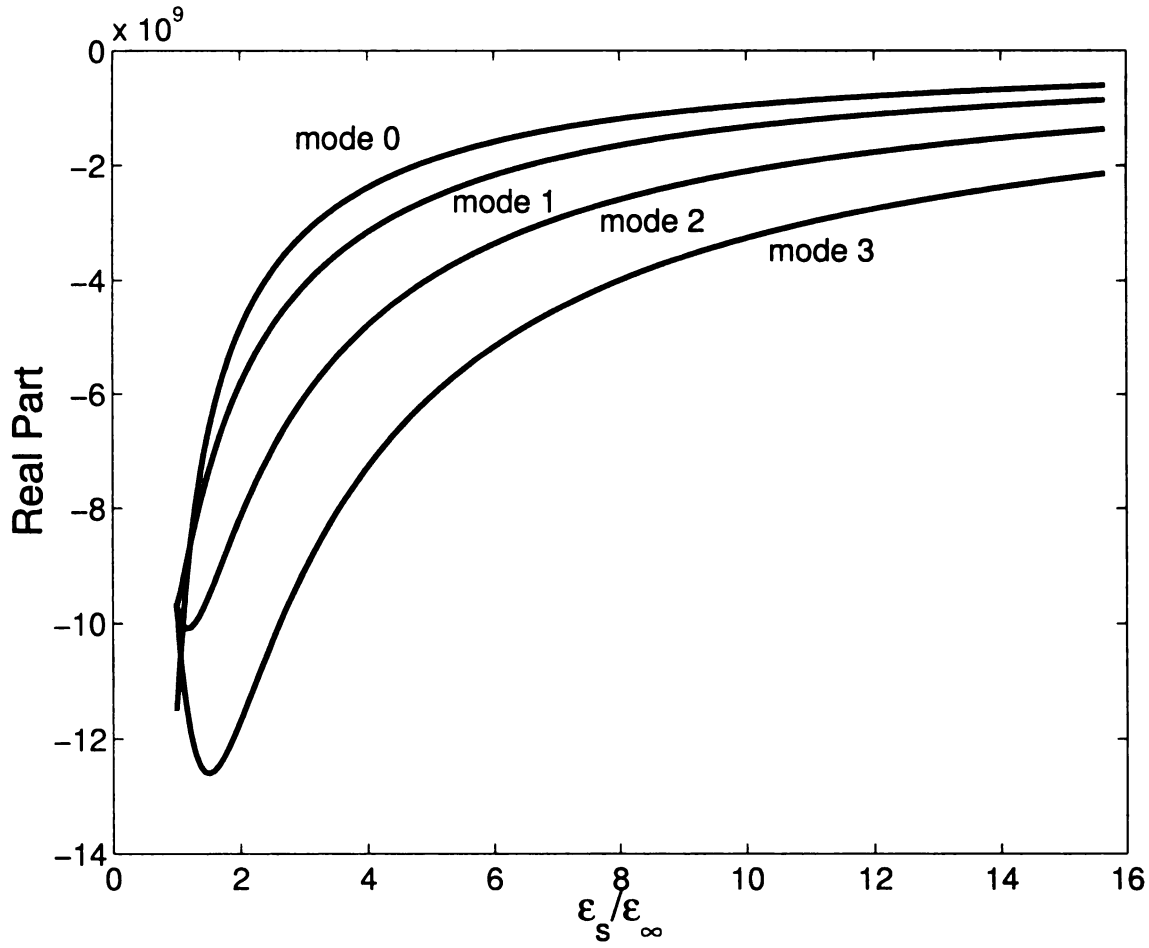

Figure 5.1: The amplitude of the real parts of poles vs. the ratio of ϵ_s to ϵ_∞, $\|$ polarization ($\epsilon_s = 5.0\epsilon_0 \rightarrow 78.3\epsilon_0$, $\epsilon_\infty = 5.0\epsilon_0$, $\xi = 9.6 \times 10^{-12}$ sec, $\Delta = 2$ cm, $\theta_i = 30°$, $\sigma = 0.5$ S/m).

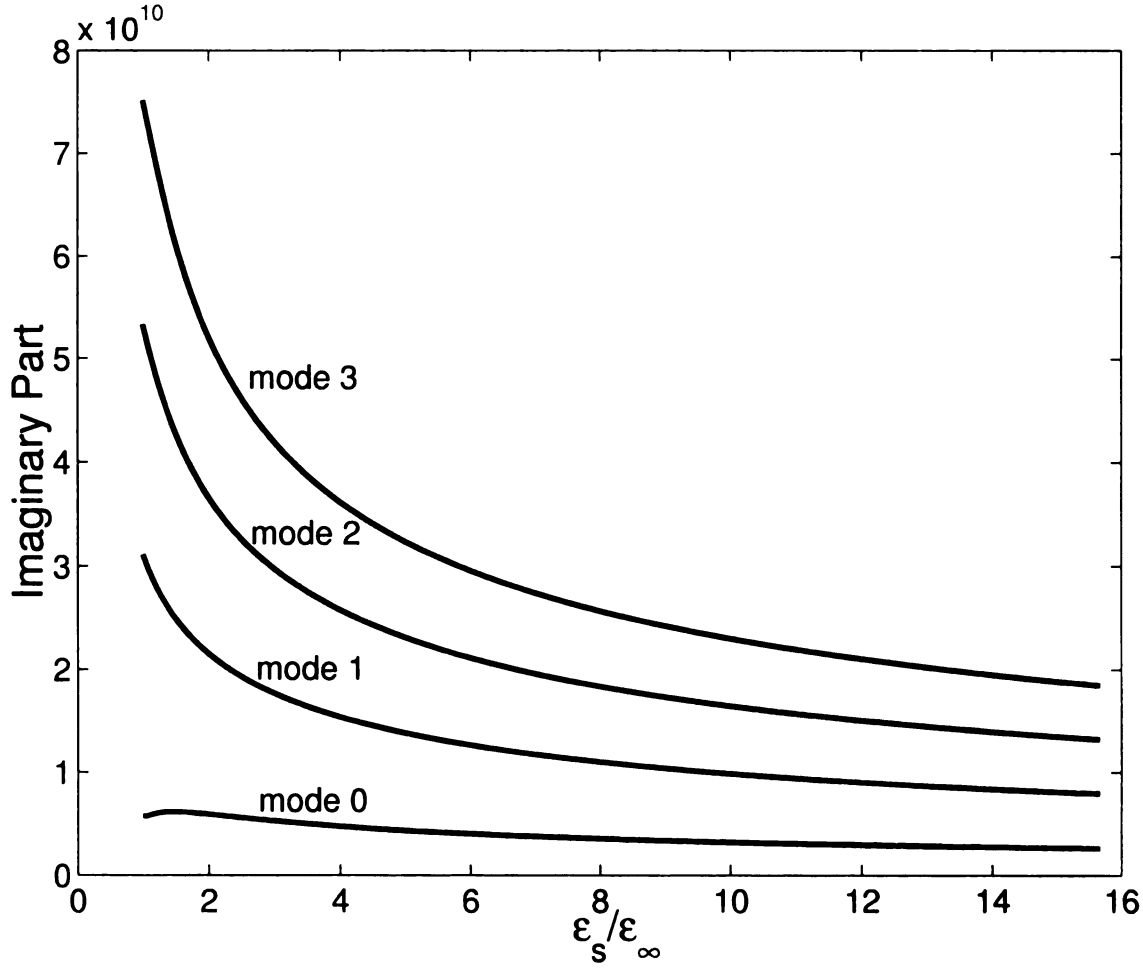

Figure 5.2: The amplitude of the imaginary parts of poles vs. the ratio of ϵ_s to ϵ_∞, $\|$ polarization ($\epsilon_s = 5.0\epsilon_0 \rightarrow 78.3\epsilon_0$, $\epsilon_\infty = 5.0\epsilon_0$, $\xi = 9.6 \times 10^{-12}$ sec, $\Delta = 2$ cm, $\theta_i = 30°$, $\sigma = 0.5$ S/m).

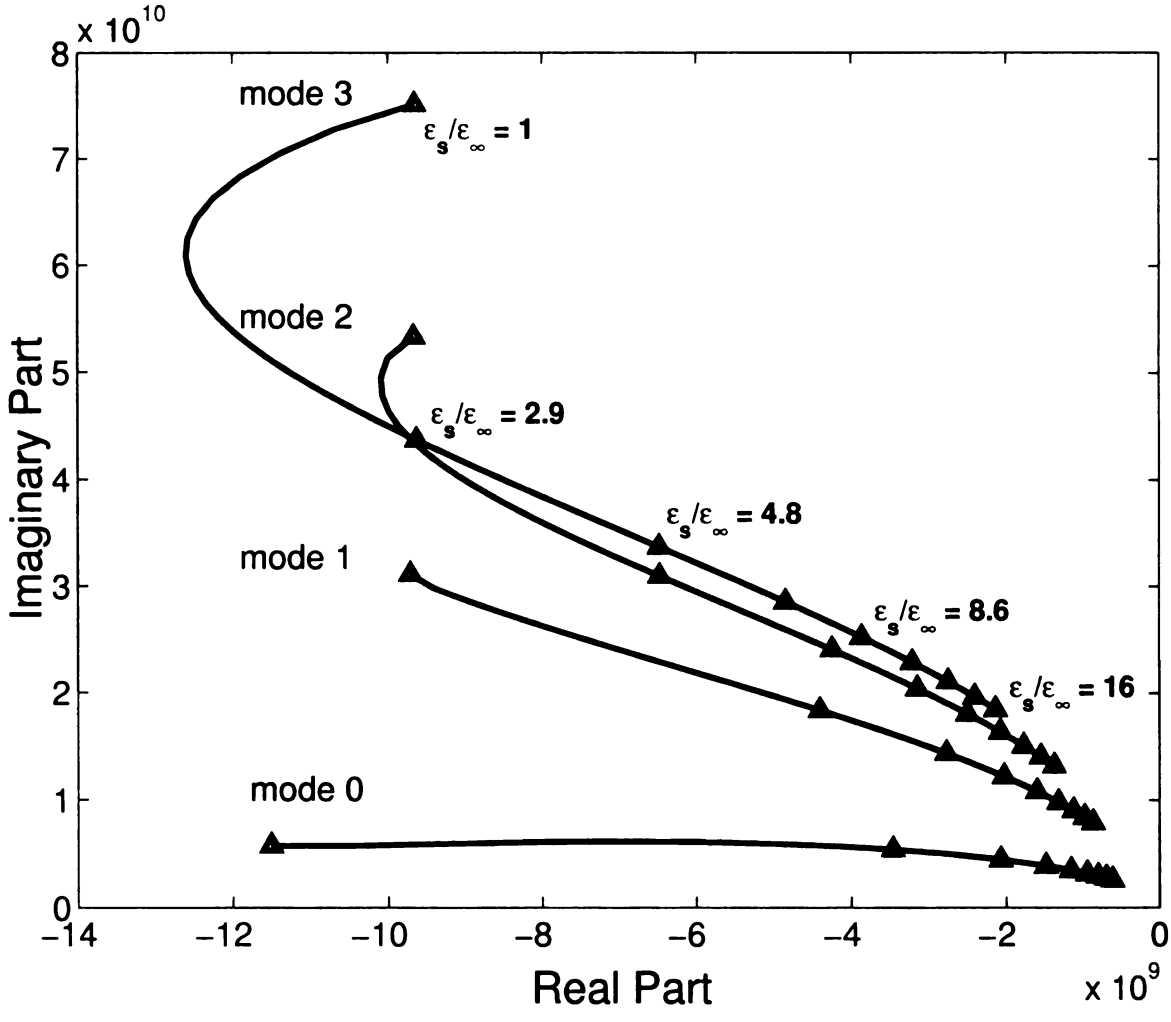

Figure 5.3: Pole trajectories of the reflection coefficient, $\|$ polarization ($\epsilon_s = 5.0\epsilon_0 \rightarrow 78.3\epsilon_0$, $\epsilon_\infty = 5.0\epsilon_0$, $\xi = 9.6 \times 10^{-12}$ sec, $\Delta = 2$ cm, $\theta_i = 30°$, $\sigma = 0.5$ S/m).

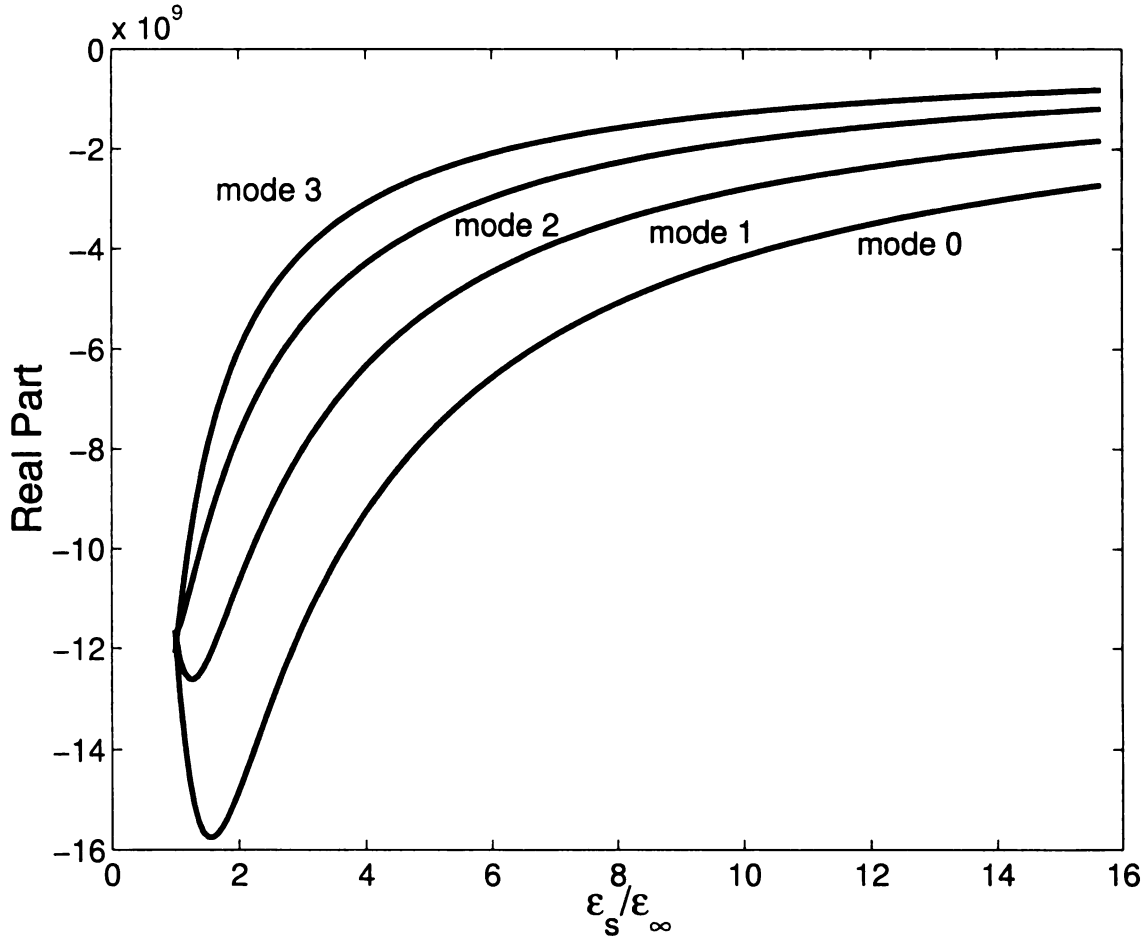

Figure 5.4: The amplitude of the real parts of poles vs. the ratio of ϵ_s to ϵ_∞, $\perp$ polarization ($\epsilon_s = 5.0\epsilon_0 \rightarrow 78.3\epsilon_0$, $\epsilon_\infty = 5.0\epsilon_0$, $\xi = 9.6 \times 10^{-12}$ sec, $\Delta = 2$ cm, $\theta_i = 30°$, $\sigma = 0.5$ S/m).

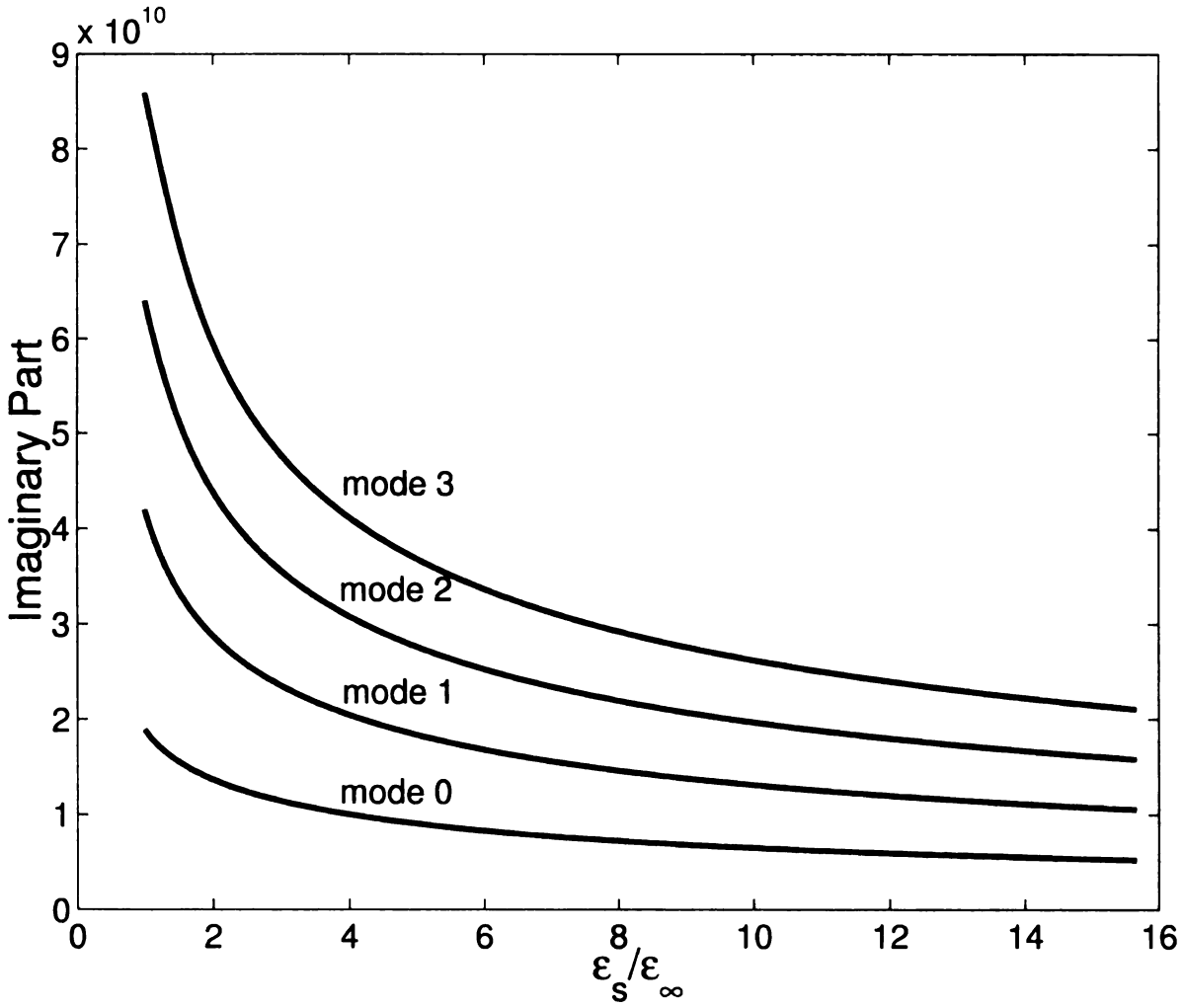

Figure 5.5: The amplitude of the imaginary parts of poles vs. the ratio of ϵ_s to ϵ_∞, $\perp$ polarization ($\epsilon_s = 5.0\epsilon_0 \rightarrow 78.3\epsilon_0$, $\epsilon_\infty = 5.0\epsilon_0$, $\xi = 9.6 \times 10^{-12}$ sec, $\Delta = 2$ cm, $\theta_i = 30°$, $\sigma = 0.5$ S/m).

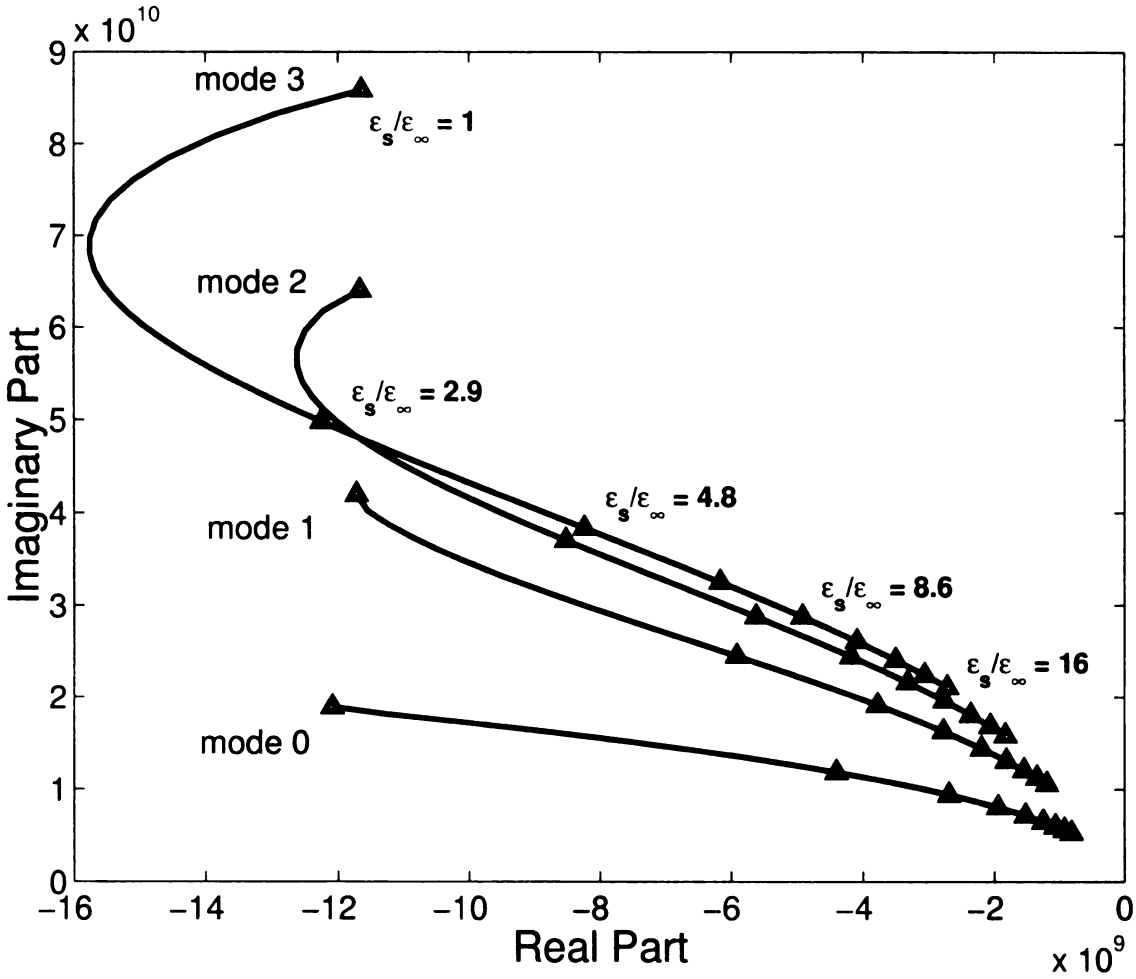

Figure 5.6: Pole trajectories of the reflection coefficient, $\perp$ polarization ($\epsilon_s = 5.0\epsilon_0 \rightarrow 78.3\epsilon_0$, $\epsilon_\infty = 5.0\epsilon_0$, $\xi = 9.6 \times 10^{-12}$ sec, $\Delta = 2$ cm, $\theta_i = 30°$, $\sigma = 0.5$ S/m).

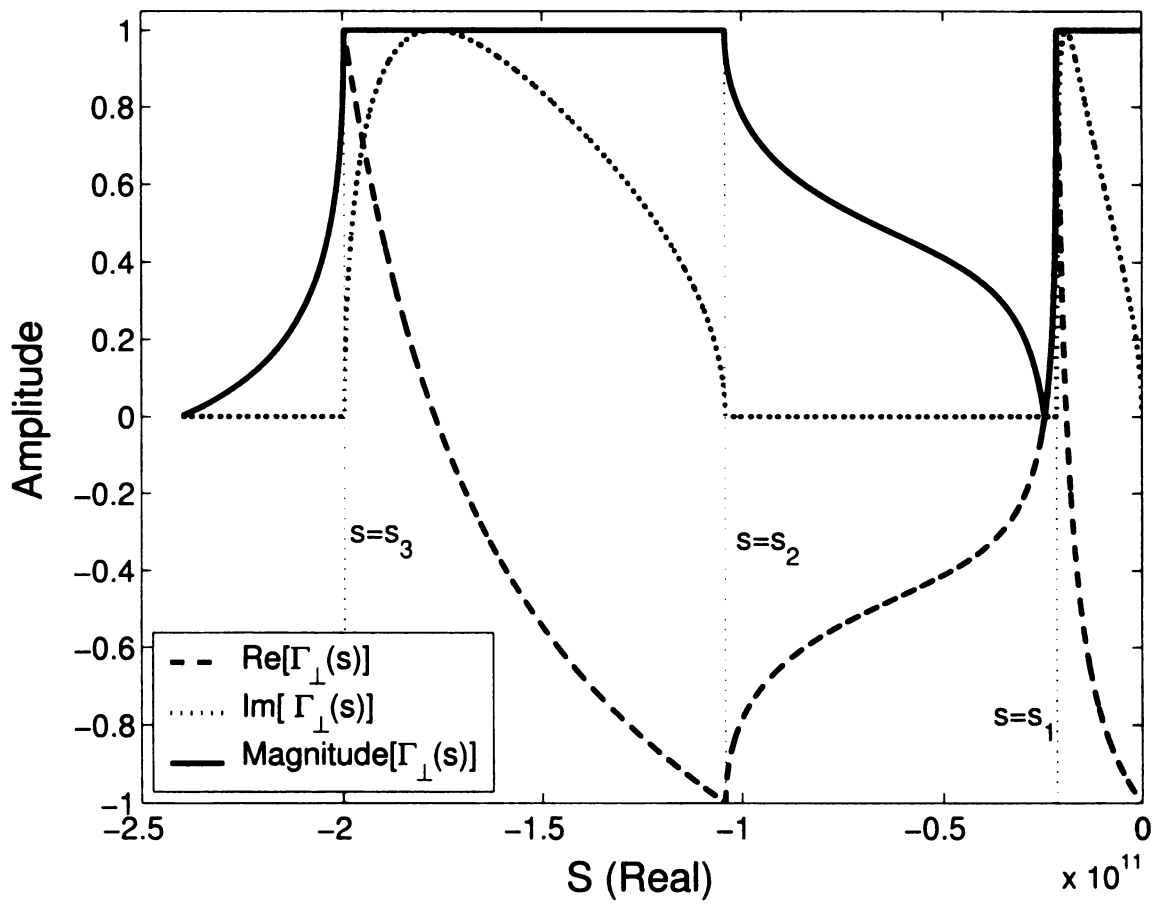

Figure 5.7: Amplitude of the reflection coefficient vs. frequency for $\perp$ polarization ($\epsilon_s = 5.0\epsilon_0$, $\epsilon_\infty = 3.0\epsilon_0$, $\xi = 9.6 \times 10^{-12}$ sec, $\Delta = 2$ cm, $\theta_i = 30°$, $\sigma = 1.0$ S/m).

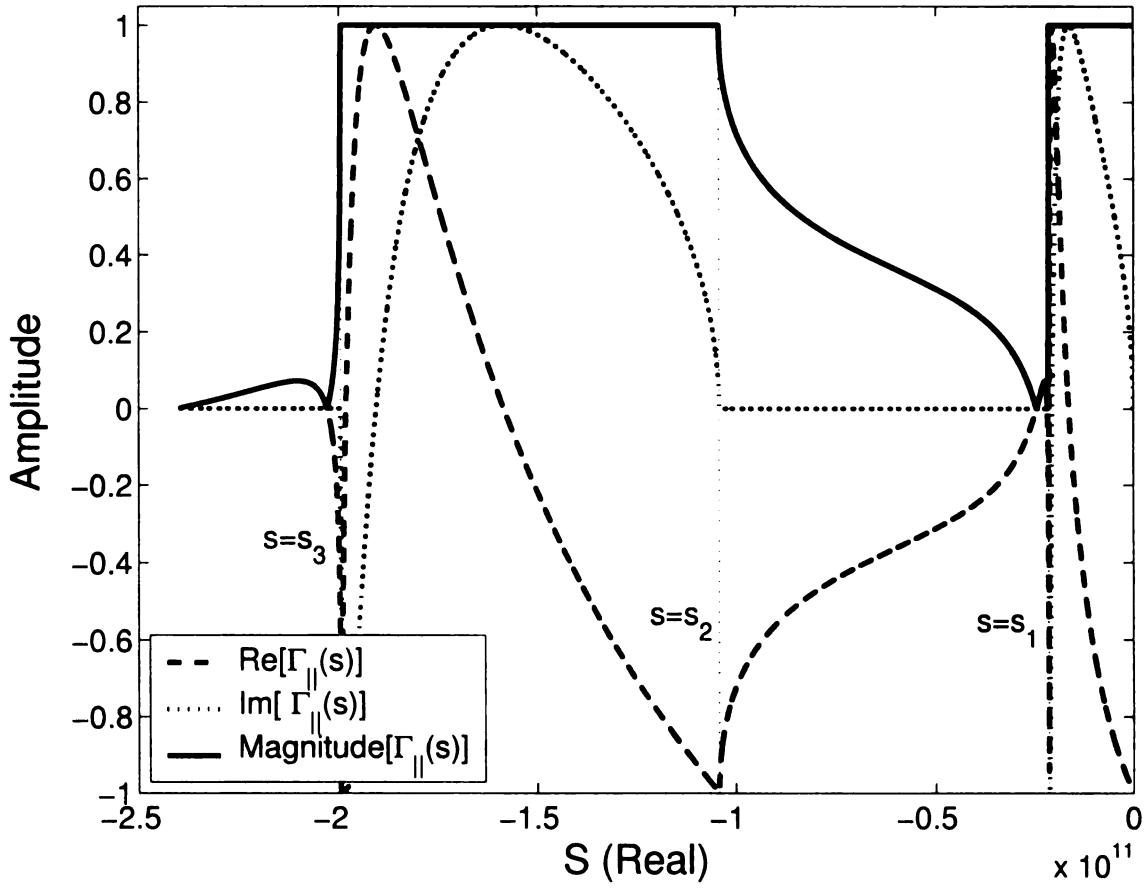

Figure 5.8: Amplitude of the reflection coefficient vs. frequency for $\|$ polarization ($\epsilon_s = 5.0\epsilon_0$, $\epsilon_\infty = 3.0\epsilon_0$, $\xi = 9.6 \times 10^{-12}$ sec, $\Delta = 2$ cm, $\theta_i = 30°$, $\sigma = 1.0$ S/m).

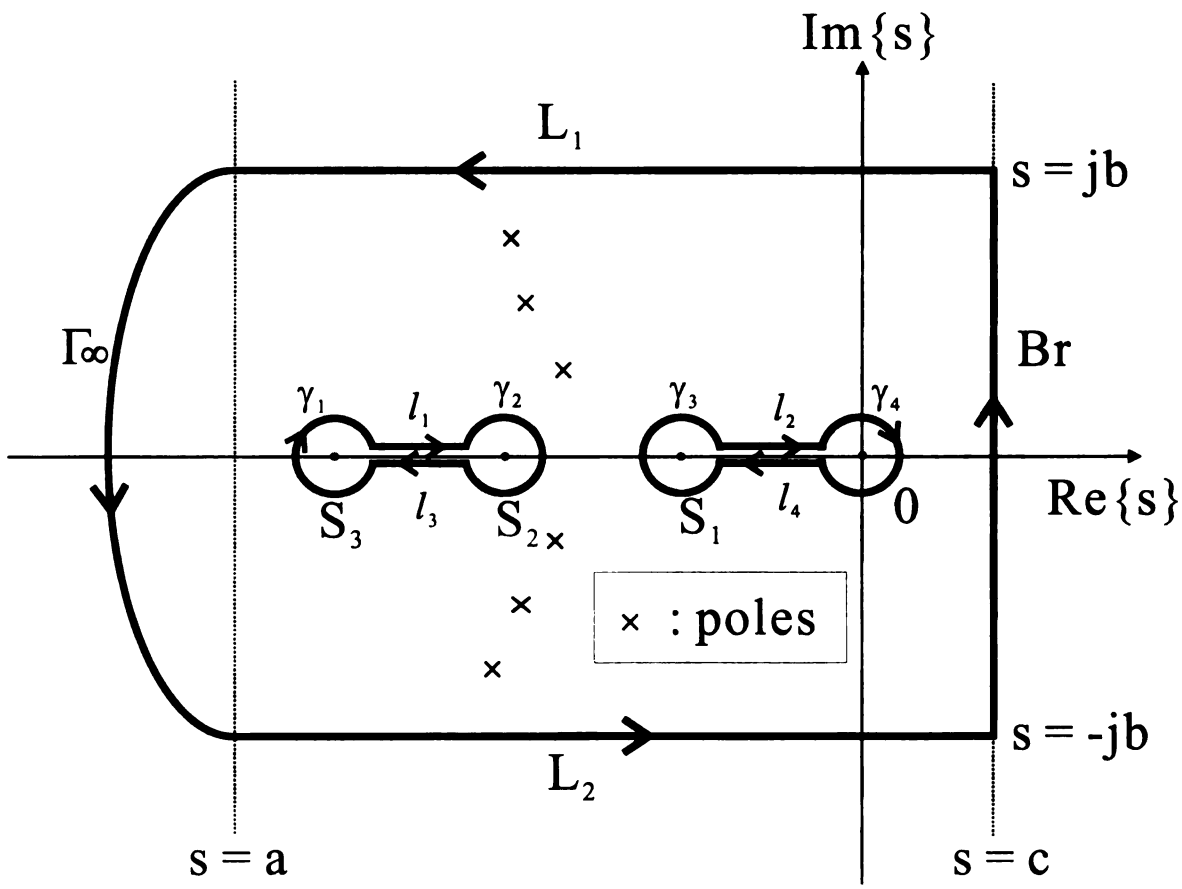

Figure 5.9: The integration contour when $t > \tau_0$. $|a|, |b| \to \infty$, $0 < c < \infty$.

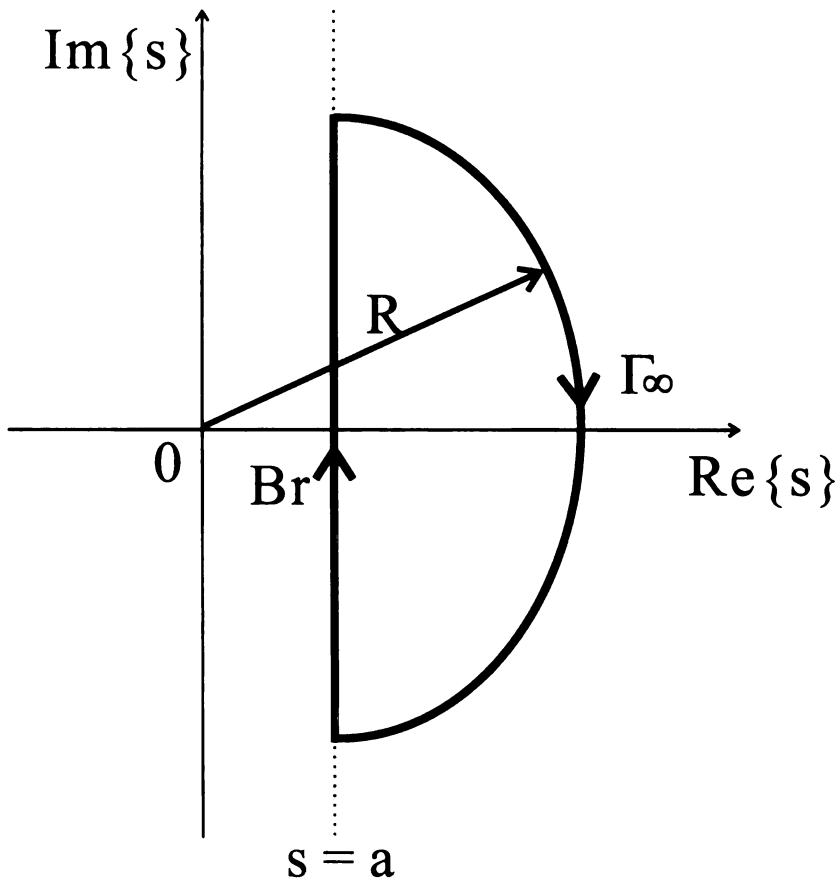

Figure 5.10: The integration contour when $t < \tau_0$. $R \to \infty$, $0 < a < \infty$.

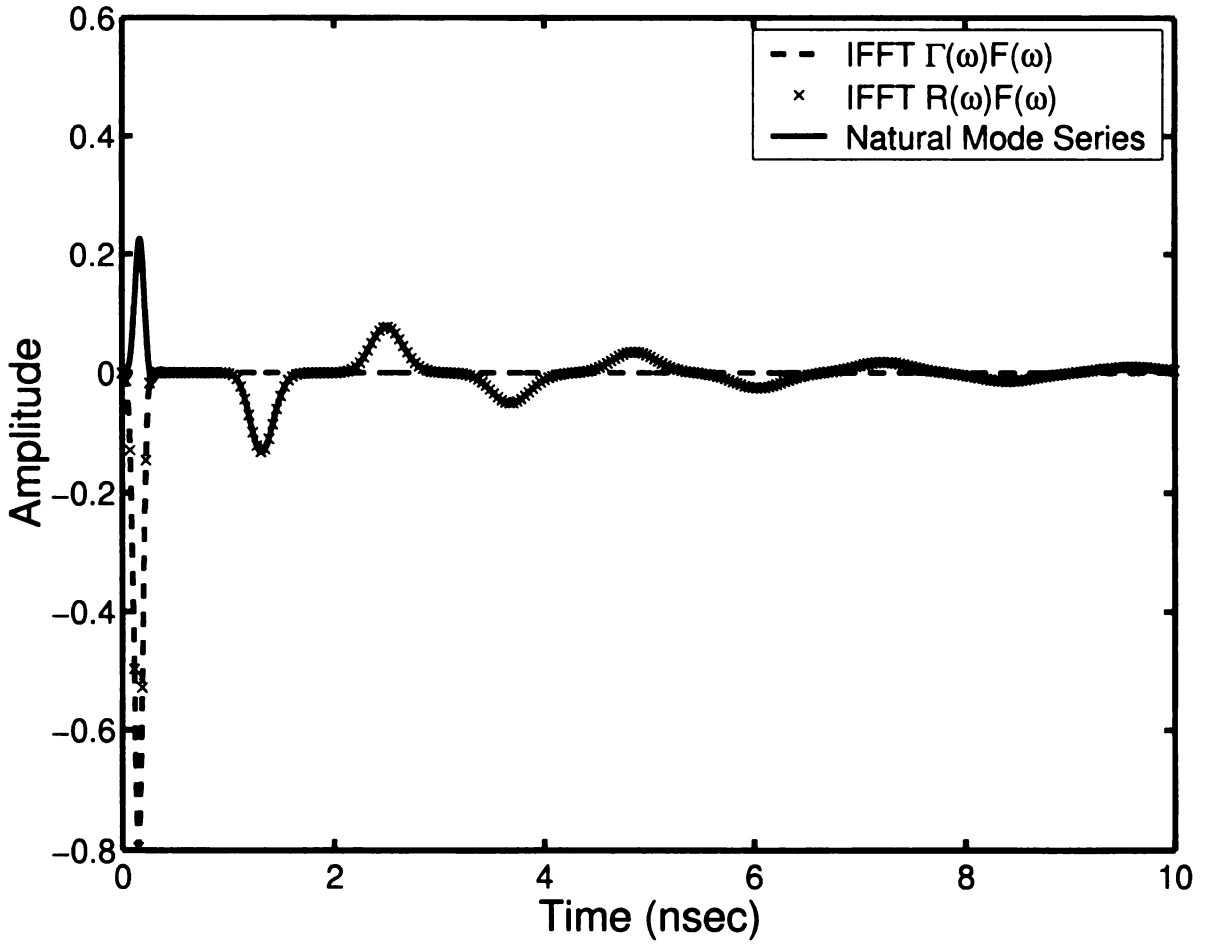

Figure 5.11: Time domain response, conductor-backed case, normal incidence, ($\epsilon_s = 78.3\epsilon_0$, $\epsilon_\infty = 5.0\epsilon_0$, $\xi = 9.6 \times 10^{-12}$ sec, $\Delta = 2$ cm, $\theta_i = 0°$, $\sigma = 0.0$ S/m).

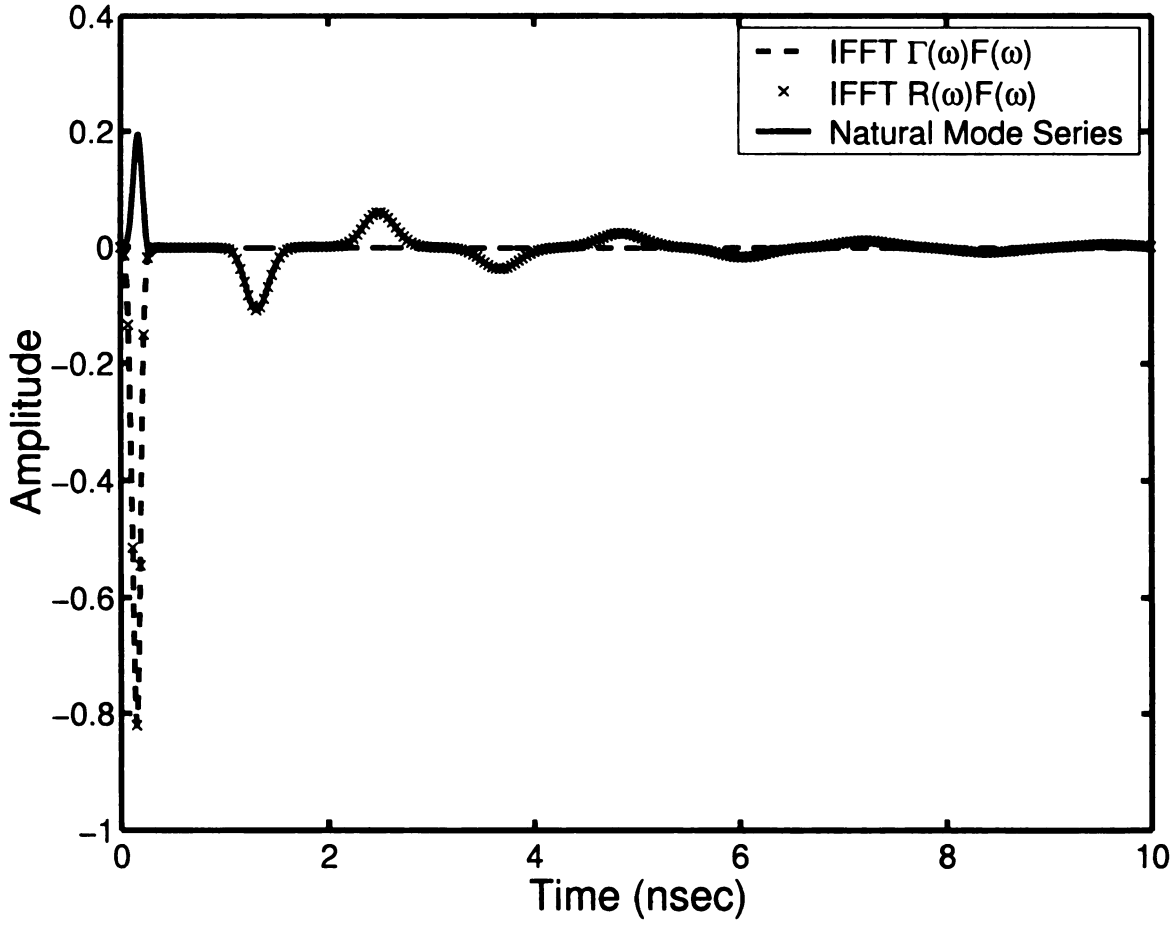

Figure 5.12: Time domain response, conductor-backed case, $\perp$ polarization, ($\epsilon_s = 78.3\epsilon_0$, $\epsilon_\infty = 5.0\epsilon_0$, $\xi = 9.6 \times 10^{-12}$ sec, $\Delta = 2$ cm, $\theta_i = 30°$, $\sigma = 0.1$ S/m).

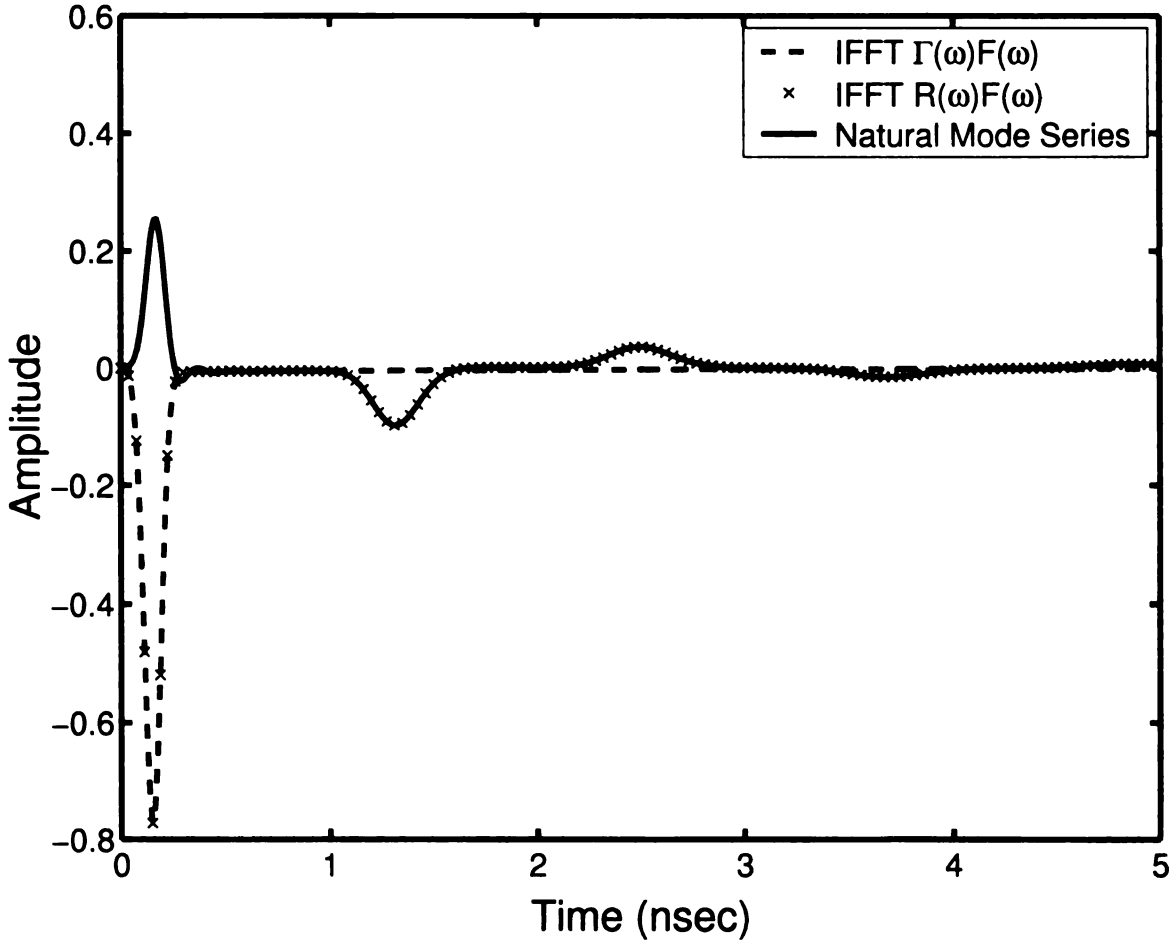

Figure 5.13: Time domain response, conductor-backed case, $\|$ polarization, ($\epsilon_s = 78.3\epsilon_0$, $\epsilon_\infty = 5.0\epsilon_0$, $\xi = 9.6 \times 10^{-12}$ sec, $\Delta = 2$ cm, $\theta_i = 30°$, $\sigma = 0.5$ S/m).

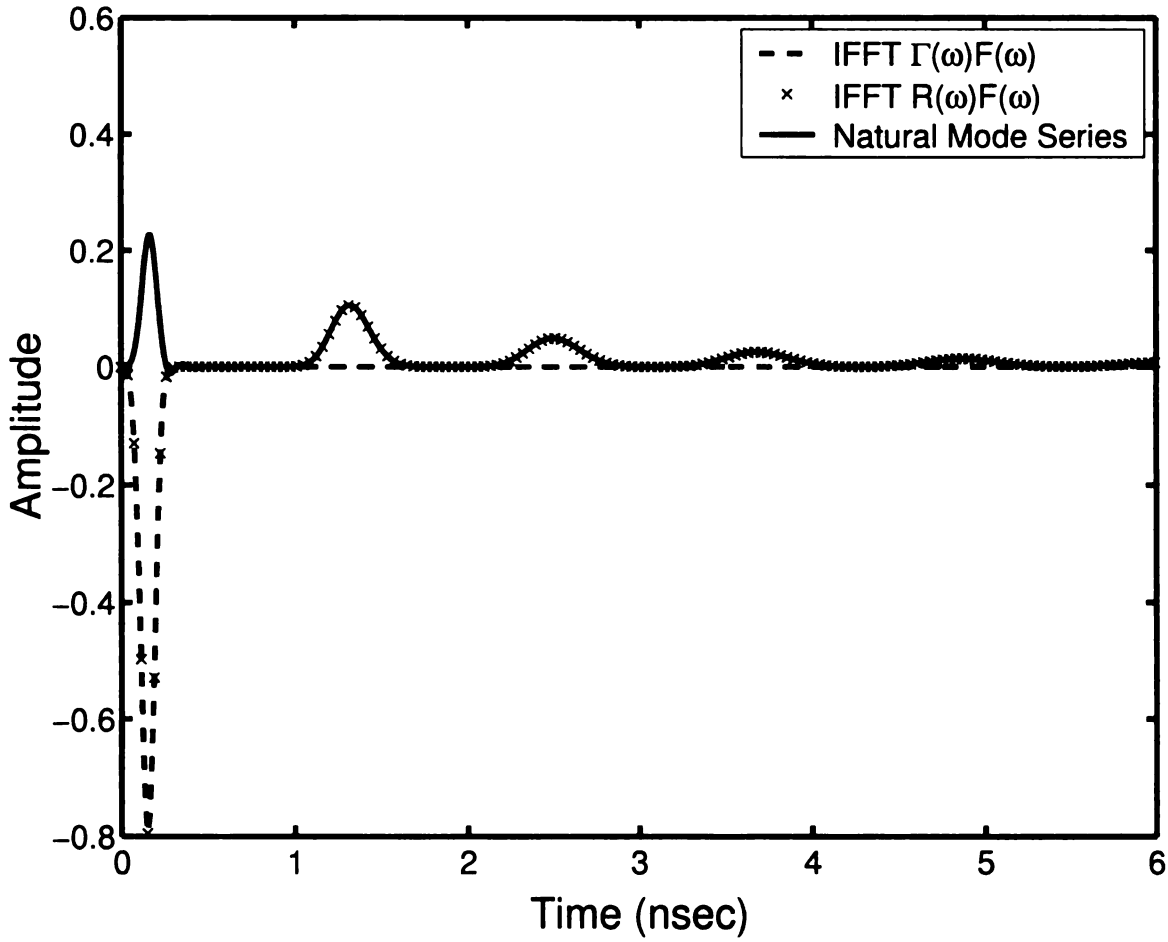

Figure 5.14: Time domain response, air-backed case, normal incidence, ($\epsilon_s = 78.3\epsilon_0$, $\epsilon_\infty = 5.0\epsilon_0$, $\xi = 9.6 \times 10^{-12}$ sec, $\Delta = 2$ cm, $\theta_i = 0°$, $\sigma = 0.0$ S/m).

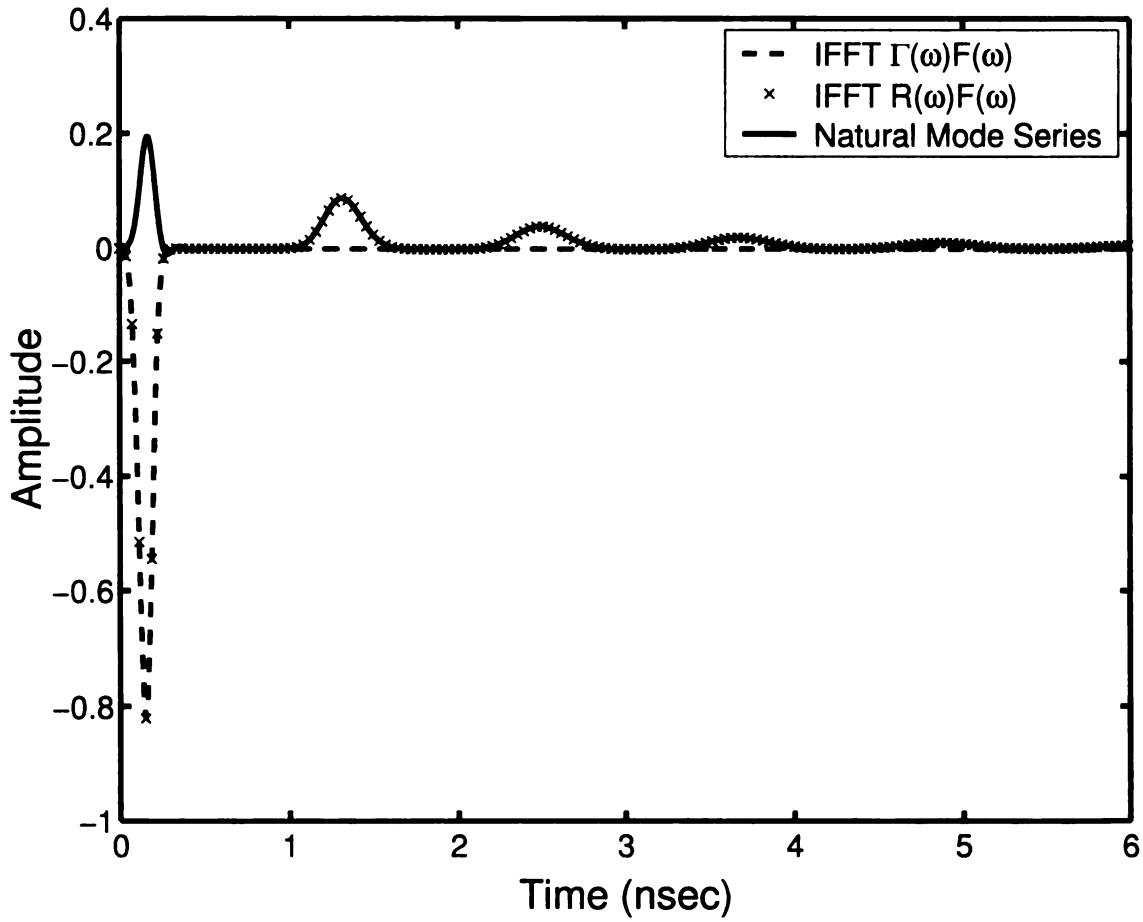

Figure 5.15: Time domain response, air-backed case, $\perp$ polarization, ($\epsilon_s = 78.3\epsilon_0$, $\epsilon_\infty = 5.0\epsilon_0$, $\xi = 9.6 \times 10^{-12}$ sec, $\Delta = 2$ cm, $\theta_i = 30°$, $\sigma = 0.1$ S/m).

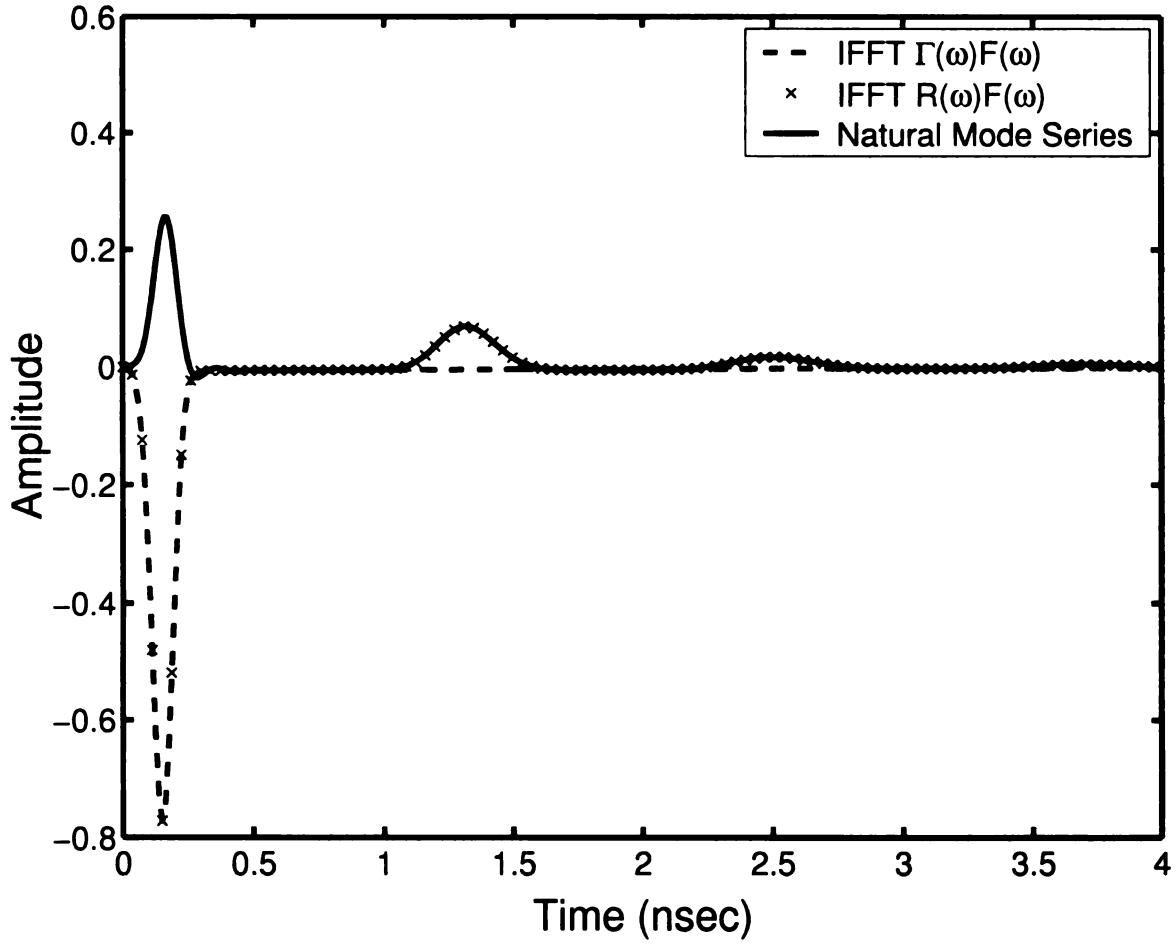

Figure 5.16: Time domain response, air-backed case, $\|$ polarization, ($\epsilon_s = 78.3\epsilon_0$, $\epsilon_\infty = 5.0\epsilon_0$, $\xi = 9.6 \times 10^{-12}$ sec, $\Delta = 2$ cm, $\theta_i = 30°$, $\sigma = 0.5$ S/m).

Chapter 6: Conclusions

The natural mode representations of the field reflected by conductor-backed and air-backed lossy layers with frequency independent or dependent (Debye type) material parameters have been analyzed and obtained numerically. It has been shown that the late time response can be represented as a pure series of damped sinusoids. These results are not only useful in the practical application to material characterization using the E-pulse method, but also give us a significant physical insight into the nature of the transient scattering.

In this thesis, a complete set of complex s domain poles was determined for each case. In particular, the existance conditions of the real poles that are indispensable for calculating the transient response were analyzed, and the determining equation was formulated and numerically implemented. It should be emphasized that, when calculating the poles numerically, it is very important to have good initial guesses and to know the approximate pole behavior in order to bound the pole locations.

Unlike in the previous work [12], [13], the evaluation of the Laplace inversion integral was accomplished analytically without resorting to numerical evaluation. It was clearly justified that the contributions from the deformation contour located at infinity and the branch cuts along the negative real axis vanishes. Here, it should be noted that the assumption of a practically realizable signal which belongs to the class of almost piecewise continuous (APC) signal [14] is fundamentally crucial in evaluating the Laplace inversion integrals. In the previous work [12], [13], the assumption of an unrealistic signal (a rectangular pulse with instant rising time) led to inaccurate and computationally expensive results.

Also in this thesis, the transient responses from the frequency dependent Debye type material were evaluated analytically showing the natural resonance representation works equally well for the frequency dependent material parameters

case. This result can be used for developing different permittivity models.

In future work, a multiple layer material can be examined with the reflection coefficient formulated in Chapter 1. Also, it may be possible to develop a different permittivity model that can better represent a general class of dielectrics. For this purpose, a series of known permittivity models such as the Debye model can be considered [32]. As a common structure, a curved structure also deserves to be examined. Finally, the parameter extraction problem, which is to find material parameters from a known time-domain response, is worthy of investigation.

BIBLIOGRAPHY

Bibliography

[1] C. L. Bennett, "Time-domain electromagnetics and its applications," Proc. IEEE, vol. 66, no. 3, pp. 299-318, 1978.

[2] L. B. Felsen, ed., *Transient Electromagnetic Fields*, Springer-Verlag, Berlin, 1976, Chapter 3 (C. E. Baum).

[3] A. G. Alexander, "Theoretical and practical aspects of singularity and eigenmode expansion methods," IEEE Trans. Antennas Propagat., vol. AP-28, no. 6, pp. 897-901, Nov. 1980.

[4] M. A. Morgan, "Singularitiy expansion representations of fields and currents in transient scattering," IEEE Trans. Antennas Propagat., vol. AP-32, no. 5, pp. 466-473, May 1984.

[5] L. B. Felson, "Comments on early time SEM," IEEE Trans. Antennas Propagat., vol. AP-33, no. 1, pp. 118-119, Jan. 1985.

[6] D. G. Dudley, "Comments on SEM and the parameter inverse problem," IEEE Trans. Antennas Propagat., vol. AP-33, no. 1, pp. 119-120, Jan. 1985.

[7] C. E. Baum, E. J. Rothwell, K.M. Chen and D. P. Nyquist, "The singularity expansion method and its application to target identification," Proc. IEEE, vol. 79, no. 10, pp. 1481-1491, 1991.

[8] E. J. Rothwell, D. P. Nyquist, K. M. Chen, and B. Drachman, "Radar target discrimination using the extinction-pulse technique," IEEE Trans. Antennas Propagat., vol. AP-33, pp. 929-937, Sept. 1985.

[9] E. J. Rothwell, K. M. Chen, D. P. Nyquist and W. Sun, "Frequency domain E-pulse synthesis and target discrimination," IEEE Trans. Antennas Propagat., vol. AP-35, pp. 426-434, Apr. 1987.

[10] G. J. Stenholm, E. J. Rothwell, D. P. Nyquist, L.C. Kempel, and K. M. Chen, "E-pulse diagnostics for layered materials," URSI Radio Science Meeting., Boston, Mass., 2001, p. 190

[11] D. Batrakov, S. Shulga, and N. Zhuck, "Application of the extinction pulse technique to non-destructive control of dielectric materials,", in IEEE AP-S Int. Symp. Dig., Ann Arbor, MI, 1993, vol. 2, pp. 880-883.

[12] A. G. Tihuis and H. Block, "SEM approach to the transient scattering by an inhomogeneous, lossy dielectric slab; Part 1: the homogeneous case," Wave Motion, vol. 6, pp. 61-78, 1984.

[13] A. G. Tihuis and H. Block, "SEM approach to the transient scattering by an inhomogeneous, lossy dielectric slab; Part 2: the inhomogeneous case," Wave Motion, vol. 6, pp. 167-182, 1984.

[14] W. R. LePage, *Complex Variables and the Laplace Transform for Engineers*, McGraw-Hill, New York, 1961, pp. 353-357.

[15] E. J. Rothwell and M. J. Cloud, *Electromagnetics*, CRC Press, Boca Raton, Florida, 2001.

[16] R. F. Harrington, *Time-Harmonic Electromagnetic Fields* , McGraw-Hill, New York, 1961.

[17] W. H. Press et al., *Numerical Recipes in FORTRAN 90*, 2nd ed. Cambridge University Press, Cambridge, New York, 1996.

[18] C. F. Gerald and P. O. Wheatley, *Applied Numerical Analysis*, 5th ed. Addison-Wesley, Massachusetts, 1994.

[19] S. J. Chapman, *Fortran 90/95 for Scientists and Engineers*, McGraw-Hill, New York, 1998.

[20] T. W. Gamelin, *Complex Analysis*, Springer-Verlag, New York, 2001, pp. 216-219.

[21] A. Papoulis, *The Fourier Integral and Its Applications*, McGraw-Hill, New York, 1962.

[22] E.A. Guillemin, *The Mathematics of Circuit Analysis*, John Wiley & Sons, New York, 1958.

[23] B. J. Ley, S. G. Lutz and C. F. Rehberg, *Linear Circuit Analysis*, McGraw-Hill, New York, 1959.

[24] D. H. Griffel, *Applied Functional Analysis*, Ellis Horwood Limited, Chichester, England, 1981.

[25] D. S. Jones, *Generalised Functions*, McGraw-Hill House, Maidenhead, Berkshire, England, 1966.

[26] J. W. Suk and E. J. Rothwell, "Transient Analysis of TE-Plane Wave Reflection from a Layered Medium," Journal of Electromagnetic Waves and Applications, vol. 16, no. 2, pp. 281-297, 2002.

[27] J. W. Suk and E. J. Rothwell, "Transient Analysis of TM-Plane Wave Reflection from a Layered Medium," Journal of Electromagnetic Waves and Applications, vol. 16, no. 9, pp. 1195-1208, 2002.

[28] V. V. Daniel, *Dielectric Relaxation*, Academic Press, New York, 1967, Chapter 2.

[29] A. K. Jonscher, *Dielectric Relaxation in Solids*, Chelsea Dielectrics Press, London, 1983.

[30] J. C. Anderson, *Dielectrics*, Reinhold Publishing Corporation, New York, 1964.

[31] H. Fröhlich, *Theory of Dielectrics*, Oxford University Press, London, 1958.

[32] M. Mrozowski and M. Stuchly, "Parameterization of Media Dispersive Properties for FDTD," IEEE Trans. Antenas Propagat., vol. 45, no. 9, pp. 1438-1439, 1997.